

Asian Power Electronics Journal

PERC, HK PolyU

Copyright © The Hong Kong Polytechnic University 2009

All right reserved. No part of this publication may be reproduced or transmitted in any form or by any means, electronic or mechanical, including photocopying recording or any information storage or retrieval system, without permission in writing form the publisher.

First edition September 2009

Printed in Hong Kong by Reprographic Unit
The Hong Kong Polytechnic University

Published by

Power Electronics Research Centre
The Hong Kong Polytechnic University
Hung Hom, Kowloon, Hong Kong

ISSN 1995-1051

Disclaimer

Any opinions, findings, conclusions or recommendations expressed in this material/event do not reflect the views of The Hong Kong Polytechnic University

Editorial board

Honorary Editor

Prof. Fred C. Lee

Electrical and Computer Engineering, Virginia Polytechnic Institute and State University

Editor

Prof. Yim-Shu Lee

Victor Electronics Ltd.

Associate Editors and Advisors

Prof. Philip T. Krien

Department of Electrical and Computer Engineering, University of Illinois

Prof. Keyue Smedley

Department of Electrical and Computer Engineering, University of California

Prof. Muhammad H. Rashid

Department of Electrical and Computer Engineering, University of West Florida

Prof. Dehong Xu

College of Electrical Engineering, Zhejiang University

Prof. Hirofumi Akagi

Department of Electrical Engineering, Tokyo Institute of Technology

Prof. Xiao-zhong Liao

Department of Automatic Control, Beijing Institute of Technology

Prof. Wu Jie

Electric Power College, South China University of Technology

Prof. Hao Chen

Dept. of Automation, China University of Mining and Technology

Prof. Danny Sutanto

Integral Energy Power Quality and Reliability Centre, University of Wollongong

Prof. Siu L.Ho

Department of Electrical Engineering, The Hong Kong Polytechnic University

Prof. Eric Cheng

Department of Electrical Engineering, The Hong Kong Polytechnic University

Dr. Norbert Cheung

Department of Electrical Engineering, The Hong Kong Polytechnic University

Dr. Kevin Chan

Department of Electrical Engineering, The Hong Kong Polytechnic University

Dr. Tze F. Chan

Department of Electrical Engineering, The Hong Kong Polytechnic University

Dr. Martin Chow

Department of Electronic and Information Engineering, The Hong Kong Polytechnic University

Dr. Edward Lo

Department of Electrical Engineering, The Hong Kong Polytechnic University

Dr. Mark Ho

Department of Electrical Engineering, The Hong Kong Polytechnic University

Dr. David Cheng

Department of Industrial and System Engineering, The Hong Kong Polytechnic University

Dr. Frank Leung

Department of Electronic and Information Engineering, The Hong Kong Polytechnic University

Publishing Director:

Prof. Eric Cheng

Department of Electrical Engineering, The Hong Kong Polytechnic University

Communications and Development Director:

Ms. Anna Chang

Anna Chang PR Consultancy

Editorial Committee:

Prof. Zhe Chen

Prof. Dehong Xu

Prof. Xiaozhong Liao

Dr. B.P.Divakar

Dr. Kai Ding

Dr. Xue XiangDang

Dr. James Ho

Dr. Benny Y.P.Yeung

Dr. S.X.Wang

Dr. W.N. Fu

Dr. Tze F. Chan

Dr. Martin Chow

Dr. Frank Leung

Dr. Patrick Luk

Dr. Y.B. Che

Dr. R. Zaimeddine

Dr. Mohan Aware

Dr. Wai Chwen Gan

Dr. Dong Lei

Dr. E. Chandra Sekaran

Dr. Chi Kwan Lee

Production Coordinator:

Mr. Ken Ho

Power Electronics Research Centre, The Hong Kong Polytechnic University

Secretary:

Ms. Canary Tong

Department of Electrical Engineering, The Hong Kong Polytechnic University

Table of Content

Experimental Investigation of Five-Phase Induction Motor Drive Using Extended Kalman-Filter	1
Khan M. Rizwan and Iqbal Atif	
A daptive Neuro-Fuzzy Speed Controller for Vector Controlled Induction Motor Drive	8
Kumar Rajesh, Gupta R. A. and Surjuse Rajesh S.	
High Voltage Multilevel DC-DC Converter in Auto Balancing Mode	15
Virulkar Vasudeo B., Mohod Sharad W. and Aware Mohan V.	
Performance Investigation of Modified Self- Commutated CSI-fed Induction Motor Drive	21
Agarwal Pramod, Pandey A.K. and Verma V.K.	
Reliability Estimation for Power Factor Correction Circuits	30
Praveen Kumar A, Gulam Amer and Srinivasa Rao.S	
Control Technologies in Distributed Generation System Based on Renewable Energy	39
WU Jie, Chen Sizhe, Zeng Jun and Gao Lamei	
Author Index	53

Experimental Investigation of Five-Phase Induction Motor Drive Using Extended Kalman-Filter

M. Rizwan Khan¹ Atif Iqbal²

Abstract — In this paper extended Kalman filter (EKF) is reviewed for estimating the rotor position/speed of a vector controlled five-phase induction motor drive. The basic configuration of the Kalman filter is studied and the system vectors and matrices are explained. The EKF equations are made from a d-q-axis model of the five-phase induction motor by considering the rotor speed as a state variable. The simulation and experimental results show that the EKF is capable of tracking the actual rotor speed. Care should be taken in the selection of elements of the covariance matrices. The performance of the EKF is acceptable even in the presence of noise.

Keywords - Induction motor, Sensorless control, Kalman filter, Five-phase.

I. INTRODUCTION

Three-phase induction machine in industry is mostly used for speed control. For speed control ac drives are used which require a power electronic converter for their supply (mostly an inverter with a dc link), therefore number of machine phases is effectively unlimited. Multi-phase ac drive applications have increases enormously, since multiphase machines tender many advantages over their three-phase counterparts. A number of multi-phase machine research results have been reported [1-8].

Main advantages of multi-phase machine over three-phase machine are superior torque density, better efficiency, low torque pulsations, better fault tolerance, and reduced rating per inverter leg. Furthermore, noise performances of the drive improve as well. The limitation of multi-phase machine is that it needs a power electronic converter for phase conversion because three-phase supply is only easily available.

In most drive systems (speed and torque controlled), closed loop control is used in which shaft encoder is used for measurement of speed/position of the motor. However, in a compact drive system it is very difficult and expensive to use speed sensors for speed measurement (e.g. submarine applications). The cost of system can be reduced by eliminating the speed sensor and connection cables, and so the consistency and ruggedness of the overall drive system increases. A series of speed sensorless control techniques for induction motor has been reported in the last decade. The motor speed is estimated using these techniques and used as a feedback signal for closed-loop speed control.

Kalman filter is a unique observer which offers best possible filtering of the noise in measurement and of the system if the noise covariances are known. If rotor speed considered as an extended state and is incorporated in the dynamic model of an induction machine then the extended Kalman filter can be used to relinearize the nonlinear state model for each new value of estimate. As a result, the extended Kalman filter is measured to be the best solution for the speed estimation of an induction machine [9]. The extended Kalman filter has been applied to the vector control system [10-12] and for a direct control system or a constant Volt per Hertz. Few publications has been reported for the choice of the covariance matrices of the Kalman speed estimator. In this paper, the Kalman speed estimator for a vector controlled five-phase induction motor drive system is studied.

II. KALMAN FILTERS

Kalman filter takes care of the effects of the disturbance noise of a control system and the errors in the parameters of the system are considered as noise. The Kalman filter can be expressed as a state model [13]:

$$\dot{x} = Ax + Bu + U(t)w(t) \quad (\text{System equation}) \quad (1)$$

$$y = Cx + v(t) \quad (\text{Measurement equation}) \quad (2)$$

where

$U(t)$ = weight matrix of noise

$v(t)$ = noise matrix of output model (measurement noise)

$w(t)$ = noise matrix of state model (system noise)

$U(t)$, $v(t)$, and $w(t)$ are assumed to be stationary, white, and Gaussian noise, and their expectation values are zero. The covariance matrices Q and R of this noise are defined as:

$$Q = \text{covariance}(w) = E\{ww'\} \quad (3)$$

$$R = \text{covariance}(v) = E\{vv'\} \quad (4)$$

where $E\{\cdot\}$ denotes the expected value.

The basic configuration of the Kalman filter is shown in Fig. 1.

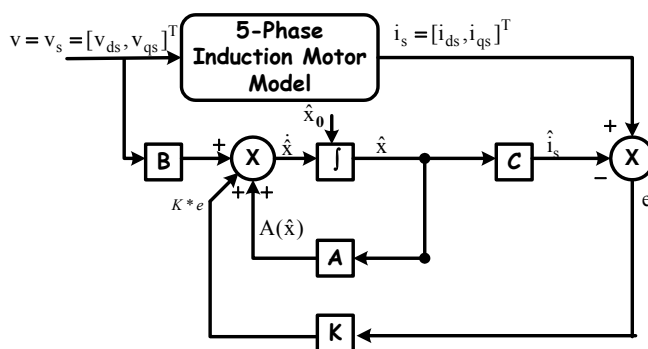


Fig. 1: The basic configuration of the Kalman filter observer.

The paper first received 3 Jun 2008 and in revised from 27 Sept 2008.
Digital Ref: A170501189

¹Department of Electrical Engineering, Aligarh Muslim University, Aligarh, India, E-mail: rizwan_eed@rediffmail.com

²Department of Electrical Engineering, Aligarh Muslim University, Aligarh, India, E-mail: atif_iqbal1@rediffmail.com

The state equations of the Kalman filter can be made as follows:

$$\hat{x} = (A - KC)\hat{x} + Bu + Ky \quad (5)$$

The Kalman filter matrix is based on the covariance of the noise and denoted by K . The measure of quality of the observation is expressed as follows:

$$L_x = \sum E\{[x(k) - \hat{x}(k)]^T [x(k) - \hat{x}(k)]\} = \min \quad (6)$$

The value of K should be such that as to minimize L_x . The result of K is a recursive algorithm for the discrete time case. The discrete form of Kalman filter may be written by the following equations, in which all symbols denote matrices or vectors [13]:

(i) System state estimation:

$$x(k+1) = x(k) + K(k)(y(k) - \hat{y}(k)) \quad (7)$$

(ii) Renew of the error covariance matrix:

$$P(k+1) = P(k) - K(k)h^T (k+1)P(k) \quad (8)$$

(iii) Calculation of Kalman filter gain matrix:

$$K(k+1) = P^*(k+1)h^T (k+1)[h(k+1)P^*(k+1)h^T (k+1) + R]^{-1} \quad (9)$$

(iv) Prediction of state matrix:

$$f(k+1) = \frac{\partial}{\partial x} (A_d x + B_d v) \Big|_{x=\hat{x}(k+1)} \quad (10)$$

(v) Estimation of error covariance matrix:

$$P^*(k+1) = f(k+1)\hat{P}(k)f^T (k+1) + Q \quad (11)$$

Discretization of (1) and (2) yields:

$$x(k+1) = A_d(k)x(k) + B_d(k)u(k) \quad (12)$$

$$y(k) = C_d(k)x(k) \quad (13)$$

where $K(k)$ is the feedback matrix of the Kalman filter. $K(k)$ gain matrix calculates how the state vector of the Kalman filter is updated when the output of the model is compared with the actual output of the system. The Kalman filter algorithm can also be used for nonlinear systems (e.g. induction motor). However, the optimal performance may not be obtained and it is impractical to verify the convergence of the model. To realize the recursive algorithm of the extended Kalman filter, a state model of the induction motor is required. After knowing the matrices A_d , B_d , and C_d , the matrices $x(k)$ (state prediction) and $y(k)$ (output prediction) can be calculated.

III. DESIGN OF EXTENDED KALMAN FILTER FOR FIVE-PHASE INDUCTION MOTOR DRIVE

When rotor speed is considered as a state variable in the induction motor model, then an extended induction motor model is obtained and the rotor speed is considered as an extended state. The discrete induction motor model defined in (12) and (13) can be implemented in the extended Kalman filter algorithm.

If the system matrix, the input and output matrices of the discrete system are denoted by A_d , B_d , and C_d , while the state and the output of the discrete system are denoted by $x(k)$ and $y(k)$, then

$$A_d = \begin{bmatrix} 1-T/T_s^* & 0 & TL_m/(L_s' L_r T_r) & \omega_r TL_m/(L_s' L_r) & 0 \\ 0 & 1-T/T_s^* & -\omega_r TL_m/(L_s' L_r) & TL_m/(L_s' L_r T_r) & 0 \\ TL_m/T_r & 0 & 1-T/T_r & -T\omega_r & 0 \\ 0 & TL_m/T_r & T\omega_r & 1-T/T_r & 0 \\ 0 & 0 & 0 & 0 & 1 \end{bmatrix}$$

$$B_d = \begin{bmatrix} T/L_s' & 0 \\ 0 & T/L_s' \\ 0 & 0 \\ 0 & 0 \\ 0 & 0 \end{bmatrix}$$

$$C_d = \begin{bmatrix} 1 & 0 & 0 & 0 & 0 \\ 0 & 1 & 0 & 0 & 0 \end{bmatrix}$$

$$x(k) = [i_{ds}(k) i_{qs}(k) \psi_{dr}(k) \psi_{qr}(k) \omega_r(k)]^T$$

$$u(k) = [u_{ds}(k) u_{qs}(k)]^T$$

$$y(k) = [i_{ds}(k) i_{qs}(k)]^T$$

where $L_s' = \sigma L_s = (1 - \frac{L_m^2}{L_s L_r}) L_s$,

$T_s'^* = \frac{L_s'}{R_s + R_r (L_m / L_r)^2}$ and T is the sampling time.

The essential matrices and vectors for the recursive algorithm of the extended Kalman filter can be calculated, with the discrete system model. With the help of Matlab/Simulink program, speed estimation algorithm of the extended Kalman filter can be simulated, as shown in Fig. 2. The execution of the S-function block is based on an M-file written as MATLAB code.

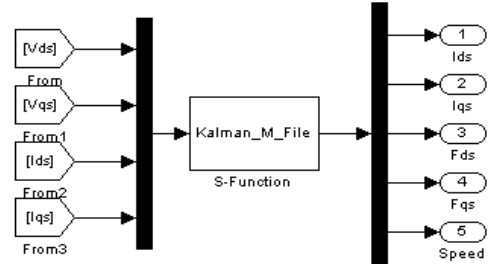


Fig. 2: Simulink based extended Kalman filter speed estimator.

IV. SENSORLESS OPERATION OF FIVE-PHASE INDUCTION MOTOR DRIVES

The developed model of a five-phase induction motor [4] indicates that an observer (Kalman Filter) used for three-phase machines can be easily extended to multi-phase machines. For multi-phase machines observer-based speed estimator requires only d and q components of stator voltages and currents. From the model of a five-phase induction machine [4], it is shown that the stator and rotor d and q axis flux linkages are function of magnetizing inductance L_m and stator and rotor d and q axis currents, where as the x and y axis flux linkages are function of only their respective currents. Therefore in speed estimation for multi-phase machine the x and y components of voltages and currents are not required. The speed can be estimated using only d and q components of stator voltages and currents.

The proposed extended Kalman filter-based vector controlled five-phase induction motor drive structure with current control in the stationary reference frame is shown in Fig. 3 (Appendix).

V. SIMULATION RESULTS

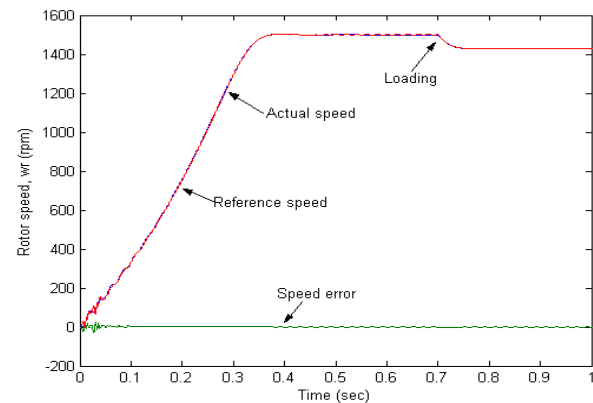
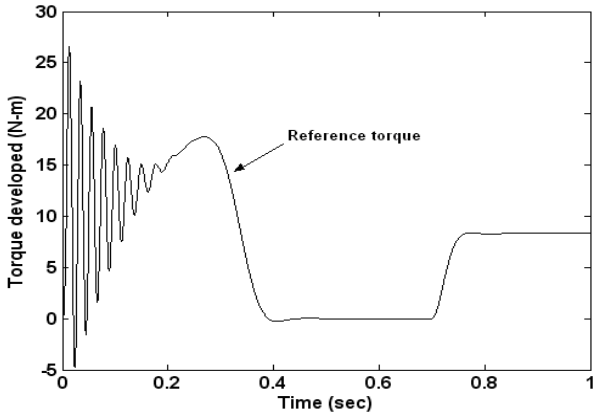


Fig. 4: Five-phase induction motor torque and speed characteristics for fixed voltage and fixed frequency fed supply ($g_1 = q_1 = 1e-6$, $g_2 = q_2 = 1e-2$).

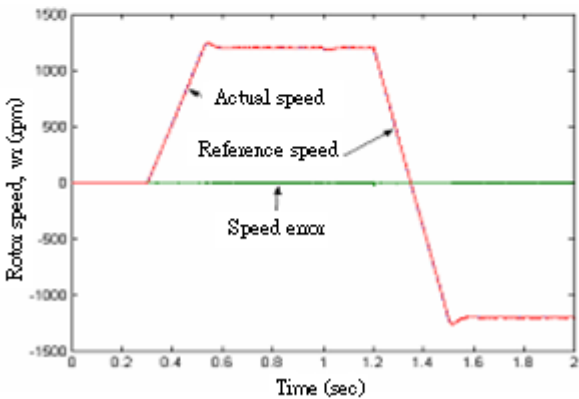
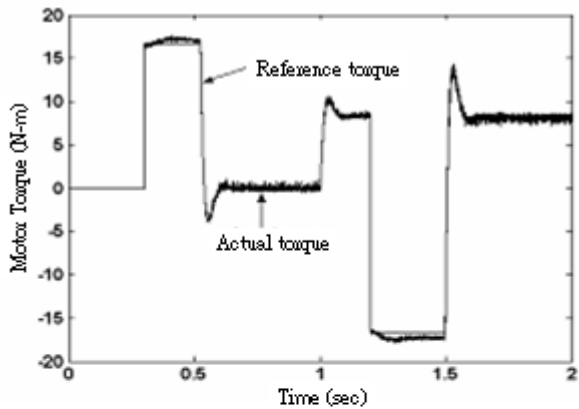


Fig. 5: Five-phase induction motor torque and speed characteristics for vector control ($g_1 = q_1 = 1e-6$, $g_2 = q_2 = 1e-2$).

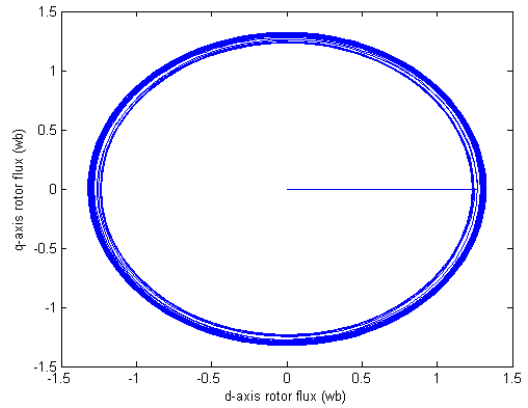


Fig. 6: Locus of rotor d- and q-axis fluxes.

The proposed drive is operated in speed mode with speed feedback is taken from kalman filter speed estimator. Fig. 4 displays the results for torque and speed characteristics of the induction motor when motor is fed with fixed voltage and fixed frequency supply. The simulation time is $t=1$ sec. and a rated torque is applied at $t=0.7$ sec. For vector control, the total simulation time is $t=2$ sec. Speed command of 1200 rpm is functional at $t=0.3$ sec in a ramp wise mode from $t = 0.3$ to $t = 0.35$ sec and is further kept unaffected. Operation takes place under no-load and load conditions. Interruption dismissal properties of the drive are investigated next. A load torque equal to the motor rated torque is functional in a step-wise mode at $t = 1$ sec. In the last, reversing transient is examined. The command for speed reversal is given at $t = 1.2$ sec. The results, obtained for these periods, are shown in Fig. 5. It is concluded from the results that, the actual speed and torque closely follow the reference. Fig. 6 displays the locus of rotor fluxes.

The error covariance matrix P of the Kalman filter is taken as a unit matrix and the measurement noise covariance matrix R of the extended Kalman filter is assumed as follows:

$$P = \text{diag}(1,1,1,1,1) \text{ and } R = \text{diag}(1e-3,1e-3)$$

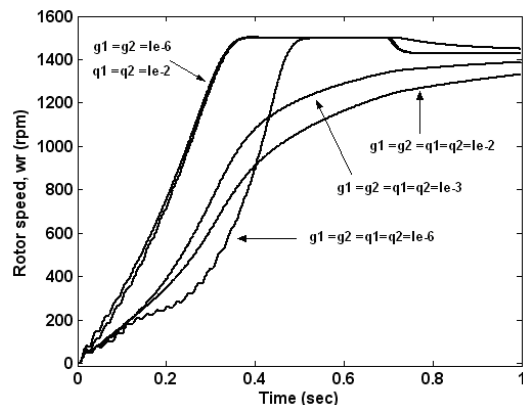
Selection of covariance matrix:

The configurations of the state noise covariance matrices G and Q are of highest importance for the superior performance of the Kalman filter algorithm. They are expressed as follows:

$$G = \text{diag}(g_1, g_1, g_1, g_1, g_2) \text{ and}$$

$$Q = \text{diag}(q_1, q_1, q_1, q_1, q_2)$$

Fig.7 illustrates that the speed estimation of the extended Kalman filter is sensitive to the covariance matrices G and Q .



(a)

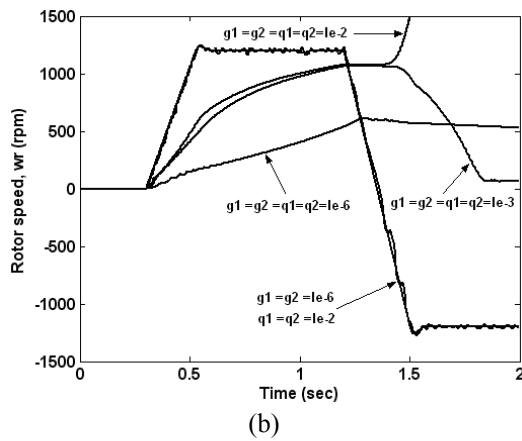


Fig. 7: Estimated speed with various covariance matrices for (a) fixed voltage and fixed frequency fed supply (b) vector control five-phase induction motor drive.

The precision of speed estimation with various G and Q may be found by the mean squared error between the actual rotor speed and the estimated speed. From Fig. 7, it is observed that when $g_1 = q_1 = 1e-6$, and $g_2 = q_2 = 1e-2$, the extended Kalman filter gives a more accurate result. When $g_1 = g_2 = q_1 = q_2$, the extended Kalman filter gives poor speed estimation results. For obtaining superior estimation results, the design principle is that the values of g_2 and q_2 in the covariance matrices G and Q should be greater than the values of g_1 and q_1 .

VI. EXPERIMENTAL RESULTS

With the advent of high-performance digital signal processors (DSPs) dedicated for motion control applications, it is now possible to control motors without speed sensors. This is obtained by algorithms/programs that estimate the desired quantities in real time, based on the electrical signals in the motor windings. The advantages are cost savings and improved consistency due to reduced component used.

The motor used in both the experiment and simulation is same. The simulation results shown in Fig. 4 to Fig. 7 have been obtained under an 8.41 N-m load. The real-time control and observer program are implemented by using the software of digital signal processor (DSP) TMS320F2812. An eddy-current machine is coupled to the shaft of the IM as a load. A feedback control system is applied to the vector controlled IM drive system. In the inner loop of the control system, a standard proportional plus integral (PI) controller is used for current control and another PI controller is used in the outer loop for speed control. The parameters of the PI controller are tuned to obtain ample performance of the control system. A PC is used for data logging, data communication, and downloading. The stator currents are detected through Hall-effect sensors. The performance of the Kalman observer is tested in the implementation for trapezoidal references. The trapezoidal references are selected to show the performance of the proposed method in both directions at variable and constant speeds. The various experimental results are shown in Fig. 8 to Fig. 11.

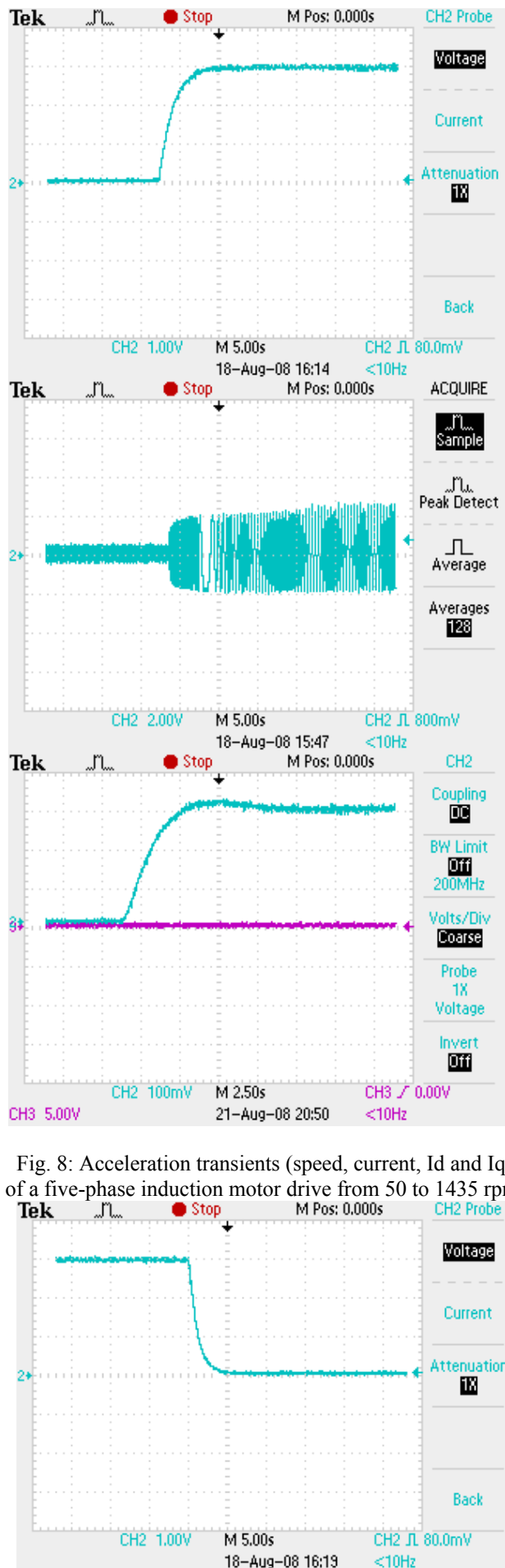


Fig. 8: Acceleration transients (speed, current, Id and Iq) of a five-phase induction motor drive from 50 to 1435 rpm.

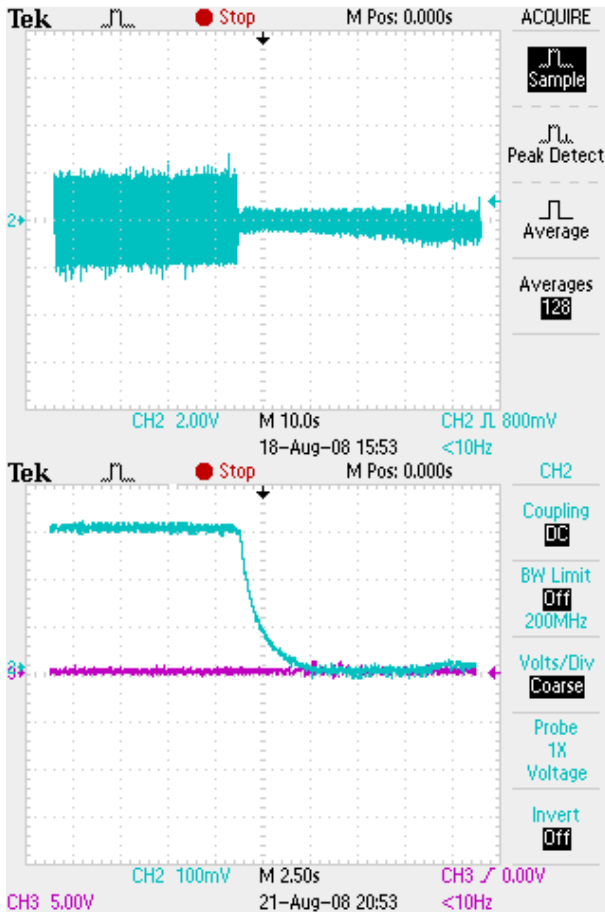


Fig. 9: Deceleration transients (speed, current, Id and Iq) of a five-phase induction motor drive from 1435rpm to 50 rpm.

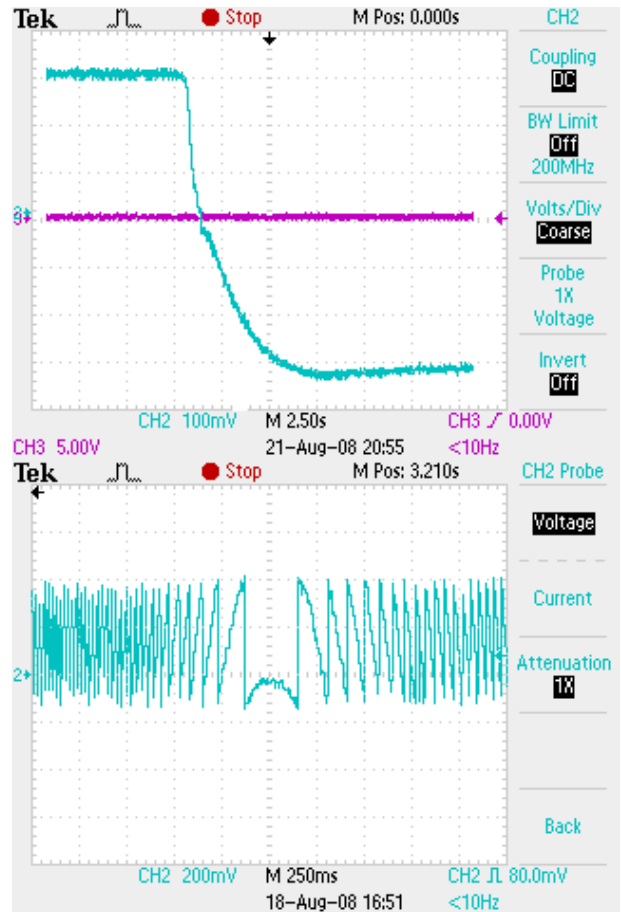
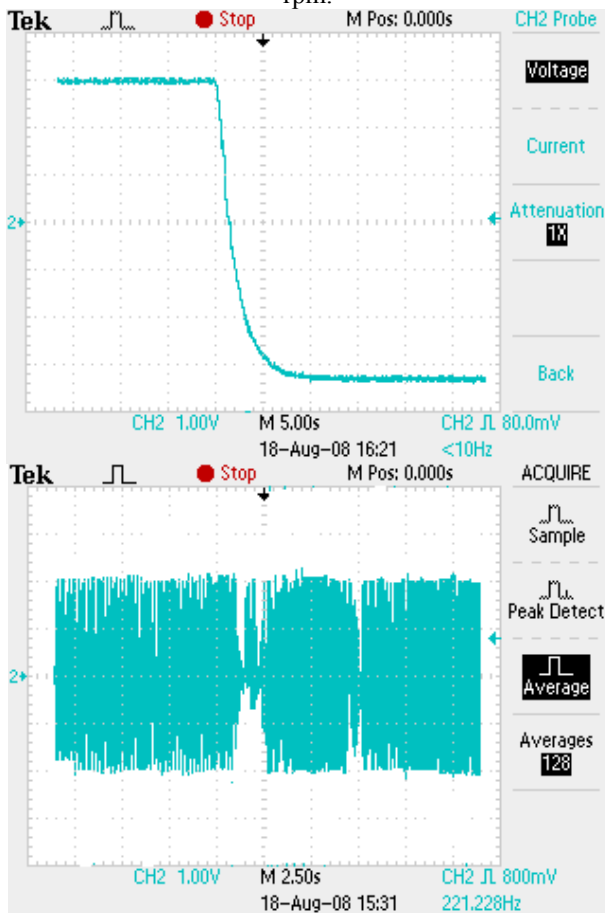
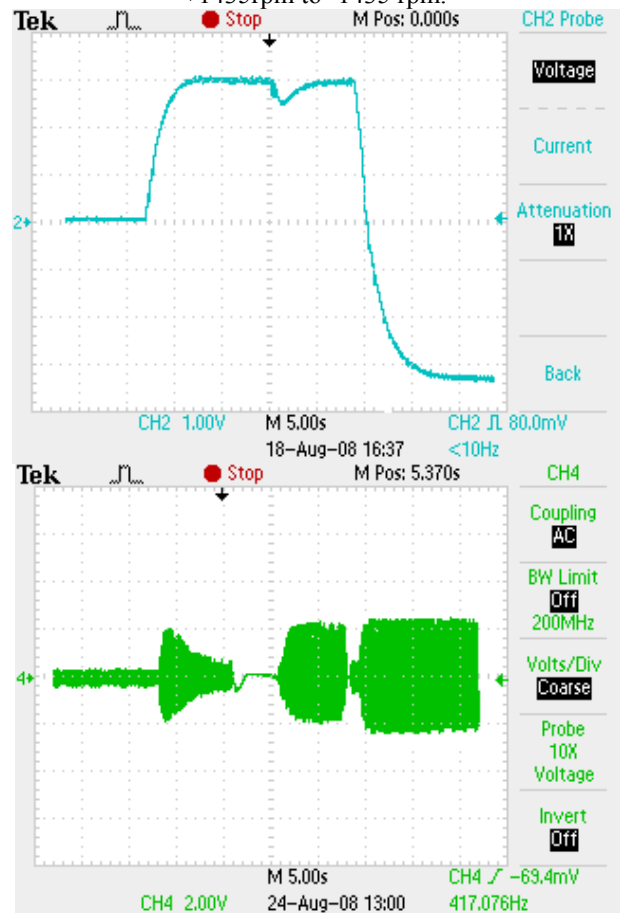


Fig. 10: Reversing transients (speed, current, Id & Iq, rotor position) of a five-phase induction motor drive from +1435rpm to -1435 rpm.



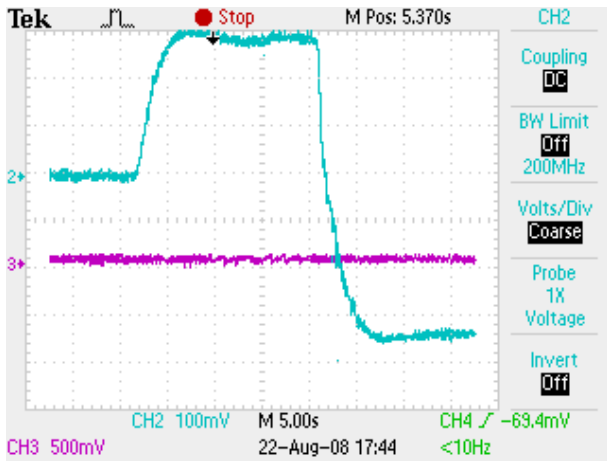


Fig. 11: Acceleration and reversing transients (speed, current, I_d and I_q) of a five-phase induction motor drive under no-load and load from 50rpm to 1435rpm to -1435 rpm.

VII. DISCUSSION

The results of the experimental study are illustrated for all transients by displaying the speed response, actual phase current and stator d- and q-axis current references. A step speed command is initiated in all the cases. There is no inertia wheel fitted to the motor. It can operate under no load and load conditions. All the transients are taken from the DAC outputs of DSP TMS320F2812. Acceleration transients, starting from 50 rpm, are shown in Fig. 8. The step speed command is 1435 rpm. Typical behavior of sensorless control of vector controlled five-phase induction motor is observed, with rapid stator q-axis current reference build up corresponding to almost instantaneous torque build up. Three different types of characteristics speed, current and I_d and I_q are shown in Fig. 8.

VIII. CONCLUSION

In this paper, an extended Kalman filter is designed to estimate the rotor speed of a vector controlled five-phase induction motor drive. Effects of the covariance matrices of the Kalman filter are studied and a suggestion for selecting the covariance matrices is also given. Simulation results show that the extended Kalman filter has excellent noise rejection properties. The attainable performance are examined by simulation and compared. It is shown that the dynamic behavior, obtainable with the indirect vector control, is the same as obtained with three-phase machine. Results are also obtained by experiments and compared with the simulation results. Experiment results show that proposed technique is well suited for speed sensorless estimation of five-phase induction machine. Same technique can be extended to multi-phase multi-motor drive system.

APPENDIX

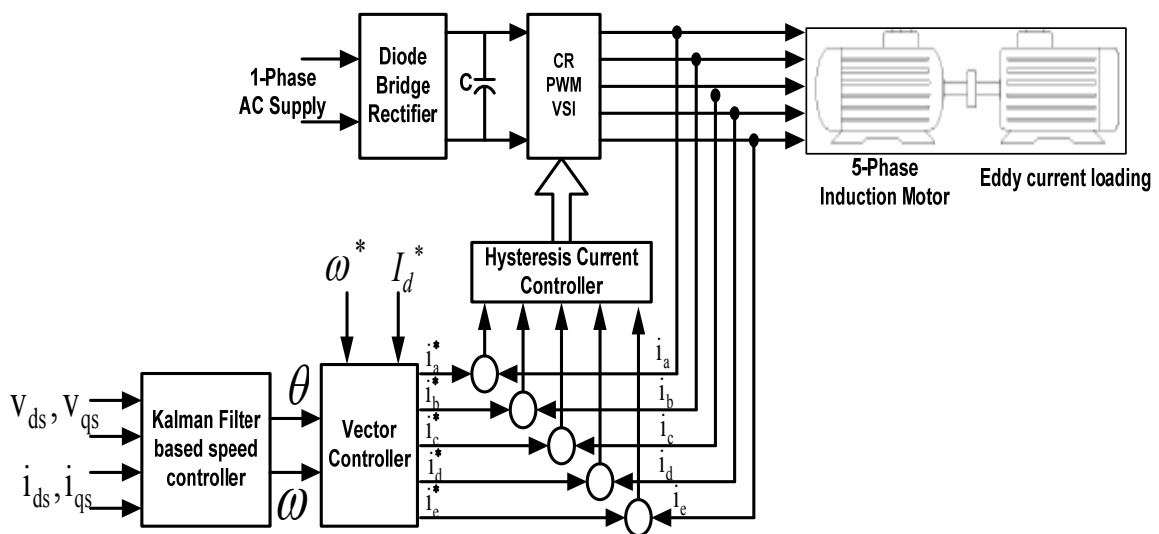


Fig. 3: A vector controlled five-phase induction motor with extended Kalman filter speed estimation algorithm

ACKNOWLEDGEMENT

The authors gratefully acknowledge the support provided for the work on this project by the AICTE, File No. 8023/BOR/RPS-86/2006-07.

REFERENCES

- [1] E. Levi, "Multi-phase electric machines for variable speed applications", IEEE Trans. On Ind. Electronics, Vol. 55, No. 5, 2008, pp. -1893-1909.
- [2] E. Levi, R. Bojoi, F. Farina, H.A. Toliyat and S. Williamson, "Multi-phase induction motor drives-A technology status review", IET Electr. Power Appl. Vol. 1, No. 4, 2007, pp. 489-516.
- [3] M.Jones and E.Levi, "A literature survey of state-of-the-art in multiphase ac drives", Proc. 37th Int. Universities Power Eng. Conf. UPEC, Stafford, UK, 2002, pp. 505-510.
- [4] A. Iqbal, S.N. Vukosavi and E.Levi, "Vector control of a five-phase induction motor drive," Proc. 38th UPEC, Thessaloniki, Greece, 2003, CD-ROM paper No. EMDII, pp.57-60.
- [5] M. Rizwan Khan, Atif Iqbal and Mukhtar Ahmad, "MRAS-Based Sensorless Control of A Vector Controlled Five-Phase Induction Motor Drive" Electric Power Systems Research, Volume 78, No. 8, August 2008, pp. 1311-1321.
- [6] M. Rizwan Khan and Atif Iqbal "MRAS-Based Sensorless Control Of Series-Connected Five-Phase Two-Motor Drive System " Korian Journal of Electrical Engineering and Technology , Vol. 3, No. 2, 2008, pp. 224-234.
- [7] M. Rizwan Khan and Atif Iqbal, "Speeds Estimation of Series-Connected Five-Phase Two-Motor Drive System Using Adaptive Flux Observers" Asian Power Electronics Journal Vol. 2, No.1, April 2008, pp. 45-54.
- [8] M. Rizwan Khan, Atif Iqbal and Mukhtar Ahmad, "Artificial Intelligence -Based Sensorless Control of A Vector Controlled Five-Phase Induction Motor Drive" IEEE International Conf. on Recent Advancement and Applications of Computer in Electrical Engineering (RACE), 24-25 March, 2006, Bikaner, India, CD_ROM paper.

- [9] C. Manes, F. Parasiliti, M. Tursini, "A Comparative Study of Rotor Flux Estimation in Induction Motors with a Nonlinear Observer and the Extended Kalman Filter", IECON 94 Conference, 1994, pp.2149-2154.
- [10] G. Henneberger, B.J. Brunsbach, Th. Klepsch, "Field-Oriented Control of Synchronous and Asynchronous Drives without Mechanical Sensors using a Kalman Filter", Sensorless Control of AC Motor Drives, IEEE Press, 1996, pp.207-214.
- [11] Y. R. Kim, S.K. Sul, M.H. Park, "Speed Sensorless Vector Control of Induction Motor Using Extended Kalman Filter", Sensorless Control of AC Motor Drives, IEEE Press, 1996, pp. 2 15-223.
- [12] L. Salvatore. S. Stasi, S. and L. Tarchioni, "A New EKF-based Algorithm for Flux Estimation in Induction Machines", IEEE Transactions on Industrial Electronics, Vol.40, No.5, 1993, pp.496-504.
- [13] F. L. Lewis, "Applied Optimal Control & Estimation", Prentice Hall, Inc., 1992.
- [14] M. Chee, "Dynamic Simulation of Electric Machinery Using Matlab/Simulink" PrenticeHall, Inc., 1998.

BIOGRAPHIES

M. Rizwan Khan received his B.Sc. Engineering, M.Tech. (Electrical) and Ph.D. degrees in 1998, 2001 and 2009 respectively, from the Aligarh Muslim University, Aligarh, India. He is an Asstt. Professor in the Department of Electrical Engineering, Aligarh Muslim University, Aligarh since 2001. His principal area of research interest is Power Electronics, Artificial Intelligence and Multi-phase motor drives.

Atif Iqbal received his B.Sc. and M.Sc. Engineering (Electrical) degrees in 1991 and 1996, respectively, from the Aligarh Muslim University, Aligarh, India and PhD in 2005 from Liverpool John Moores University, Liverpool, UK. He has been employed as Lecturer in the Department of Electrical Engineering, Aligarh Muslim University, Aligarh since 1991 and is currently working as a Reader in the same university. He is recipient of Maulana Tufail Ahmad Gold Medal for standing first at B.Sc. Engg. Exams in 1991, AMU and research fellowship from EPSRC,UK for pursuing Ph.D. studies. His principal area of research interest is Power Electronics and Multi-phase machine drives.

Adaptive Neuro-Fuzzy Speed Controller for Vector Controlled Induction Motor Drive

Rajesh Kumar¹ R. A. Gupta² Rajesh S. Surjuse³

Abstract– This paper presents a novel adaptive neuro-fuzzy based speed controller for vector controlled induction motor drive. The proposed neuro-fuzzy controller incorporates fuzzy logic algorithm with a five-layer artificial neural network (ANN) structure. The conventional PI controller is replaced by Adaptive Neuro-Fuzzy Inference System (ANFIS), which tunes the fuzzy inference system with hybrid learning algorithm. This makes fuzzy system to learn. The performance of the proposed neuro-fuzzy based vector controlled induction motor drive is investigated at different operating conditions. The results of the proposed controller are also compared to those obtained by a conventional PI controller and Fuzzy Logic controller. The simulation study indicates robustness and suitability of drive for high performance drive applications.

Keywords – Adaptive Neuro-Fuzzy Inference System(ANFIS), Artificial Neural Network (ANN), back propagation algorithm, hybrid learning algorithm

I. INTRODUCTION

Vector controlled induction motor (IM) drive is a very accepted method for high performance system response [1]-[2]. This method employs the conventional Proportional – Integral (PI), Proportional – Integral – Derivative (PID) controller or their adaptive versions, for variable speed drive applications. However, the design of these controllers depends on exact mathematical model with accurate parameters. The difficulties of obtaining the exact parameters of the induction motor leads to cumbersome design approach. Also the conventional fixed gain PI and PID controllers are very sensitive to disturbances, parameter variations and system non-linearity. On the other hands, the design of intelligent controllers based on Artificial Intelligence (AI) does not need the exact mathematical model of the system. Therefore Artificial Neural Network (ANN) and Fuzzy Logic Control (FLC) demands special attention for speed control of high performance IM drives.

Fuzzy Logic Controller yields superior and faster control [3]-[4], without the need of accurate mathematical model of the system and works well for complex, non-linear, multi-dimensional system with parameter variations or with less precise signals. The main design problem lies in the determination of consistent and complete rule set and shape of the membership functions. A lot of trial and error has to be carried out to obtain the desired response which is time consuming. On the other hand, ANN alone is insufficient if the training data are not enough to take care of all the operating modes.

Adaptive Neuro-Fuzzy Inference System (ANFIS) is used as an intelligent tool to design FLC [5]-[11]. It helps to generate and optimize membership functions as well as the rule base from the simple data provided. ANFIS combine the learning power of neural network with knowledge representation of fuzzy logic. This paper presents a novel speed control scheme of vector controlled IM drive based on Neuro-fuzzy controller (NFC) [12]-[14]. The proposed NFC is adapted by a hybrid learning algorithm in order to minimize the square of the error between desired and actual output. A 5-layer ANN structure is utilized to train the parameters of the FLC, which eliminates unwanted trial and error as was in the case for a conventional fuzzy logic control. A complete simulation model for vector controlled IM drive incorporating the proposed NFC was developed. The performance of the proposed NFC based IM drive has been investigated at different operating conditions. A comparison is made with the conventional PI speed controller and Fuzzy Logic speed controller response. Section II presents the mathematical modeling of IM and vector control scheme. Section III presents the design aspects of proposed NFC. Section IV and V presents the performance evaluation and conclusion respectively.

II. VECTOR CONTROLLED INDUCTION MOTOR DRIVE

Induction Motor Modeling

The mathematical model of a three- phase squirrel cage induction motor in synchronous rotating reference frames is given by equations (1)-(11) as follows [2].

$$V_{ds}^e = R_s i_{ds}^e + p\lambda_{ds}^e + w_e \lambda_{qs}^e \quad (1)$$

$$V_{qs}^e = R_s i_{qs}^e + p\lambda_{qs}^e - w_e \lambda_{ds}^e \quad (2)$$

$$0 = R_r i_{dr}^e + p\lambda_{dr}^e - (w_e - w_r) \lambda_{qr}^e \quad (3)$$

$$0 = R_r i_{qr}^e + p\lambda_{qr}^e + (w_e - w_r) \lambda_{dr}^e \quad (4)$$

Where

$$\lambda_{ds}^e = L_s i_{ds}^e + L_m i_{dr}^e \quad (5)$$

$$\lambda_{qs}^e = L_s i_{qs}^e + L_m i_{qr}^e \quad (6)$$

$$\lambda_{dr}^e = L_r i_{dr}^e + L_m i_{ds}^e \quad (7)$$

$$\lambda_{qr}^e = L_r i_{qr}^e + L_m i_{qs}^e \quad (8)$$

and electromagnetic torque

$$T_e = \frac{3}{2} \frac{P}{2} L_m (i_{qs}^e i_{dr}^e - i_{ds}^e i_{qr}^e) \quad (9)$$

$$\frac{d\theta_r}{dt} = \omega_r \quad (10)$$

$$T_e = J_m \frac{d\omega_r}{dt} + B_m \omega_r + T_L \quad (11)$$

The paper first received 17 Sept. 2008 and in revised form 10 July 2009. Digital Ref:A17050211

^{1, 2, 3} Department of Electrical Engineering, MNIT, Jaipur (INDIA)- 302017, E-mail: rkumar_mnit@rediffmail.com, rag_mnit@rediffmail.com, surjusemnit@rediffmail.com respectively.

where v_{ds}^e, v_{qs}^e are d-q axis stator voltages respectively; $i_{ds}^e, i_{qs}^e, i_{dr}^e, i_{qr}^e$ are d-q axis stator currents and d-q axis rotor currents respectively; R_s, R_r are the stator and rotor resistance per phase respectively; L_s, L_r, L_m are the self inductances of the stator and rotor and the mutual inductance respectively; P is the number of poles; p is the differentiation operator (d/dt); ω_e, ω_r are the speed of the rotating magnetic field and the rotor speed respectively; T_e, T_L are the electromagnetic developed torque and the load torque respectively; J_m is the rotor inertia; B_m is the rotor damping coefficient and θ_r is the rotor position. The transformation from abc to dq0 variables is given by equation (12).

$$f_{dq0} = [T_{abc}^e] f_{abc}^e \quad (12)$$

$$[T_{abc}^e] = \frac{2}{3} \begin{bmatrix} \cos(\omega t) & \cos(\omega t - \frac{2\pi}{3}) & \cos(\omega t + \frac{2\pi}{3}) \\ \sin(\omega t) & \sin(\omega t - \frac{2\pi}{3}) & \sin(\omega t + \frac{2\pi}{3}) \\ \frac{1}{2} & \frac{1}{2} & \frac{1}{2} \end{bmatrix} \quad (13)$$

where $[T_{abc}^e]$ is transformation matrix given by equation (13) and f may represents current or voltage.

Vector Control

For high performance drive system response, the vector controlled induction motor is a very accepted method [2]. It is based on the decoupling of flux and torque producing components of the stator current. Under this condition, the q-axis component of rotor flux is set to zero while the d-axis reaches the nominal value of the magnetizing flux. The torque equation can also be written as

$$T_e = \frac{3}{2} \frac{P}{2} \frac{L_m}{L_r} (i_{qs}^e \lambda_{dr}^e - i_{ds}^e \lambda_{qr}^e) \quad (14)$$

Since λ_{qr}^e is zero

$$T_e = \frac{3}{2} \frac{P}{2} \frac{L_m}{L_r} (i_{qs}^e \lambda_{dr}^e) = K_{te} i_{qs}^e \lambda_{dr}^e \quad (15)$$

where $K_{te} = \frac{3}{2} \frac{P}{2} \frac{L_m}{L_r} =$ torque constant

If the rotor flux linkage in equation (15) is maintained constant, then the torque is simply proportional to the torque producing component of the stator current, as in the case of the separately excited dc machine with armature current control. From equations (3), (4) and (7), (8) putting λ_{qr}^e equal to zero, other field oriented controller equations are obtained as

$$T_r \frac{d\lambda_{dr}^e}{dt} + \lambda_{dr}^e = L_m i_{ds}^e \quad (16)$$

$$\omega_e = \frac{L_m}{T_r} \frac{i_{qs}^e}{\lambda_{dr}^e} + \omega_r \quad (17)$$

T_r denotes the rotor time constant. The equation (16) resembles the field equation in a separately excited dc

machine, whose time constant is usually in the order of seconds. Likewise, the induction motor rotor time constant is in the order of seconds.

The equations which transform the synchronous reference frame to stationary reference frame are:

$$i_{qs}^S = \cos \theta_e i_{qs}^e + \sin \theta_e i_{ds}^e \quad (18)$$

$$i_{ds}^S = -\sin \theta_e i_{qs}^e + \cos \theta_e i_{ds}^e \quad (19)$$

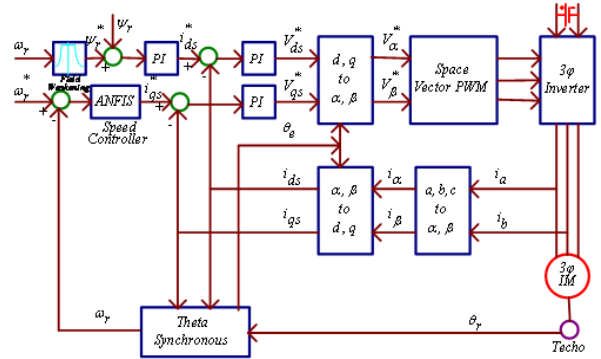


Fig. 1. Adaptive Neuro-Fuzzy speed controller based vector controlled induction motor drive.

where i_{qs}^S, i_{ds}^S are stationary frame q and d axis stator current respectively. The proposed vector control scheme is depicted in Fig. 1.

III. ADAPTIVE NEURO-FUZZY CONTROLLER

The proposed neuro-fuzzy controller incorporates fuzzy logic algorithm with a five layer artificial neural network (ANN) structure [13] as shown in fig. 2.

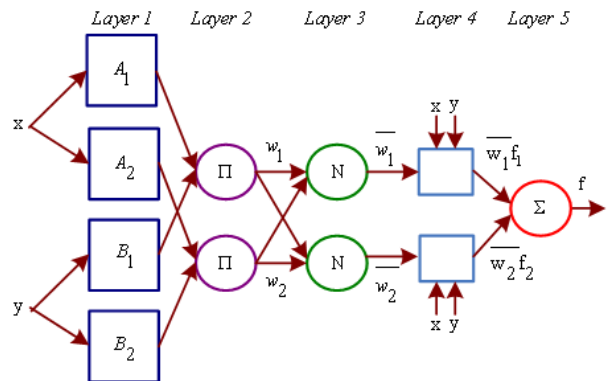


Fig. 2. ANFIS architecture of 2-input Sugeno fuzzy model with 2 rules.

A tuning block is utilized to adjust fourth layer's parameters in order to correct any deviation of control effort. The speed error and the rate of change of actual speed error are the inputs of the neuro-fuzzy controller, which are given by

$$Input1 = \varepsilon_\omega = \omega^* - \omega \quad (20)$$

$$Input2 = \Delta \varepsilon_\omega = \frac{\varepsilon_\omega(n) - \varepsilon_\omega(n-1)}{T} \times 100\% \quad (21)$$

where ω^* is the command speed and T is the sampling time.

Sugeno fuzzy model with five-layer ANN structure is used in proposed controller. In this five-layer ANN

structure the first layer represents for inputs, the second layer represents for fuzzification, the third and fourth layers represents for fuzzy rule evaluation and the fifth layer represents for defuzzification.

A two input first order Sugeno fuzzy model with two rules is depicted in fig. 2.

In layer 1, every node i is an adaptive node with a node function

$$\begin{aligned} O_{1i} &= \mu_{A_i}(x) \text{ for } i=1,2 \text{ or} \\ O_{1i} &= \mu_{B_{i-2}}(y) \text{ for } i=3,4 \end{aligned} \quad (22)$$

(here we denote the output of the i th node in layer 1 as O_{1i})

where x (or y) is the input to node i and A_i (or B_{i-2}) is a linguistic label such as ‘small’ or ‘large’ associated with this node. The membership function for A can be any appropriate parameterized membership function. In proposed scheme generalized bell function is used as a membership function given by equation (23).

$$\mu_A(x) = \left(\frac{1}{1 + \left| \frac{x-c_i}{a_i} \right|^{2b_i}} \right) \quad (23)$$

where $\{a_i, b_i, c_i\}$ is the parameter set. As the values of these parameters changes, various forms of bell shaped membership functions can be get for fuzzy set A . Parameters in this layer are referred to as premise parameters.

In layer 2, every node is a fixed node labeled Π , whose output is the product of all the incoming signals.

$$O_{2i} = w_i = \mu_{A_i}(x)\mu_{B_i}(y), \quad i=1,2 \quad (24)$$

Each node output represents the firing strength of a rule.

In layer 3, every node is a fixed node labeled N . The outputs of this layer are normalized firing strengths given by equation (25).

$$O_{3i} = \bar{w}_i = \frac{w_i}{w_1 + w_2}, \quad i=1,2 \quad (25)$$

In layer 4, every node i , is an adaptive node with a node function given by equation (26).

$$O_{4i} = \bar{w}_i f_i = \bar{w}_i (p_i x + q_i y + r_i) \quad (26)$$

where \bar{w}_i is a normalized firing strength from layer 3 and $\{p_i, q_i, r_i\}$ is the parameter set of this node. Parameters in this layer are referred to as consequent parameters.

Layer 5 is the single node layer with a fixed node labeled Σ , which computes the overall output as the summation of all incoming signals.

$$O_{5,1} = \sum_i \bar{w}_i f_i = \frac{\sum_i w_i f_i}{\sum_i w_i} \quad (27)$$

Hybrid learning algorithm [14] is used in proposed controller. It has two passes, forward pass and backward pass. In the forward pass of the hybrid learning algorithm, node output goes forward until layer four and the consequent parameters are identified by the sequential least squares method. In the backward pass, the error signals propagate backward and premise parameters are updated by gradient descent that is back propagation

learning method. The consequent parameters thus identified are optimal under the condition that the premise parameters are fixed. Thus, the hybrid approach converges much faster since it reduces the search space dimension of the original pure back propagation.

In hybrid learning, for back propagation, objective function to be minimized is defined by (28).

$$E_p = \sum_{m=1}^{\ell} (T_{m,p} - O_{m,p})^2 \quad (28)$$

where $T_{m,p}$ is the m th component of p th target output vector

and $O_{m,p}$ is the m th component of actual output vector

produced by the presentation of the p th input vector.

Hence the over all error measure is given by (29).

$$E = \sum_{p=1}^P E_p \quad (29)$$

Learning rules can be derived as follows

$$a_i(n+1) = a_i(n) - \eta_{ai} (\partial E / \partial a_i) \quad (30)$$

$$b_i(n+1) = b_i(n) - \eta_{bi} (\partial E / \partial b_i) \quad (31)$$

$$c_i(n+1) = c_i(n) - \eta_{ci} (\partial E / \partial c_i) \quad (32)$$

where η_{ai} , η_{bi} and η_{ci} are the learning rates of the

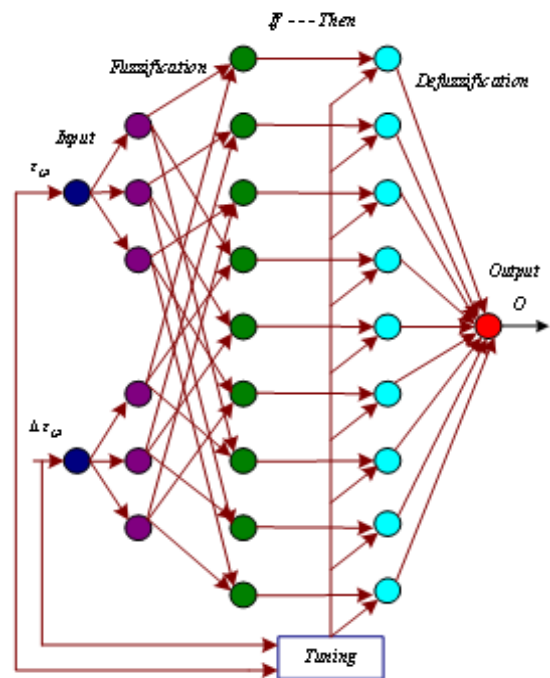


Fig. 3. Proposed equivalent ANFIS architecture

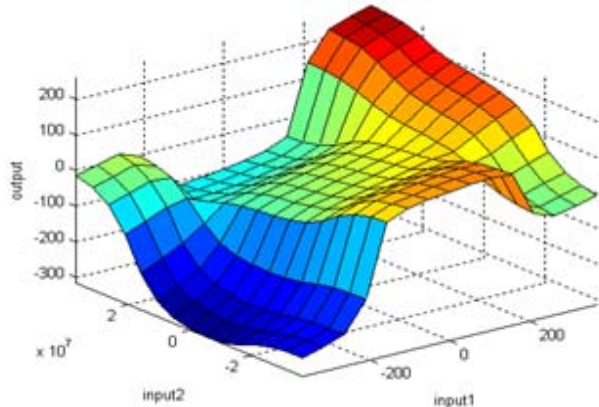


Fig. 4. Output surface of proposed ANFIS

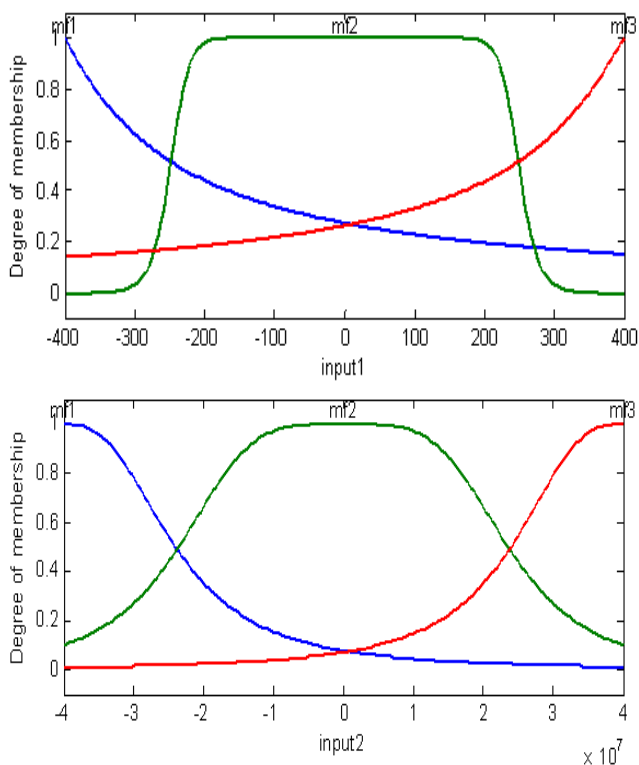


Fig. 5. Input membership function of proposed ANFIS

corresponding parameters. The derivatives in the above equations can be found by chain rule.

The propose ANFIS had following features: Type-Sugeno; AndMethod- product; OrMethod- probor (probabilistic or); DefuzzMethod- wtaver (weighted average); ImpMethod (implication method)- product; AggMethod (aggregation method)- sum; No. of input- 2; No. of input membership function- 3; input membership function type- gbellmf (generalized bell curve membership function); No. of output- 1; No. of output membership function- 9; output membership function type - linear; No. of rules- 9. Fig. 3. presents proposed equivalent ANFIS architecture. Fig. 4. and Fig. 5. shows output surface and input membership functions of proposed ANFIS respectively.

IV. PERFORMANCE ASSESSMENT OF NEURO-FUZZY CONTROLLER BASED VECTOR CONTROLLED IM DRIVE

A complete simulation model for vector controlled IM drive incorporating the proposed NFC is developed.

The performance of the proposed NFC based IM drive is investigated at different operating conditions. In order to prove the superiority of the proposed NFC, a comparison is made with the response of conventional PI and FLC speed controller based IM drive. The parameters of the induction motor considered in this study are summarized in Appendix A. The design parameter of PI speed controller is given in Appendix B and for FLC speed controller is given in Appendix C. The performance of vector control induction motor drive with all the three speed controller are presented during starting, load perturbation and speed reversal. Transient, steady state

and dynamic behavior of the drive with PI speed controller is shown in Fig. 6, with FLC speed controller is shown in Fig. 7 and with neuro-fuzzy speed controller is shown in Fig. 8. The reference speed is set at 185 rad/sec. The electromagnetic torque T_e rises to maximum during starting of the motor from standstill and then settles down over remaining period (steady state condition). Same is for currents. At steady state load torque T_L has been increased to 12 Nm from 3 Nm at time $t=0.3$ sec. and suddenly decreased to 3 Nm at $t=0.5$ sec. Finally the motor which is operating at 185 rad/sec, suddenly its reference speed is changed to negative 185 rad/sec. Table I, II and III presents performance comparison during steady state operation, during transient operation and in time domain analysis respectively.

Table 1: Performance comparison during steady state operation

Controller	Speed (rad/sec)	Ripple	Torque (Nm)	Ripple
PI	0.1		0.0017	
FLC	0.008		0.0005	
NFC	0.004		0.0003	

Table 2: Performance comparison during transients

Controller	Starting Time (sec)	Reversal Time (sec)	Dip in Speed (rad/sec)	Rise in Speed (rad/sec)
PI	0.04	0.145	4.9	4.8
FLC	0.032	0.11	4.78	4.63
NFC	0.03	0.08	4.7	4.6

Table 3: Performance comparison in time domain analysis

Controller	Peak Over shoot	Peak Time (sec)	Rise Time (sec)	Settle Time (sec)
PI	0.1351	0.06	0.03	0.13
FLC	0.08	0.058	0.028	0.128
NFC	0.0054	0.057	0.026	0.11

The results shows better performance of NFC based IM drive as compare to conventional PI and FLC controller based IM drive under starting, load perturbation and speed reversal. Since fuzzy logic has tolerance for imprecision of data and neural network has tolerance for noisy data, their combination neuro-fuzzy is having good tolerance for the parameter variation particularly stator and rotor resistances.

Also, neuro-fuzzy controller is universal function approximator, it can very well approximate linear and non-linear functions, thus it is more versatile than a linear controller in dealing with nonlinear plant characteristics and hence it has better stability than the conventional linear controller. Above discussion shows NFC based vector control induction motor drive is robust for high performance IM drive.

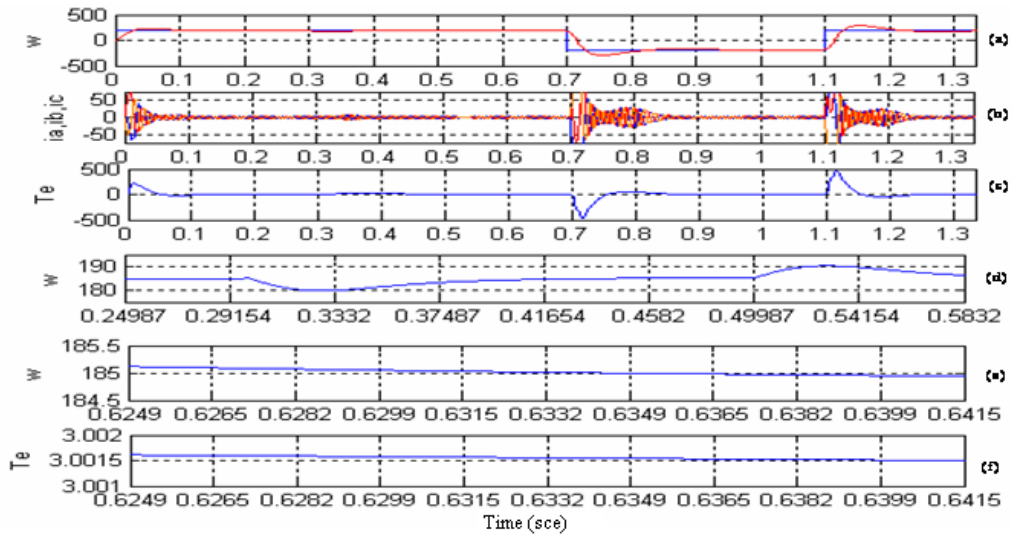


Fig.6. Performance Characteristics of Drive Scheme with PI- Speed controller (a) speed (rad/sec.) (b) current (amp.) (c) torque (Nm) (d) speed during loading cycle (e) speed ripples (f) torque ripples.

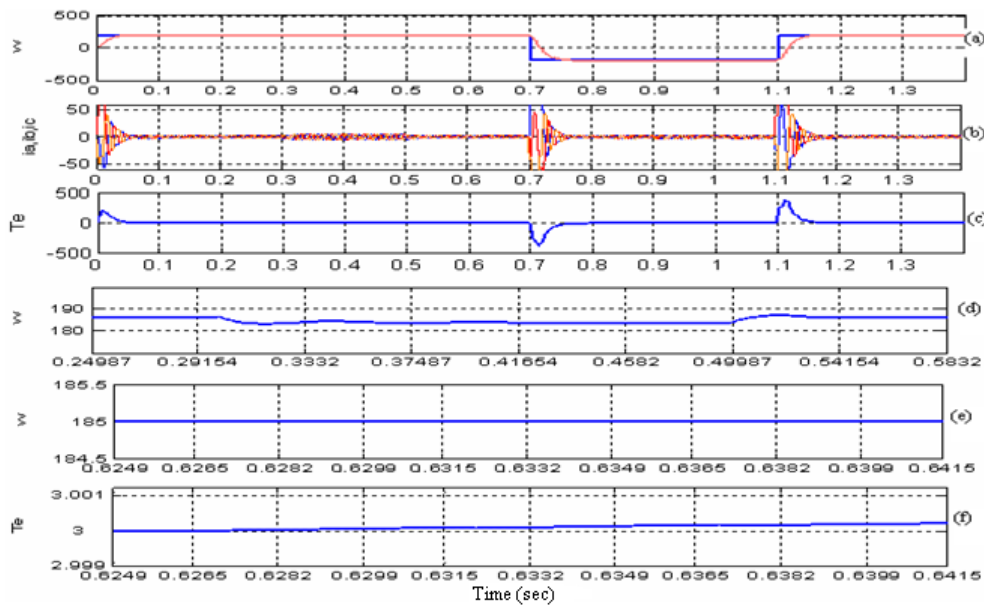


Fig.7. Performance Characteristics of Drive Scheme with FLC- Speed controller (a) speed (rad/sec.) (b) current (amp.) (c) torque (Nm) (d) speed during loading cycle (e) speed ripples (f) torque ripples

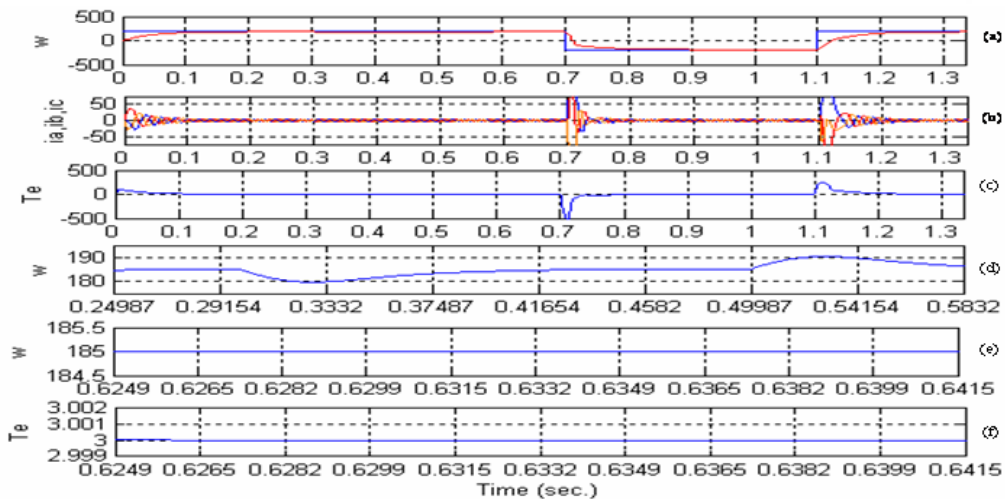


Fig. 8. Performance Characteristics of Drive Scheme with ANFIS- Speed controller (a) speed (rad/sec.) (b) current (amp.) (c) torque (Nm) (d) speed during loading cycle (e) speed ripples (f) torque ripples

V. CONCLUSION

A novel Neuro-fuzzy controller based vector controlled induction motor drive has been presented in this paper. Some of the advantages of ANFIS are reduced number of rules, faster speed of operation and no need for modifications in membership function by conventional trial and error method for optimal response. This makes NFC a easy-build and robust controller. The performances of the proposed NFC based drive have been investigated at various operating conditions. A performance comparison between PI based drive, FLC based drive and the proposed NFC based drive has been presented. The proposed NFC based IM drive has been found to be robust for high performance drive application.

Appendix A

The parameters of induction motor are as follows:

Nominal power (P):2.2KW; Voltage: 460V (L-L, rms); Phases: 3; Frequency: 60Hz; Stator resistance (R_s):1.77 ohms; Rotor resistance (R_r):1.34 ohms; Stator leakage reactance (X_{ls}):5.25 ohms; Rotor leakage reactance (X_{lr}):4.57 ohms; Mutual reactance (X_m):139 ohms; Rotor inertia (J): 0.025 Kg.m²; Number of pole (p): 4.

Appendix B

The design parameters of PI speed controller are as follows:

Proportional constant (K_p): 0.62445; Integral constant (K_i):0.01.

Appendix C

The design parameters of FLC speed controller are as follows:

Inputs to the FLC speed controller are speed error and rate of change of speed error and output is command current. Membership functions for input and output variables have been chosen with triangular shapes as shown in Fig. 9. Universe of discourse of input and output variables are divided in to seven fuzzy sets: NL (Negative Large), NM (Negative Medium), NS (Negative Small), ZE (Zero), PL (Positive Large), PM (Positive Medium), PS (Positive Small). Rule base for FLC speed controller is given in Table 4. Max-Product inference method and centroid defuzzification method are used.

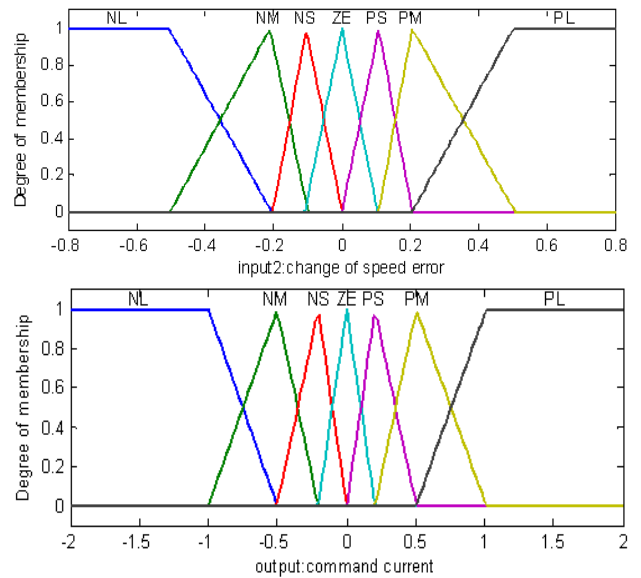
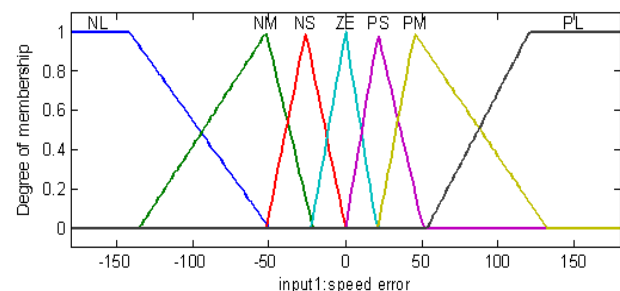


Fig. 9. Input and output membership function of FLC speed controller

Table 4: Rule base for FLC speed controller

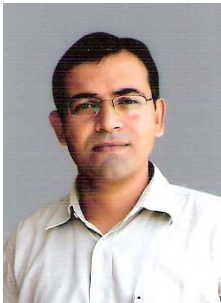
we \ cwe	NL	NM	NS	ZE	PS	PM	PL
NL	NL	NL	NL	NL	NM	NS	ZE
NM	NL	NL	NL	NM	NS	ZE	PS
NS	NL	NL	NM	NS	ZE	PS	PM
ZE	NL	NM	NS	ZE	PS	PM	PL
PS	NM	NS	ZE	PS	PM	PL	PL
PM	NS	ZE	PS	PM	PL	PL	PL
PL	ZE	PS	PM	PL	PL	PL	PL

REFERENCES

- [1] P. Vas, ‘Sensorless Vector and Direct Torque Control’ (London, U.K.: Oxford Science Publication, 1998).
- [2] R. Krishnan, ‘Electric motor drives modeling, analysis and control’ (PHI Pvt. Ltd., New Delhi, 2003).
- [3] Kumar, Rajesh, Gupta, R.A. and Singh, Bhim. (December 2006), ‘‘Intelligent Tuned PID Controllers for PMSM Drive -A Critical Analysis’’, in the Proc. of IEEE International Conference on Industrial Technology (ICIT2006),Mumbai, INDIA, pp. 2055-2060.
- [4] Z. Ibrahim and E. Levi, ‘‘A comparative analysis of fuzzy logic and PI speed control in high-performance AC drives using experimental approach,’’ IEEE Transl. On Ind. Appli, Vol. 38, No.5, pp. 1210–1218, Sep/Oct. 2002.
- [5] M.V. Aware, A.G. Kothari and S.O. Choubbe, ‘‘Application of adaptive neuro-fuzzy controller (ANFIS)for voltage source inverter fed induction motor drive,’’ in the Proc. of IPEMC 2000 Conf., Vol. 2, 15-18 Aug 2000, pp. 935–939.
- [6] Tae-Chon Ahn, Yang-Won Kwon, Hyung- Soo Hwang and Pedrycz, W, ‘‘Design of neuro-fuzzy controller on DSP for real-time control of induction motors,’’ in the Proc. of NAFIPS Conf., Vol. 5, 25-28 July 2001, pp. 3038–3043.
- [7] M. N. Uddin and H. Wen ‘‘Development of a self-tuned neuro-fuzzy controller for induction motor drives,’’ in Conf. record of Industry Applications 2004, Vol. 4, 3-7 Oct. 2004, pp. 2630–2636.
- [8] P. P. Cruz, J. M. Aquino and M. R. Elizondo, ‘‘Vector control using ANFIS controller with space vector modulation [induction motor drive application],’’ in the Proc. of UPEC Conf., Vol. 2, 6-8 Sept. 2004, pp. 545–549.

- [9] A. Miloudi, E.A.A Radadi, A. Draou and Y. Miloud, "Simulation and modeling of a variable gain PI controller for speed control of a direct torque neuro fuzzy controlled induction machine drive," in the Proc. of IEEE PESC 2004 Conf., Vol. 5, 20-25 June 2004, pp. 3493–3498.
- [10] Zhi Rui Huang and M.N. Uddin, "Development of a simplified Neuro-Fuzzy controller for an IM drive," in the Proc. Of IEEE International Conf. on Industrial Technology 2006 , 15-17 Dec. 2006, pp. 63–68.
- [11] M. N. Uddin Z. R. Huang and Md. M. Chy "A simplified self-tuned neuro-fuzzy controller based speed control of an induction motor drives," in the Proc. Of PES General Meeting 2007, 24-28 June. 2007, pp. 1–8.
- [12] Matlab, Simulink user guide, The Math Works Inc., 2003.
- [13] J.S.R. Jang, C.T. Sun and E. Mizutani, 'Neuro-Fuzzy and soft computing- A computational approach to learning and machine intelligence' (PHI Pvt. Ltd., New Delhi, 2006).
- [14] J.S.R. Jang, 'ANFIS: Adaptive-Network-Based-Fuzzy-Inference-System' IEEE Trans. on Systems, Man and Cybernetics, Vol. 23, No. 3, May 1993, pp. 665-685.

BIOGRAPHIES



Rajesh Kumar received the B.Tech. degree in Electrical Engineering from the National Institute of Technology (NIT), Kurukshetra, India in 1994, the M. E. degree in Electrical Engineering from the Malaviya National Institute of Technology (MNIT), Jaipur, India in 1997 and the Ph.D. degree in Intelligent systems from University of Rajasthan, India in 2005. In 1995 he joined as Lecturer with the Department of Electrical Engineering, MNIT, Jaipur and now working as Reader at the same institute. His research interests

include Intelligent Control, Evolutionary Algorithms, Fuzzy and Neural methodologies, Power Electronics and drives. Dr. Kumar received the Career Award for Young Teachers (CAYT) from Govt. of INDIA in 2002. He is a member of IEEE, fellow of IETE, member of Institute of Engineers (INDIA), member of IEANG and life member of Indian Society for Technical Education (ISTE).



R. A. Gupta was born in Chandera, Rajasthan, India, in 1956. He received B.E. (Electrical) and M.E. Degrees from the University of Jodhpur, India in 1980 and 1984, respectively and Ph.D in 1994 from IIT, Roorkee, India. In 1982, he joined as an Assistant Professor in the Department of Electrical Engineering, University of Jodhpur. In November 1990, he joined as a Reader and become full Professor in 1999 at the Department of Electrical Engineering, MREC, Jaipur (INDIA). His field of interest includes power electronics, electrical machines and drives. Prof. Gupta is a fellow of Institute of Engineers (INDIA), member of IEEE, a life member of (ISTE) and Indian Society for continuing Engineering Education.



Rajesh S Surjuse received the B.E. and M.Tech. degree in electrical engineering from the Visvesvaraya National Institute of Technology (VNIT), Nagpur, India in 1994 and 2003 respectively. In 1995, he joined as Lecturer with the Department of Electrical Engineering, Govt. Polytechnic Yavatmal, India and now working as a senior Lecturer in the Department of Electrical Engineering, Govt. Polytechnic Nagpur, India. He is a student member of IEEE and life member of Indian Society for Technical Education

(ISTE). At present he is research scholar at Malaviya National Institute of Technology (MNIT) Jaipur, India.. His primary area of research includes Power Electronics and Electrical Drives and control.

High Voltage Multilevel DC-DC Converter in Auto Balancing Mode

Vasudeo B Virulkar.¹ Sharad W Mohod.² Mohan V. Aware³

Abstract — In this paper balancing theory of a three level DC-DC converter is presented. It is proposed to make dc link voltages balanced across the capacitor stack. This voltage distribution gets equally distributed by selecting the appropriate switching frequency. This work is to investigate the new control scheme to incorporate the current adaptive switching in DC-DC converters. The major advantage of this novel scheme is to develop the bi-directional high voltage multilevel converters required in many high power industrial applications. A systematic approach and mathematical study is presented. Simulation results validates this proposed scheme.

Keywords - Adaptive current control, DC-DC bi-directional Converter, High power converters.

I. INTRODUCTION

Multilevel DC-DC converters are mostly used in high power applications in many industrial applications. They offer advantage of operating at relatively high DC bus voltages with reduced harmonic content, low EMI and low voltage stress on the devices. Multilevel converters can achieve smoother and less distorted AC-DC, DC-AC, and DC-DC power conversion. These technologies are used in the utility and large motor drives applications. These are presented in many of the literature [1].

In multilevel converters, DC bus capacitor banks are stacked in series. These converters will meet more voltage balance problem than that in AC-DC or DC-AC converter. Because of the asymmetric DC output voltage, fewer redundant switching states will be available in DC-DC multilevel converter. Also the difference of characteristics for each individual component, either on semiconductors or on passive components, will cause the voltage unbalance [2]-[7],[10]-[11].

In most cases, a dynamic balance control strategy is necessary to balance the capacitor voltages, which requires enough redundant switching states.

The transfer of energy from one end to another in DC – DC converter is of application dependent and also decided by the type of load.

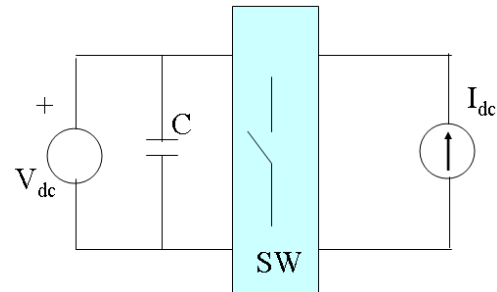


Fig 1: Generalized converter

The most convenient structure is to control the load current while maintaining the source side voltage constant across the supply side. This simple configuration is presented in figure 1. The industrial application of bi-directional DC/DC converters is for the interfacing the energy storage device like Superconducting Magnetic Energy Storage (SMES) coil to the power system through the voltage source inverters to mitigate the power quality problems. The SMES coil is charged from the power system under the normal operating condition and discharge in case of real power demand by the power system. The interface of the coil to inverter is across the dc link has to be at the high voltage level. This causes the dc capacitor and inverter semiconductor components to operate on high stress levels. Therefore the multilevel DC/DC converters are preferred. However, this leads to have multiple dc stages with capacitors. The voltages across these dc stages are governed by converter operating conditions. It is necessary to maintain the dc voltage constant during the converter operation [8]. There are various dc voltage balancing control strategy involving the additional sensor and control circuits [9]. In this paper, dc voltage balancing is achieved with proposed control strategy.

The energy balance theory with basic circuit laws can be used for analysis this circuit. However, the controlled power conversion process involves the switching structure of the DC-DC converters. One such converter structure is analyzed in this paper. In this paper, analysis of DC-DC converter is presented with the voltage balancing across the capacitor. The typical design considerations are also presented. In figure 2, three level topology of a proposed DC-DC converter is shown.

The operating principal of the three level DC-DC converter and current adaptive switching control is presented. The benefits of the proposed circuit with high power capability are as under.

- Voltage balancing at DC bus
- Soft-switching is realized
- High power applications
- Lower cost due to high frequency transformer
- Use of multilevel structure can reduce the Total Harmonic Distortion (THD).

The paper first received 2-Jun-2009 and in revised form 1-Sept- 2009.
Digital Ref: A17050214

¹ V.B.Virulkar is Research Scholar with the Department of Electrical Engineering, Visveshvaraya National Institute of Technology, Nagpur, Maharashtra, INDIA. E-mail: vbvirulkar@yahoo.com

² S.W Mohod is with Electronics Engineering Department, Ram Meghe Institute of Technology & Research, Badnera, Amravati Maharashtra E-mail: shardmohod@rediffmail.com

³ M.V. Aware is with the Department of Electrical Engineering, Visveshvaraya National Institute of Technology, Nagpur, Maharashtra, INDIA E-mail: mva_win@yahoo.com

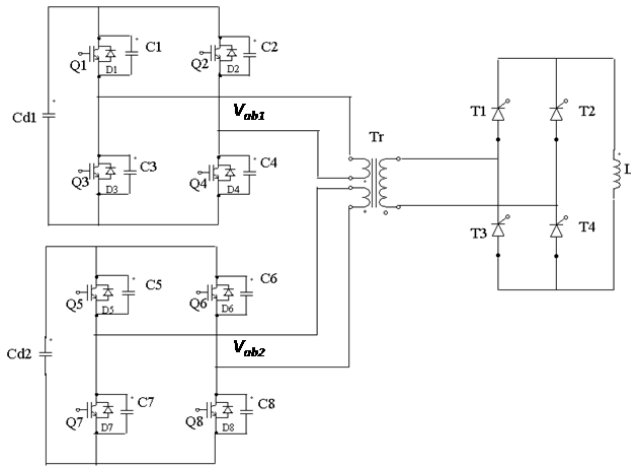


Fig 2: Multi level converter

II. CONVERTER OPERATION

The circuit topology is shown in figure 2 is analyzed for its operation. The one complete cycle is presented in the following figures. The circuit is built with the switches Q1-Q8 and C1-C8 capacitors connected across them. The secondary of the transformer (T_r) is having full bridge converter connected to the inductor coil (L). The switching signals to H bridge on primary side and for the full bridge thyristors on secondary are shown in figure 3 (a) and (b) respectively. The voltages and currents across the each primary winding of the transformer is shown in figure 4. The secondary side currents (I_{T1} , I_{T2}) and voltages are shown in figure 5.

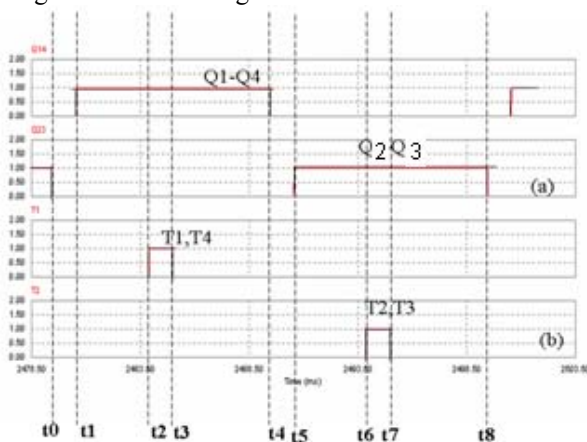


Fig 3: (a) Switching pulses for H-bridge on primary and (b) bridge on secondary side of the transformer

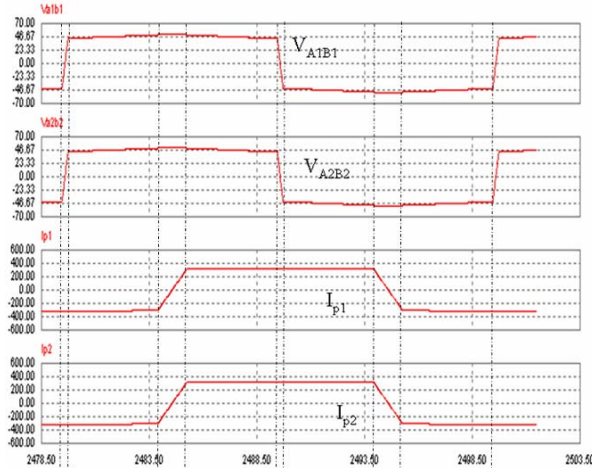


Fig 4: Voltages V_{A1B1} , V_{A2B2} and currents I_{p1} and I_{p2}

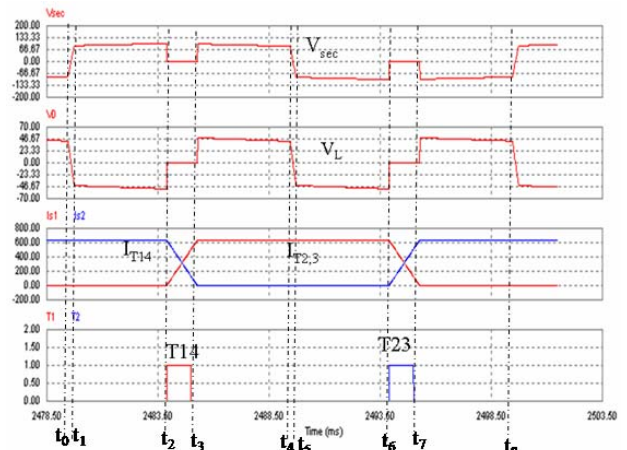


Fig 5: Output voltage- V_{sec} and coil voltage- V_L and with thyristor currents I_{T14} and $I_{T2,3}$ with respect to switching pulses

The switch Q2 and Q3, Q6 and Q7 at the t_0 instant are off and circuit is shown in figure 6. The time t_0-t_1 indicates the blanking time and its operating condition is indicated in figure 7. The operation of the switching, Q1 and Q4, Q5 and Q8 indicates the discharging operation during the time t_1-t_2 . This is shown in figure 8. The change over of the switching on secondary side by triggering the thyristors is shown in the figure 9. This is causing current (I_{T23}) to transfer to another pair of thyristor. This current transfer is due to the voltage (V_L) applied across the coil. The average current through the coil (I_o) is constant and maintains its direction. After this half cycle, the charging cycle starts as the voltage across coil is positive. The subsequent operation is shown in figure 10, 11 and 12.

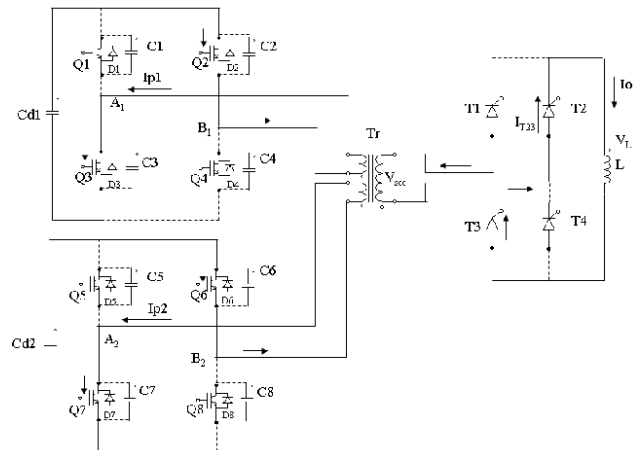


Fig 6: Operation at t_0

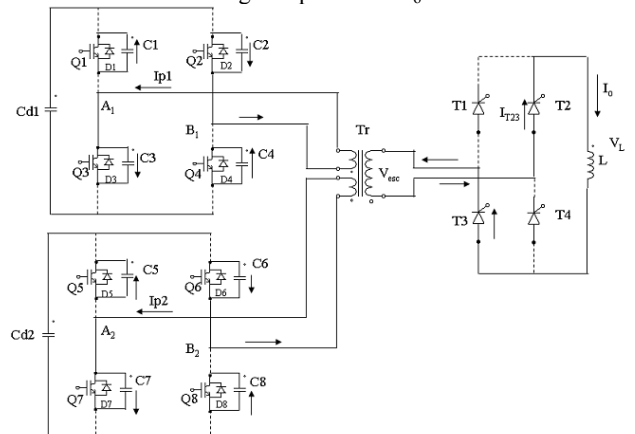


Fig 7: Operation during t_0-t_1

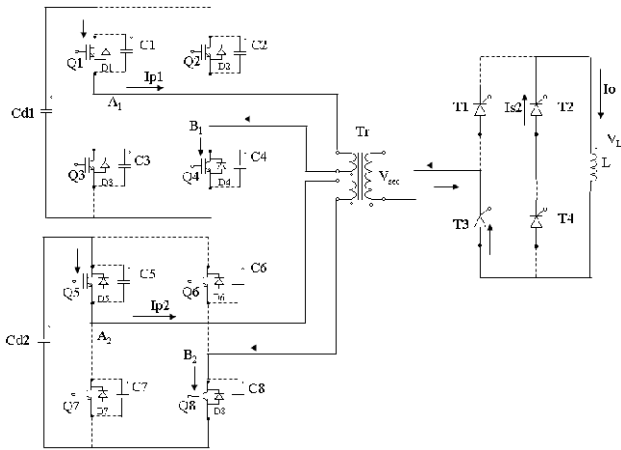


Fig 8: Operation during t_1-t_2

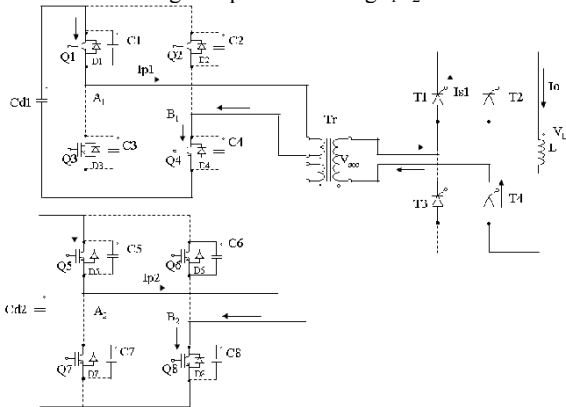


Fig 9: Operation during t_2-t_3

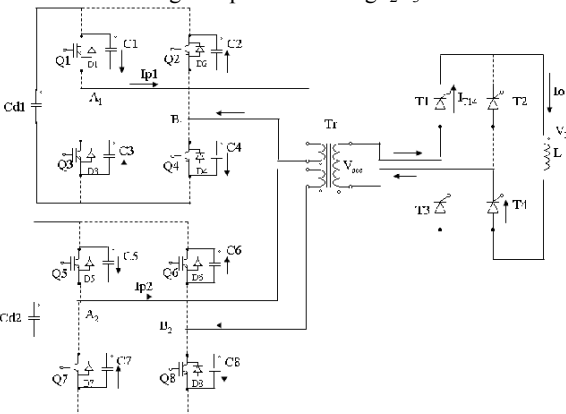


Fig 10: Operation during t_3-t_4

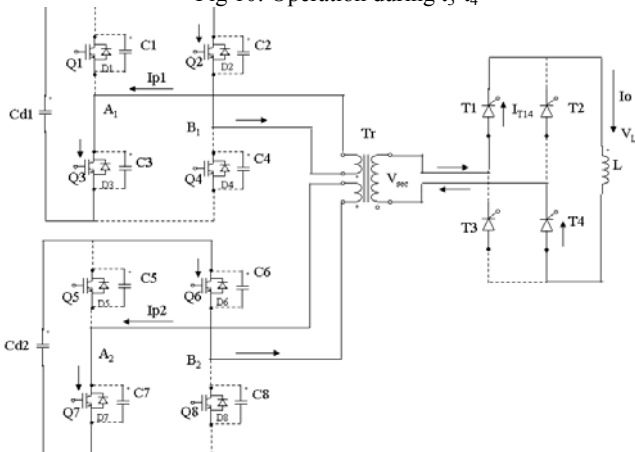


Fig 11: Operation during t_4-t_5

III. BALANCING THEORY OF MULTI-LEVEL CONVERTERS

The equivalent circuit for H- bridge under energy transferred across the transformer, that is from capacitor to inductive coil and from coil to capacitor is shown in figure 13 (a) and (b) respectively.

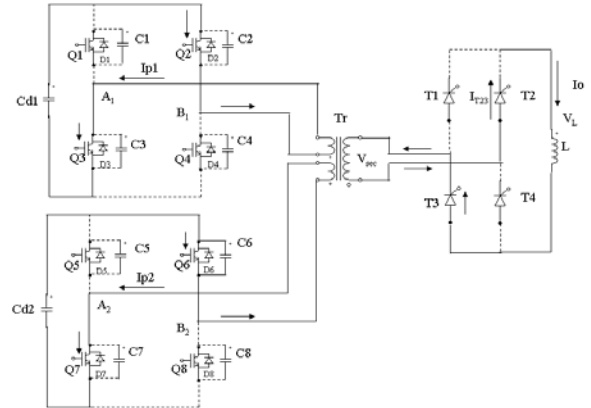


Fig 12: Operation during t_5-t_6

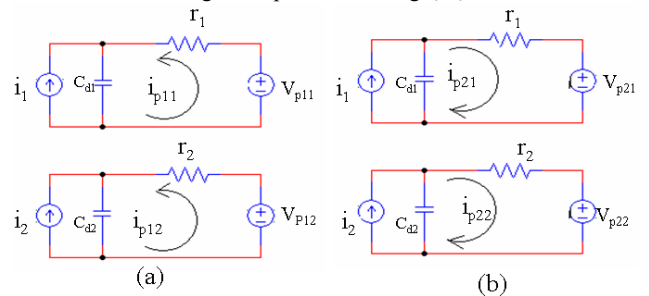


Fig 13: Circuit equivalent stages under first and third stage

The energy transfer across the transformer is simply represented from current source (i_1) and voltage source (V_{p11}) with one stage converter having equivalent resistances r_1 , representing the drop across converter and transformer winding. Similarly another winding is also represented.

The mathematical analysis is carried out with these circuits. The ampere turns across the transformer winding is written as

$$N_p * (i_{p11} + i_{p12}) = N_s * I_0 \quad (1)$$

The N_p and N_s represents the primary and secondary number of turns respectively. The current through coil is I_0 .

$$i_{p11} + i_{p12} = \frac{I_0}{K} \quad (2)$$

Where, K is the turns ratio.

Assuming that the sum of the voltage across C_{d1} and C_{d2} are $2V$, the voltage across C_{d1} is $V + \Delta V$ and the voltage across C_{d2} is $V - \Delta V$, then from figure 3, current equations can be written as

$$i_{p11} = \frac{V_{p1} - (V + \Delta V)}{r_1}, i_{p21} = \frac{V_{p11} - (V + \Delta V)}{r_1} \quad (3)$$

$$i_{p12} = \frac{V_{p1} - (V + \Delta V)}{r_2}, i_{p22} = \frac{V_{p12} - (V + \Delta V)}{r_2} \quad (4)$$

The average current on the primary can be written as

$$i_{p1} = \frac{\frac{V_{p1} - (V + \Delta V)}{r_1} T_1 + \frac{V_{p2} - (V + \Delta V)}{r_1} T_2}{T} \quad (5)$$

$$= \frac{V_{p1} - (V + \Delta V)}{r_1} d + \frac{V_{p2} - (V + \Delta V)}{r_1} (1-d)$$

$$i_{p2} = \frac{V_{p1} - (V + \Delta V)}{r_2} d + \frac{V_{p2} - (V + \Delta V)}{r_2} (1-d) \quad (6)$$

The period $T_1 = t_2 - t_0$ and $T_2 = t_4 - t_3$, can be represented in terms of duty cycle $d = \frac{T_1}{T}$, and $\frac{T_2}{T} = 1 - d$.

The difference of current is Δi_p on the primary side is

$$\begin{aligned} \Delta i_p &= i_{p1} - i_{p2} \\ &= \frac{[V_{p1} - (V + \Delta V)r_2] - [V_{p1} - (V - \Delta V)]r_1}{r_1 r_2} d \\ &\quad + \frac{V_{p2} - (V + \Delta V)r_2 - [V_{p2} - (V - \Delta V)]r_1}{r_1 r_2} (1-d) \end{aligned} \quad (7)$$

The unbalance due to equivalent resistance of these two stages can be represented with the reference value of resistance R . Which is represented as $r_1 = R$ and $r_2 = R + \Delta R$.

From above equations and after simplification it is represented as

$$\Delta i_p = \frac{-2\Delta V R - \Delta R[(V_{p2} - V_{p1})d + V - V_{p2}]\Delta R \Delta V}{R(R + \Delta R)} \quad (8)$$

Neglecting the term $\Delta R \Delta V$ and considering the balance of the charging and discharging mode, the currents are represented as $(i_{p11} + i_{p12}) = -(i_{p21} + i_{p22})$. By

substituting the values of currents and simplifications $[4V - 2(V_{p1} + V_{p2})]R + [2V - (V_{p1} + V_{p2})]\Delta R + \Delta R = 0$ (9)

It can be written as

$$2V - (V_{p1} + V_{p2}) = 0 \quad (10)$$

This gives the value of voltage V as

$$V = \frac{V_{p1} + V_{p2}}{2} \quad (11)$$

From equation 2, it can be written as

$$V_{p1} - V_{p2} = 2 \frac{I_0}{K} * \frac{R(R + \Delta R)}{(2R + \Delta R)} \quad (12)$$

Substituting these values of voltages in the equation 8,

$$\Delta i_p = \frac{-2\Delta V R - \Delta R \left(\frac{1}{2} - d \right) 2 \frac{I_0}{K} * \frac{R(R + \Delta R)}{(2R + \Delta R)}}{R(R + \Delta R)} \quad (13)$$

The current flow in capacitors are

$$i_{cd1} = (i_1 + i_{p1}), i_{cd2} = (i_2 + i_{p2}) \quad (14)$$

$$\Delta i_{cd} = i_1 + i_{p1} - (i_2 + i_{p2}) = \Delta i + \Delta i_p \quad (15)$$

combining (13) and (15), the effective current difference is written as

$$\Delta i_{cd} = i_1 - i_2 + \frac{-2\Delta V R - \Delta R \left(\frac{1}{2} - d \right) 2 \frac{I_0}{K} * \frac{R(R + \Delta R)}{(2R + \Delta R)}}{R(R + \Delta R)} \quad (16)$$

From the above equation, if the current Δi_{cd} is positive then current flowing in to the C_{d1} is larger than current flowing into the C_{d2} , and the voltage across C_{d1} raises relatively more than the C_{d2} . It will be reverse if the Δi_{cd} is negative. If $i_1 = i_2$ then Δi_{cd} become

$$\Delta i_{cd} = \frac{2\Delta V}{R} \quad (17)$$

If ΔV is positive and Δi_{cd} becomes negative, a very small voltage difference will result in a very large Δi_{cd} , which will cause the voltage across the C_{d1} diminish relatively very quickly to the voltage across C_{d2} . The voltage ΔV will decrease quickly to zero. The voltage balance will be achieved across the C_{d1} and C_{d2} .

The difference of voltage ΔV is more sensitive to the change in converter current and the equivalent resistance of the switches and circuit components. The design parameters of the converters are selected to maintain the voltage drop near to zero to operate this bidirectional converter in stable condition. One of the control factors to achieve the voltage balance is to operate the converter with selected switching frequency zone. This is one of the most important parameters to make these converters operations more robust and economical. The concept of variable switching frequency control through adaptive current control is introduced and presented in next section.

IV. ADAPTIVE CONTROL OF DC-DC CONVERTER

The control scheme is incorporated to maintain the voltage balance across the dc link capacitors by sensing the dc voltages and controlling the switching frequency. The dc link capacitor and front end high frequency transformer are the two components, which selects the switching frequency. By keeping the duty ratio constant, frequency is varied through the current balance sensing circuit. The limit is decided upon the maximum allowable safe operating voltages required for the DC converters. Analysis indicates the balances are maintained from no load to full load operating conditions with 15-20 % variation in switching frequency.

The inductive coil current regulation is carried out by regulating the switching pulses of thyristors. This regulates the energy storage in the inductor. There are three stages of operation. In the first case, the current is maintained constant, in the second, coil current is increased and in third case, current is reduced. The pulse position is shown in the figure 14. The thyristor pulse width is 20° and positioning of the pulses for both the thyristors are placed 180° apart. The location of the pulse in the half cycle decides the charging or discharging. To maintain the current through the coil constant, these pulses are to be located at 90° in each half cycle. The average coil current is constant. If the charging is required then the pulses are to be moved above 90° and for discharging the pulses are to be placed below the 90° . The reference for this is considered with the storage capacity of the inductor coil.

The control of current in coil is one variable while the dc voltage across the capacitors is another.

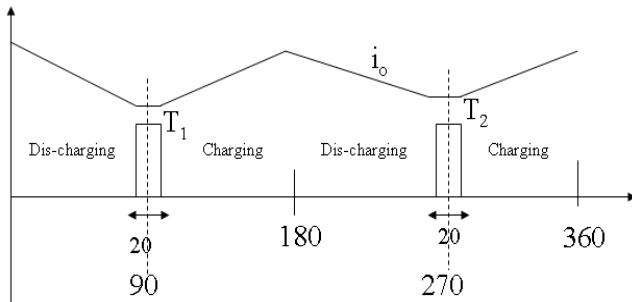


Fig 14: Charging and discharging pulse positions

The control scheme is implemented as shown in figure 15. The reference current set for the coil is generally a maximum current to which the coil can be charged. This reference can be made adaptive with system load current to get the advantage of the off-period availability of the power. This can be made to follow the load demand if the system is interfaced with the power system with the balance voltage source inverters. The switching of DC-DC multilevel converter is set to the frequency from 50 Hz to 5 kHz. This is depending on the power handling capacity of the converter. The switching frequency will be low as the power rating of the converter is more. The frequency is regulated by using voltage controlled oscillator (VCO). The required control on position (α) of the pulses for the half bridge converter is generated through the synchronizing circuit. The charging or discharging mode is regulated by comparing the actual coil current with the set reference value of the current. This control algorithm can be implemented on digital signal processor.

V. PERFORMANCE OF THE CONVERTER

This control with the circuit considering the IGBT switches is simulated in the PSIM. The design parameters are chosen to make it more realistic so that the prototype could be built. The simulation parameters are given in the Table-I. The switching frequency of the DC-DC converter is set to visualize the operating of the converter switches on both the sides of the transformer. The voltages across the switch (Q1) are shown with the capacitor voltage (C1) in the figure 16. The switching of these devices takes place exactly at the zero voltages.

This confirms the ZVS operation. Similarly the secondary side converter is operating at the zero current (ZCS). This is observed from the current and operating pulses as shown in the figure 17. The results of simulation indicating the charging operation of the coil is presented in figure 18. The charging current is indicated with the time period of charging and discharging. In the charging mode, the discharging period is always less than the charging time period to push the storage of the energy. This indicates the pulse positioning of the thyristors on secondary side of the transformer governs the control of coil current. The capacitor voltages across each of the stages (V_{d1} and V_{d2}) and current I_o is shown in figure 19.

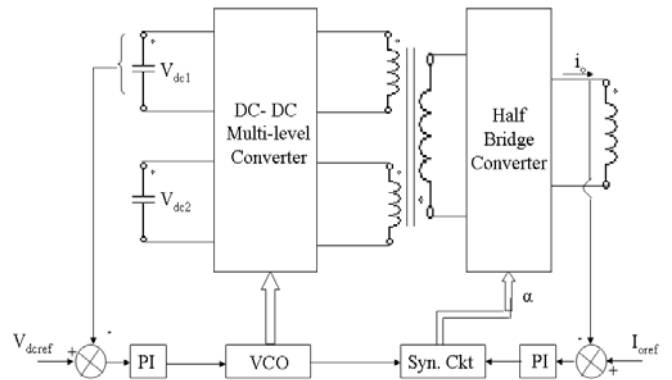


Fig 15: Control scheme for DC-DC converter

The effective charging of the current with the balancing of the voltage are taking the place. The voltages on these capacitors are set to a value of 500 volts and 300 volts and charging starts from the zero current in the coil. The final steady state is achieved where both the capacitors are having same voltages. This voltage is 40 volt. The current increases in the coil up to the value of 550 amps.

Table 1: Simulation parameters

C_{d1}, C_{d2}	$20e^{-2}$ F	V_{d1} - Volts	300
L	0.1 H	V_{d2} -Volts	500
C_1-C_8	$10 e^{-4}$	I_o -Amps	0-1000
Sw. Freq.	50 Hz	Thy. pulse width	20°
Tr-leakage inductance (Primary)	0.0001	Tr-leakage inductance (Secondary)	0.0000 1

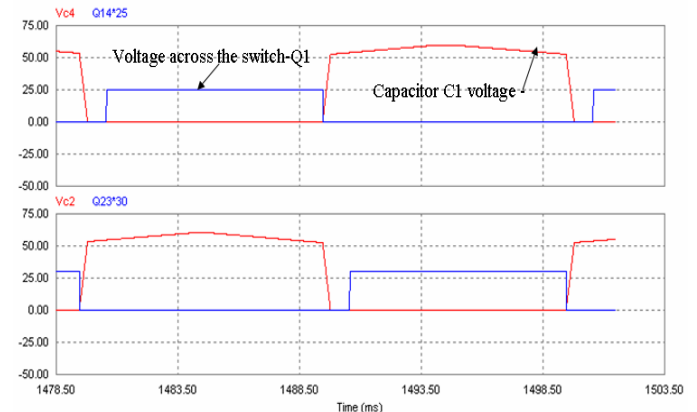


Fig 16: Voltages across the switch Q1 and capacitor C1-A ZVS operation

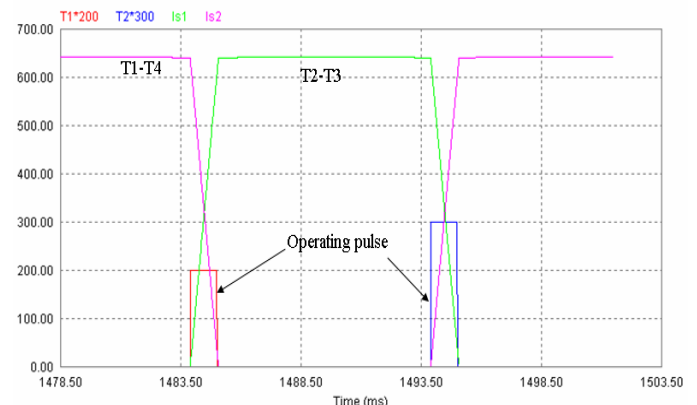


Fig 17: Currents through the thyristor- T1 and T4 and T2-T3 (ZCS operation)

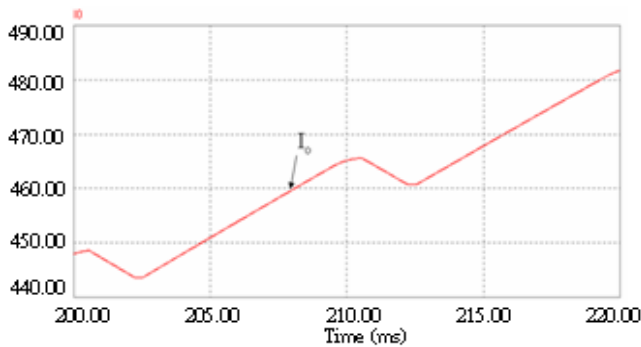


Fig 18: Coil charging-charging period is more than discharging

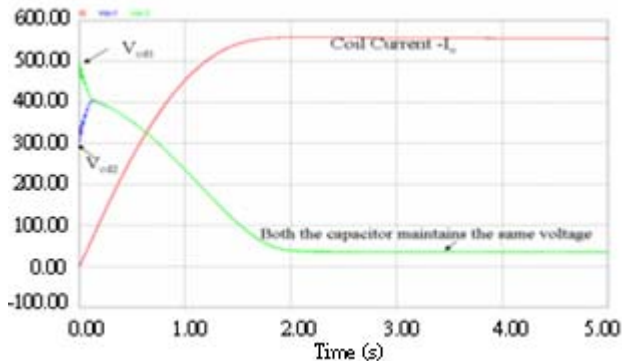


Fig 19: Capacitors voltages are balancing with the charging coil current

VI. CONCLUSION

In multi level DC-DC converters, voltage across the DC bus is more sensitive and often interferes in its operation. This paper presents the analysis of the voltage balancing at the dc bus of multi- level converters. The high power converter design with selection of circuit parameters is also presented. The operation of the circuit indicates the multi-level dc-dc converters gets balance with the appropriate switching of the H-bridge. The control scheme proposed also regulates the coil current. The new adaptive current controlled auto balancing is implemented to get stable operation of multilevel DC-DC converter. This converter works in soft switching mode hence over all efficiency and operating stability is ensured with more economical design. This has applications in interfacing of superconducting magnetic energy storages to be interfaced with the power system.

REFERENCES

[1] J. S. Lai and F. Z. Peng, "Multilevel converters-A new breed of power converters," IEEE Trans. Ind. Applications, Vol.32, May/June 1996, pp.509-517.
 [2] F. Zhang, F. Z. Peng, and Z. Qian, "Study of the multilevel converters in DC-DC Applications," IEEE POWER Electronics Specialists Conference June 2004, pp. 1702-1706.
 [3] J. Kung, and B.T.Ooi, "Series connected voltage source converter modules for forced commuted SVC and DC transmission", IEEE Trans. Power Deliv., Vol.9, No.2, April 1994, pp.977-983.
 [4] F.Z.Peng, "A generalize multilevel inverter topology with self voltage balancing". IEE Trans. on Industry Appl.,Vol.37,No.2, , March/April 2001, pp. 611-618.
 [5] E. Deschamps and I. Barbi, "A flying-capacitor ZVS 1.5 kW dc-to-dc converter with half of the input voltage across

the switches," IEEE Trans Power Electronics, Vol. 15, Sept. 2000, pp. 855-860
 [6] S. Hamada et al., "A novel zero-voltage and zero-current switching PWM dc-dc converter with reduced conduction losses," IEEE Trans. Power Electron. Vol. 17, May 2002, pp. 413-419
 [7] F. Krismer, J. Biela, J. W. Kolar, "A comparative evaluation of isolated bi-directional DC-DC converters with wide input and output range," IEEE Industry Application Conference 2005, pp 599-606 vol. 1
 [8] Shigenori Inou, Hirofumi Akagi "Voltage Control of a Bi-directional Isolated DC-DC converter for medium voltage motor drives," IEEE Power Converters Conference Nagoya-2007 pp. 1244-1250
 [9] A. Nabae, I. Takahashi, and H. Akagi, " A new neutral-point-clamped PWM inverter," IEEE Trans. Ind. App., Vol. IA-17, No.5, sept/oct 1981, pp.518-523.
 [10] A. M. Trzynadlowski, Introduction to Modern Power Electronics, John Wiley, 1998.
 [11] N. Mohan, Power Electronics, converter, applications and Design, John Wiley, 1995.

BIOGRAPHIES



Vasudeo B. Virulkar received the B.E. degree in electrical engineering from the Nagpur University, Nagpur (M.S.), India, in 1991, the M.E. (EPS) degree from the Amravati University, Amravati, India, in 1997. After his post graduation, he worked as a Lecturer in Electrical Engineering at Department of Higher and Technical Education, Govt. of Maharashtra and worked at various institutions. Presently, he is working as Lecturer in Electrical Engineering at Govt.

College of Engineering, Amravati (M.S.), India and pursuing his research on Power Quality at Department of Electrical Engineering, Visvesvaraya National Institute of Technology, NAGPUR (INDIA) under the guidance of Prof. Mohan. V. Aware.



Sharad W. Mohod (M'2006) received B.E. in Electrical Engineering and M.E. from Govt. College of Engineering Aurangabad, India in 1988 and 1991 respectively. He has worked as an Electrical Engineer in M/S Garware Polyester Ltd Aurangabad from 1988-1991. In 1991, he joined College of Engineering Badnera - Amravati, and from 2000, he is working as Assistant professor in Dept. of Electronic Engineering., at Prof. Ram Meghe

Institute of Technology & Research Badnera-Amravati, India. Presently, he is pursuing his Ph.D. at Visvesvaraya National Institute of Technology, Nagpur, India. He is a member of IE (India), IETE, LMISTE.



Mohan V. Aware received the B.E. degree in electrical engineering from the Government College of Engineering, Amravati (M.S.), India, in 1980, M.Tech. degree from the Indian Institute of Technology, Bombay, India, in 1982, and the Ph.D. from Visvesvaraya Regional College of Engineering, Nagpur, India, in 2002. He worked as a Design Officer with Crompton Greaves Ltd., Nasik, India during 1982-1989.

During 1989-1991, he was Development Engineer with Nippon Denro Ispat, Nagpur. From 1991 to 2001, he was with Department of Electrical Engineering, Visvesvaraya Regional College of Engineering, as Lecturer and Scientist "C." From 2001 to 2003, he was a Research Associate with the Electrical Engineering Department, Hong Kong Polytechnic University, Kowloon, Hong Kong. Presently, he is working as a Professor in Electrical Engineering Department at Visvesvaraya National Institute of Technology, NAGPUR (INDIA).

Performance Investigation of Modified Self-Commutated CSI-fed Induction Motor Drive

Pramod Agarwal¹ A.K. Pandey² V.K. Verma¹

Abstract - The performance of modified self-commutating CSI-fed induction motor drive is investigated in this paper. The mathematical model of the complete drive system is developed in the synchronously rotating d-q reference frame to evaluate the performance of the drive. Closed form mathematical expressions are developed for the torque, phase voltage, efficiency, power factor, total loss etc. Performance of the drive is obtained experimentally and compared with the analytical results for validation

Keywords - Current Source Inverter, PWM Rectifier, Optimal Capacitor.

I. NOMENCLATURE

i_{as}, i_{bs}, i_{cs}	Line currents of the PWM inverter
v_s	Instantaneous stator phase voltage
i_c	Instantaneous phase current of capacitor
v_{ds}^e, i_{ds}^e	Voltage and current in d-axis stator winding in synchronous rotating reference frame
v_{qs}^e, i_{qs}^e	Voltage and current in q-axis stator winding in synchronous rotating reference frame
i_{dr}^e, i_{qr}^e	Current in d and q axes of the rotor winding in synchronous rotating reference frame
i_{cd}^e	Capacitor current in d axis winding in synchronously rotating reference frame
i_{cq}^e	Capacitor current in q axis winding in synchronously rotating reference frame
I_{act}	Active component of stator current
I_{react}	Reactive component of stator current
ω_e	Synchronous speed of the induction motor
ω_r	Rotor speed of induction motor
ω_{sl}	Slip speed of the induction motor
θ_e	Angular position of synchronous reference frame
I_{dc}	d.c. link current
t_e	Electromagnetic torque
t_l	Load torque
t_L	Rated load torque
V_{inv}	Input voltage of the inverter
I_{inv}	Input current of the inverter
V_r	Rectifier output voltage
r_f	Resistance of d.c. link inductor
l_f	Inductance of d.c. link inductor
l_{ss}, r_s	Self inductance and resistance of stator winding per phase
l_{rr}, r_r	Self inductance and resistance of rotor winding per phase
l_m	Mutual inductance per phase
l_1	l_s, l_r, l_m^2

C	Capacitance per phase
J	Moment of inertia in kg-m ²
B	Viscous friction coefficient
β	Pulse width of PWM rectifier
V_{LL}	Line to line input voltage of the rectifier
P	No. of poles

II. INTRODUCTION

The speed control of the induction motor is possible over a wide range by feeding the motor through a variable frequency Current Source Inverter (CSI). Due to controlled current operation of the inverter and thus inherent short circuit protection, slip regulated CSI is preferred over Voltage Source Inverter (VSI). The current source at the front end makes the system naturally capable of power regeneration without the need of extra converter as required in VSI. However, the line currents of conventional CSI-fed induction motor drive are non-sinusoidal in nature and have dominant low order harmonics. These lower order harmonics give rise to torque pulsation and hence, different PWM techniques in CSI are reported in

literature [1-5] which includes optimal PWM [2], speed pulsations. For the smooth speed control Programmed PWM [3] and Space Vector Modulation [5]. Another control technique to reduce the losses in the drives is presented in [6]. All these techniques are aimed to reduce the harmonics in the inverter output current but still the motor current is non-sinusoidal. To make the input power factor unity as well as motor current sinusoidal, techniques based on active filters are proposed in [11, 12]. The use of active power filter increases the cost and complexity.

In the present paper a modified self commutating CSI-fed induction motor drive is designed and developed so that the motor line voltages and currents are nearly sinusoidal over the wide range of the speed control. At the terminals of induction motor, a 3-phase capacitor bank is connected. The capacitor is designed such that it removes the harmonics from the machine currents over the wide operating frequency. The use of variable speed induction motor fed from variable frequency source for a particular application depends upon its steady state performance. The steady state analysis of the conventional current source induction motor drive has been reported in [7-10]. The aim of this paper is to investigate the steady state performance of the modified CSI drive. Simulation and experimental results are presented and compared to validate the mathematical model of the drive.

III. SYSTEM DESCRIPTION

The modified CSI fed induction motor drive consists of a three-phase ac source, PWM rectifier, dc link smoothing reactor, a current controlled inverter, a three-phase squirrel cage induction motor and three-phase

The paper first received 21 Feb. 2009 and in revised form 20 Aug 2009.
Digital Ref: A17050220

¹ Department of Electrical Engineering, Indian Institute of Roorkee, Roorkee, India

² Department of Electrical Engineering, Madan Mohan Malviya Engineering College, Gorakhpur, India

capacitor bank as shown in Fig 1. The input current source is realized using rectifier with current feed back. The output voltage of the rectifier is controlled using equal pulse width modulation technique. Thus the source current is having symmetrically placed equal width pulses which makes the input displacement factor unity and also reduces the harmonics injected into supply. The CSI output is controlled using space vector technique to reduce the harmonics in the output current. To operate the machine at a normal value of air gap flux, the motor is operated in statically unstable region of torque-slip characteristics using slip regulator in the feedback loop. The present work makes use of speed and current controllers of PI type. The actual speed of induction motor is measured by pulse encoder and compared with the reference speed set. The speed error is processed in the speed control loop to obtain the reference slip speed. Using slip regulator characteristics, the value of reference

active stator current of the induction motor and reference reactive current are determined corresponding to reference slip speed.

The reference stator current is obtained using stator active reference current, the stator reactive reference current and the capacitor current as shown in the Fig.1. The stator current vs. slip speed and reactive stator current vs. slip speed characteristics together determine the slip regulator characteristics. These characteristics are shown in Fig.2 and Fig.3 and are obtained experimentally. The figures show that active current increases linearly with slip and hence with load while the reactive current is nearly constant all through out. Using reference active current, capacitor rms current and stator reference reactive current, stator reference current is determined, which is transformed to the dc link side to obtain the reference dc link current. The reference slip speed is added to the actual rotor speed to obtain the switching frequency of the inverter

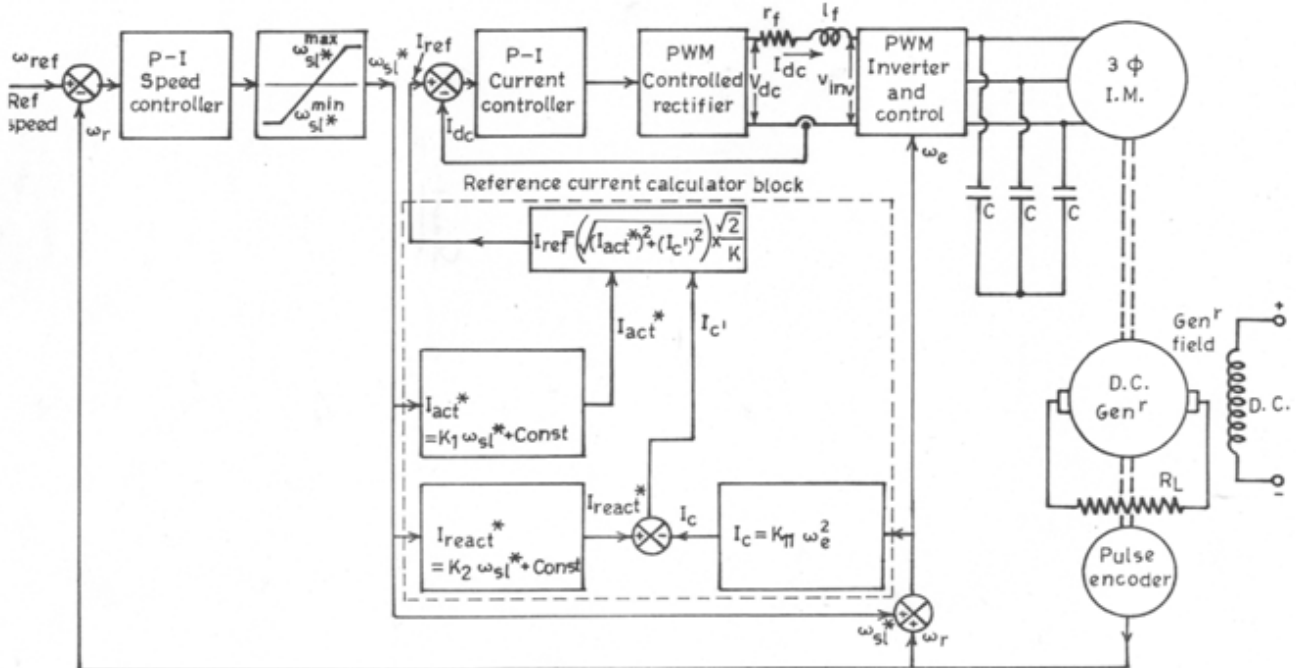


Fig 1: Variable speed modified current source inverter fed induction motor drive

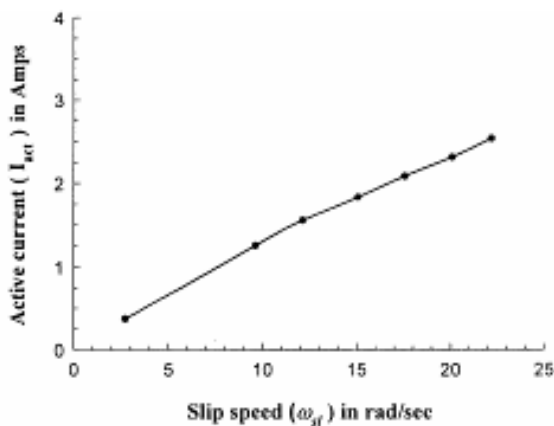


Fig 2: Active current vs slip speed characteristic

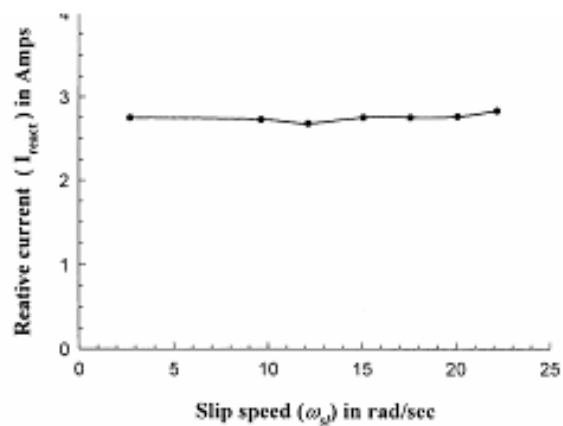


Fig 3: Reactive current vs slip speed characteristic

IV. MATHEMATICAL MODEL OF THE DRIVE

The modeling of the modified CSI fed induction motor drive is carried out in synchronously rotating reference frame.

Three-phase PWM Rectifier

The PWM rectifier output voltage depends upon the number of pulses per cycle and their widths. The converter is modeled for twelve numbers of equal pulses per cycle. It leads two pulses per 60° , each of β width. Fig.4 shows the output voltage waveform of PWM rectifier over a 60° interval.

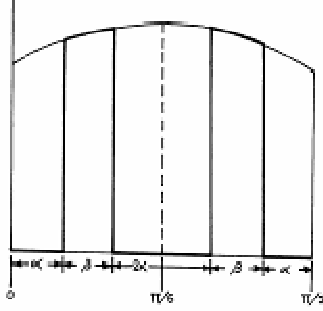


Fig 4: Output voltage of PWM Rectifier over 60°

The average output voltage of the rectifier can be obtained in terms of pulse width β and can be expressed with the following expressions:

$$V_r = \frac{3\sqrt{2}}{\pi} V_{LL} (4 \sin \frac{5\pi}{12}) \sin \frac{\beta}{2} \quad (1)$$

Since β is varied from 10% to 90% of $(\pi/6)$ radians, therefore,

$$\sin(\beta/2) \cong (\beta/2) \quad \text{and} \quad V_r = 5.218 V_{LL} (\beta/2) \quad (2)$$

Three Phase Pulse Width Modulated Inverter

The output of CSI is controlled using space vector modulation. The fundamental component of line currents of the 3-phase pulse width modulated inverter i_{as} , i_{bs} , i_{cs} forms a balanced set of 3-phase currents with a maximum value as $I_{as(max)}$ and can be expressed as

$$I_{as(max)} = k I_{dc} \quad (3)$$

where, k is obtained with the help of Fourier analysis different PWM techniques in CSI are reported in of inverter line current waveforms. The value of k depends upon the operating frequency of the inverter and it varies from 0.8485 to 0.9970 for variation in operating frequencies from 10 Hz to 50 Hz. The q^e axis of the rotating reference frame is assumed to coincide with the stator a-axis at $t = 0$ as shown in Fig.5.

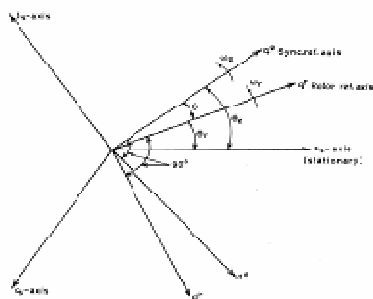


Fig.5: d-q reference frame

Since inverter output fundamental current peak is taken along the q^e axis of the reference frame, the transformed phase currents in the q^e - d^e reference frame are:

$$i_{0s}^e = 0; \quad i_{qs}^e = k I_{dc}; \quad i_{ds}^e = 0 \quad (4)$$

Assuming power loss in the inverter to be negligible, Inverter input power = Inverter output power

$$V_{inv} I_{inv} = v_{as} i_{as} + v_{bs} i_{bs} + v_{cs} i_{cs} = \frac{3}{2} (v_{qs}^e i_{qs}^e + v_{ds}^e i_{ds}^e) \quad (5)$$

Substituting the values of i_{qs}^e , i_{ds}^e and I_{inv} as I_{dc} , the inverter input voltage is obtained as:

$$V_{inv} = 1.5 k v_{qs}^e \quad (6)$$

DC Link

The rectifier output voltage V_r is expressed as

$$V_r = 1.5 k V_{qs}^e + (r_f + pL_f) I_{dc} \quad (7)$$

Three-phase Induction Motor

The induction motor can be modeled in q^e - d^e reference frame using the following assumptions.

- The three phase stator windings of the motor are balanced and sinusoidally distributed in space.
- The air gap flux is maintained at rated value.
- The motor line currents are sinusoidal due to capacitor at the motor terminals.
- The dc link current is ripple free.
- The switching transients in the inverter are ignored.
- There is no core loss in the induction machine.

The motor can be described by the following fourth-order matrix equation in q^e - d^e reference frame:

$$\begin{bmatrix} v_{qs}^e \\ v_{ds}^e \\ 0 \\ 0 \end{bmatrix} = \begin{bmatrix} r_s + pl_{ss} & \omega_e l_{ss} & pl_m & \omega_e l_m \\ -\omega_e l_{ss} & r_s + pl_{ss} & -\omega_e l_m & pl_m \\ pl_m & \omega_{sl} l_m & r_r + pl_{rr} & \omega_{sl} l_{rr} \\ -\omega_{sl} l_m & pl_m & -\omega_{sl} l_{rr} & r_r + pl_{rr} \end{bmatrix} \begin{bmatrix} i_{qs}^e \\ i_{ds}^e \\ i_{qr}^e \\ i_{dr}^e \end{bmatrix} \quad (8)$$

he electromagnetic torque equation of the motor is expressed as

$$t_e = \frac{3}{2} \cdot \frac{P}{2} \cdot L_m (i_{qs}^e i_{dr}^e - i_{qr}^e i_{ds}^e) \quad (9)$$

The equation of motion of the drive is expressed as

$$t_e = t_l + J \frac{d\omega_r}{dt} + B \omega_r \quad (10)$$

The load torque equation is given by:

$$t_l = t_L (\omega_r / \omega_{base}) \quad (11)$$

Three Phase Capacitor Bank

Assuming capacitor connected across the terminals of the stator to be loss less, the capacitor current is given as:

$$i_c = C \frac{dv_s}{dt} \quad (12)$$

Transforming the equation (12) in the synchronously rotating reference frame q^e - d^e ,

$$\left(i_{cd}^e \cos \omega_e t - i_{cq}^e \sin \omega_e t \right) = C \frac{d}{dt} \left(v_{ds}^e \cos \omega_e t - v_{qs}^e \sin \omega_e t \right)$$

$$\left. \begin{aligned} i_{cd}^e &= C (p v_{ds}^e - \omega_e v_{qs}^e) \\ i_{cq}^e &= C (p v_{qs}^e + \omega_e v_{ds}^e) \end{aligned} \right\} \quad (13)$$

The equations (1) to (13) describe the mathematical model of the modified self-commutated CSI fed induction motor drive.

V. STEADY STATE ANALYSIS

The steady state performance of the drive is obtained using the mathematical model of the drive. The various steady state equations used in the performance analysis are given below:

$$V_{r(0)} = V_{inv(0)} + r_f I_{dc(0)} \quad (14)$$

$$V_{inv(0)} = \frac{3}{2} k v_{qs(0)}^e \quad (15)$$

$$V_{r(0)} = 1.5 k v_{qs(0)}^e + r_f I_{dc(0)} \quad (16)$$

The steady state inverter current, machine current and capacitor current are related according to the following equations in q^e-d^e reference frame.

$$i_{invd(0)}^e = i_{dc(0)}^e + i_{ds(0)}^e \quad (17)$$

$$i_{invq(0)}^e = i_{qc(0)}^e + i_{qs(0)}^e \quad (18)$$

Since inverter output fundamental current peak is taken along the q^e -axis of the reference frame, therefore,

$$i_{invd(0)}^e = 0 \quad (19)$$

$$i_{invq(0)}^e = k I_{dc(0)} \quad (20)$$

Capacitor current is expressed in q^e-d^e reference frame as given below:

$$i_{dc(0)}^e = -C \omega_e v_{qs(0)}^e \quad (21)$$

$$i_{qc(0)}^e = C \omega_e v_{ds(0)}^e \quad (22)$$

The steady state stator current equations in q^e-d^e reference frame are given by the following expressions.

$$i_{ds(0)}^e = C \omega_e v_{qs(0)}^e \quad (23)$$

$$i_{qs(0)}^e = k I_{dc} - C \omega_e v_{ds(0)}^e \quad (24)$$

The steady state equation of the machine in q^e-d^e reference frame is as given below:

$$\begin{bmatrix} v_{qs(0)}^e \\ v_{ds(0)}^e \\ 0 \\ 0 \end{bmatrix} = \begin{bmatrix} r_s & \omega_e l_{ss} & 0 & \omega_e l_m \\ -\omega_e l_{ss} & r_s & -\omega_e l_m & 0 \\ 0 & \omega_{sl} l_m & r_r & \omega_{sl} l_{tr} \\ -\omega_{sl} l_m & 0 & -\omega_{sl} l_{tr} & r_r \end{bmatrix} \begin{bmatrix} i_{qs(0)}^e \\ i_{ds(0)}^e \\ i_{qr(0)}^e \\ i_{dr(0)}^e \end{bmatrix} \quad (25)$$

Under steady state condition, torque developed by the motor is equal to the load torque. Hence,

$$t_e = \frac{3}{2} \cdot \frac{P}{2} \cdot l_m \left(i_{qs(0)}^e i_{dr(0)}^e \right) = t_l \quad (26)$$

Solving these equations, we can obtain the expressions for performance parameters of the drive.

VI. SELECTION OF OPTIMAL CAPACITOR

To obtain the optimal value of capacitor required at the motor terminals for near sinusoidal current over a wide range of operating frequency, the steady state performance curves are plotted. These performance curves are obtained by computing the value of torque developed by the motor, power output, stator voltage per phase, stator current, power factor, power loss efficiency, dc link voltage for fixed value of dc link current, rated frequency and variable capacitance per phase and varying the slip from 0 to 1.

At the operating frequency and $C=90\mu\text{F}/\text{phase}$, slip-torque characteristic of Fig.6 shows that the torque developed by the machine is affected by the resonance. Therefore, higher value of capacitor is required. The performance curves are obtained for three different values of capacitor and are plotted against load torque as shown in Fig.6 to Fig.11. To explain these performance curves, the magnetization and rotor current variations with torque are also shown in Fig.12.

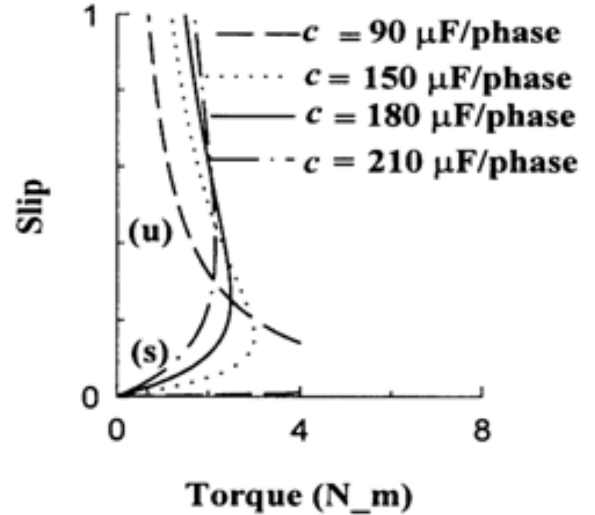


Fig.6: Variation of slip with load torque

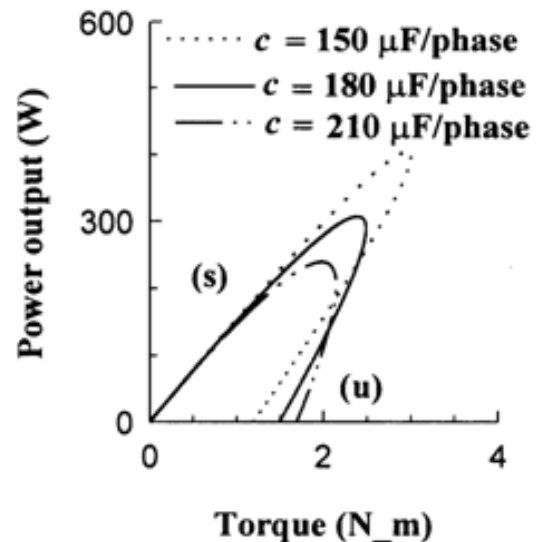


Fig.7: Variation of power output with load torque

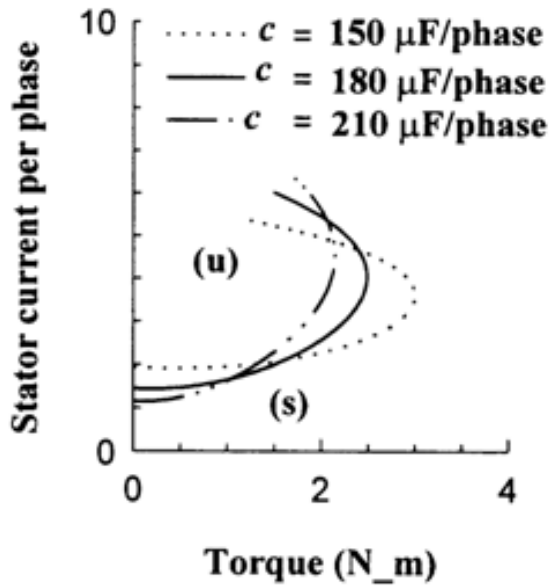


Fig.8: Variation of motor current with load torque

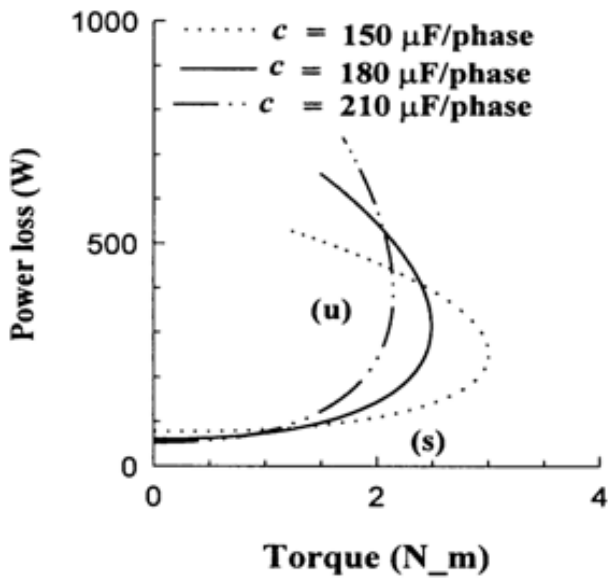


Fig.9: Variation of power loss with load torque

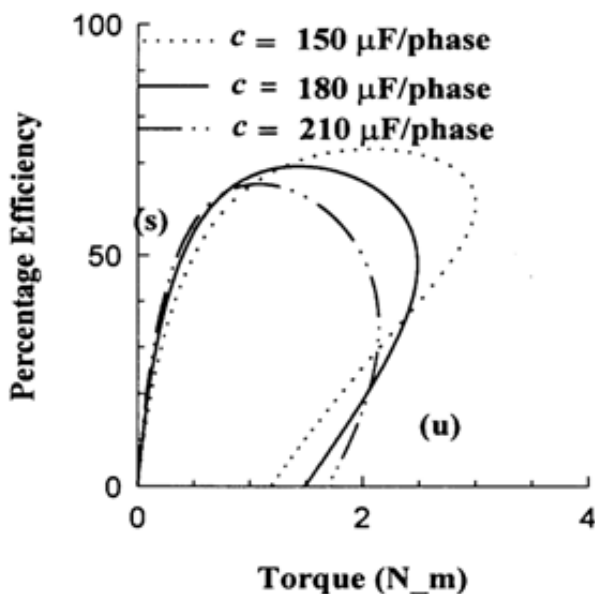


Fig.10: Variation of Efficiency with load torque

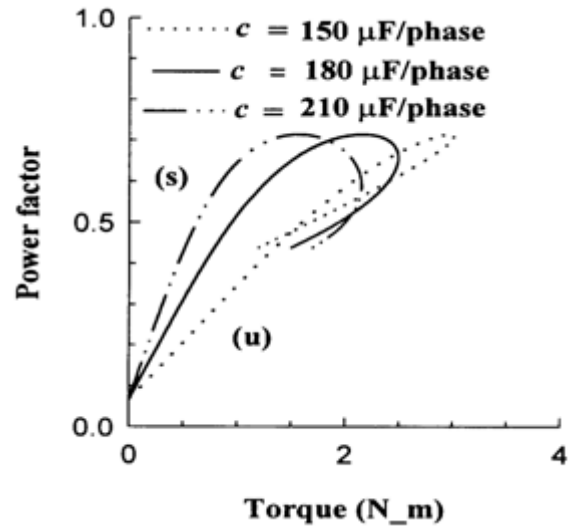


Fig.11: Variation of power factor with load torque

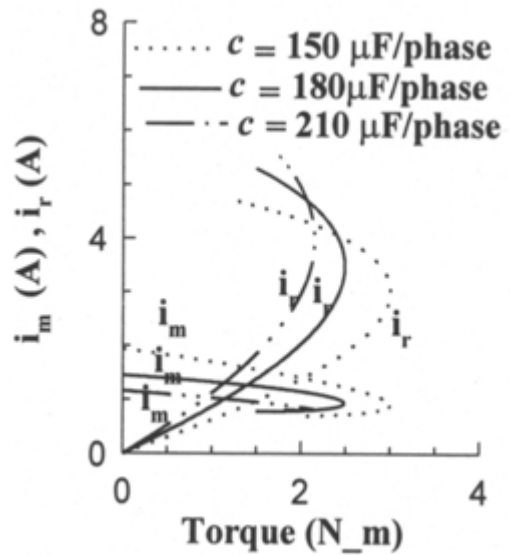


Fig.12: Variation of magnetizing and rotor current with load torque

Each curve is characterized by two regions, a stable region and an unstable region. In stable region as the capacitance increases, the slip increases for any value of torque. The peak value of torque decreases with the increase in capacitance while the slip corresponding to peak value of torque increases with the increase in capacitance. The starting torque is high at higher value of capacitance. Power output decreases with decrease in torque, in unstable region at each value of capacitance, because of low torque and high value of slip. The maximum value of power output reduces with the increase in capacitance. The stator current is the phasor sum of the magnetization and the rotor currents. As evident from the Fig.12, the magnetization current is nearly constant with respect to torque while the rotor current varies widely with torque. In the stable region at low value of slip, magnetization current is large in comparison to the rotor current, therefore stator current varies according to the variation in magnetization current. However, at high value of slip, rotor current is large in comparison to the magnetization current; therefore stator

current varies according to the variation of the rotor current. In the unstable region stator current increases with the decrease in torque corresponding to each value of capacitance because of high value of rotor current. The performance characteristics show that at a capacitor value of $150\mu\text{F}$, the performance of the drive is better.

The experimental investigations are also carried out in open loop with the different values of capacitance across motor terminals, and it is found that the performance of the drive is found to be the best at this value of capacitor. Hence, $150\mu\text{F}$ value of capacitor is selected. The motor currents are recorded for different operating frequencies and are found to be close to sinusoidal. These currents are shown in fig.13 to fig.15.

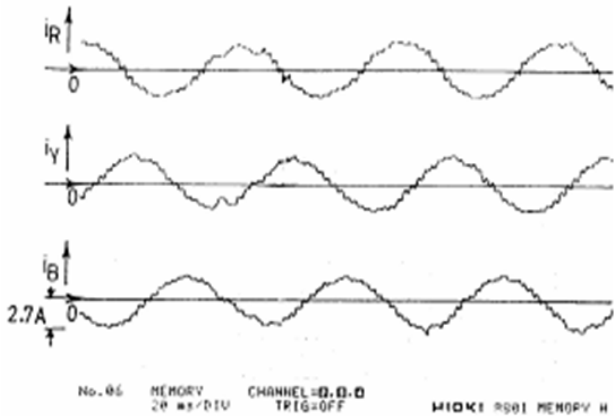


Fig.13: Motor line currents at 10 Hz operating frequency

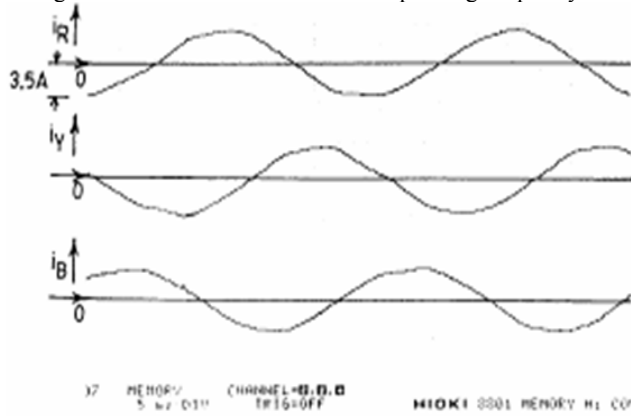


Fig.14: Motor line currents at 25 Hz operating frequency

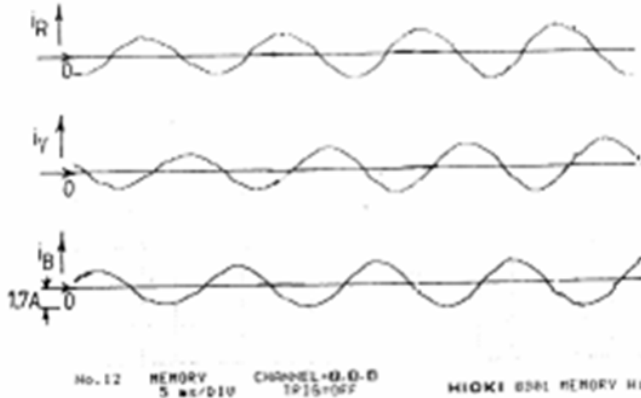


Fig.15: Motor line currents at 50 Hz operating frequency

VII. RESULTS AND DISCUSSIONS

To investigate the performance of the drive, the machine is run at the rated frequency of 314rad/sec and current of 3.0 Amp and load test is performed. The drive performance parameters such as slip, power output, stator voltage, stator current, efficiency, output power factor, dc link voltage, input power factor are determined and plotted against developed torque.

To confirm the validity of the mathematical model of the drive, the performance of the drive is computed at the same operating conditions and plotted on the same graph. The experimental and analytical performance curves are shown in Fig.16 to Fig.23. The curves are in close conformity to each other.

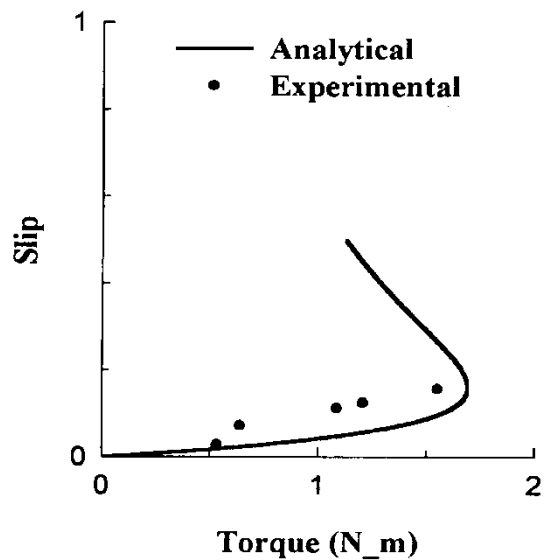


Fig.16: Slip vs torque characteristic

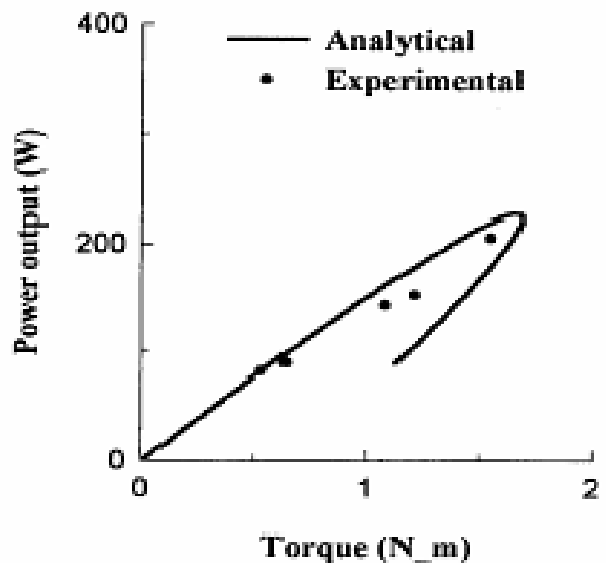


Fig.17: Power output vs torque characteristic

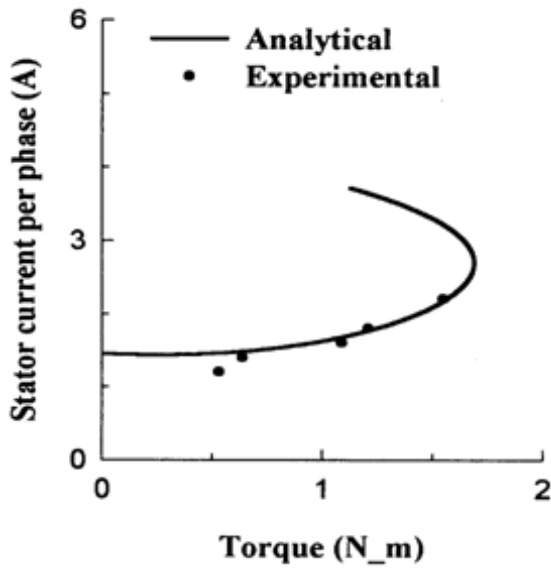


Fig. 18: Stator current vs torque characteristic

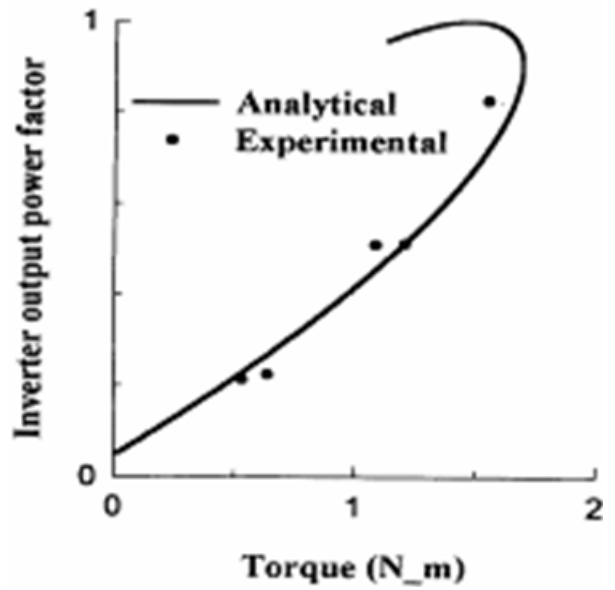


Fig. 21: Inverter output power factor vs torque characteristic

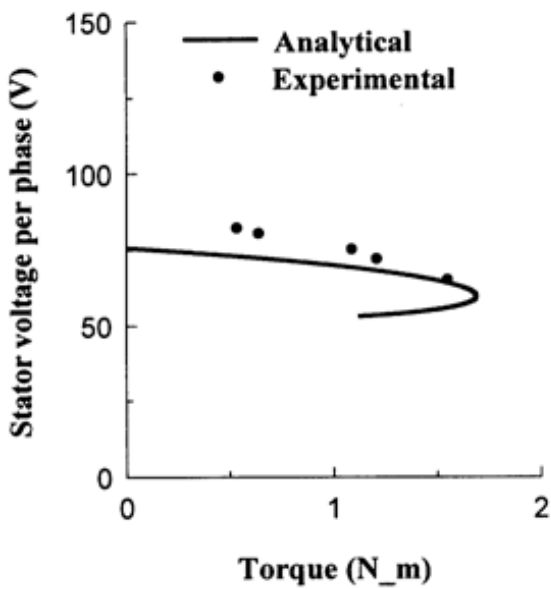


Fig.19: Stator voltage vs torque character

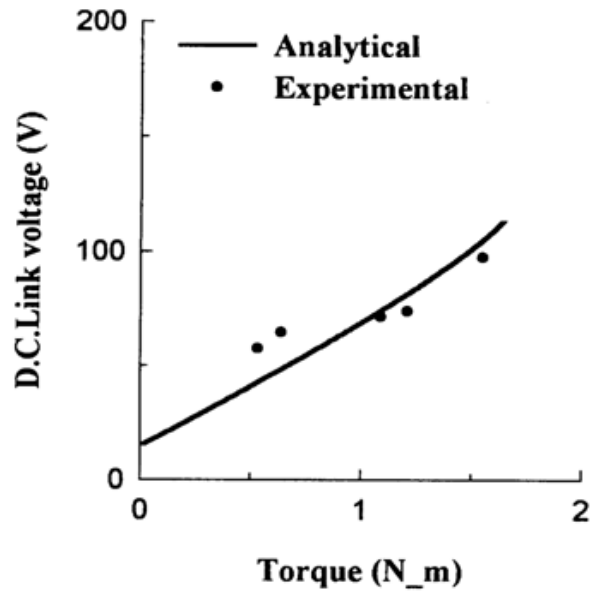


Fig.22: DC link voltage vs torque characteristic

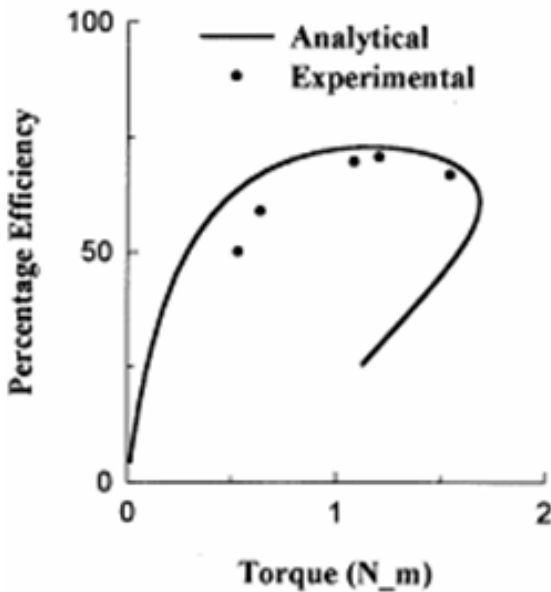


Fig.20: Efficiency vs torque characteristic

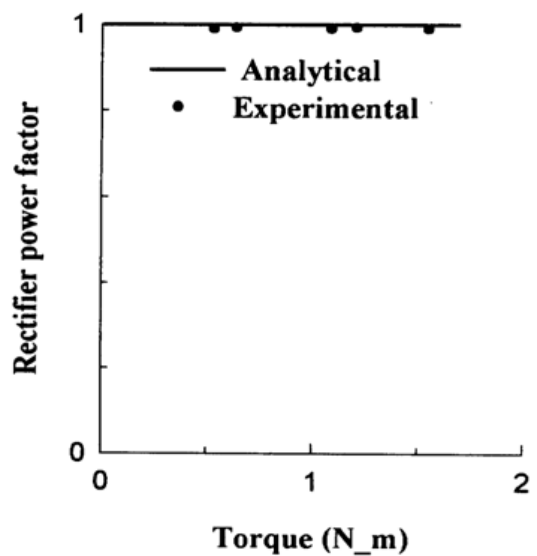


Fig.23: Input power factor vs torque characteristic

Slight deviation in the two curves is because of assumptions taken in the determination of analytical curves. For the same value of torque, slip obtained experimentally is more in comparison to the slip obtained analytically, since due to various power losses motor is not able to generate the same amount of torque at any speed as determined analytically. Therefore, the experimental power output at any value of torque is less in comparison to the power output obtained analytically. The power output increases with the increase in torque in both the cases. The stator current in both the cases are almost identical and very near to each other. The stator current variation with respect to torque is very small because with capacitance at the machine terminals. The magnetization and rotor currents are adjusted in such a manner that their phasor sum i.e. stator current varies very slowly with the torque. The efficiency increases with the increase in torque till maximum efficiency is achieved. At any value of torque experimentally obtained efficiency is less than the analytically obtained efficiency because of negligence of core, friction and windage losses. The power factor of the machine increases with the torque. Hence power factor of the inverter also increases with the increase in torque. For fixed value of dc link current the dc link voltage depends upon the input power demand of the machine. As the torque increases the power demand of the drive increases; hence dc link voltage increases with the torque. Both the power factors are quite close to each other at each value of operating frequency and torque. The analytically obtained power factor of pulse width modulated rectifier is always unity, while the experimentally obtained power factor is found to be very close to unity.

Thus, a good co-relation is found between analytical and experimental performance curves. The agreement between the analytical and experimental performance curves confirms the validity of the developed model considering various assumptions.

VIII. CONCLUSION

A modified self-commutating CSI-fed induction motor drive is presented. The steady state performance expressions are developed. The steady state performance of the drive is drawn at the different value of capacitances to select the capacitor required at the machine terminals. The optimal value of capacitor is selected from the curves for high power output, acceptable current, minimum power loss and maximum efficiency. The steady state performance curves at the optimum value of capacitance are drawn through simulation and are compared with the experimental curves drawn at the rated operating frequency and fixed dc link current in the open loop.

APPENDIX

Induction Motor Parameters

3-phase, 400V, 50 Hz, star connected, 1.0 H.P.

$r_s = 3.52 \Omega$, $r_r = 2.78 \Omega$, $l_{ss} = 0.165 \text{ H}$

$l_{tr} = 0.165 \text{ H}$, $l_m = 0.15 \text{ H}$, $J = 0.01289 \text{ kg-m}^2$

D.C. Link Parameters

$r_f = 0.250 \Omega$, $L_f = 0.04 \text{ H}$

REFERENCES

- [1] S. Nonka and Y. Neba, "New GTO current source inverter with pulse width modulation control techniques", IEEE Transactions on Industry Applications, Vol. IA-22, No. 4, July/Aug 1986, pp. 666-672.
- [2] S.R. Bowes and R.I. Bullough, "Optimal PWM microprocessor controlled current-source inverter drives", IEEE proceedings, Vol. 135, Pt. B, No. 2, March 1988, pp. 59-75.
- [3] P.N. Enjeti, P.D. Ziogas and J.F. Lindsay, "Programmed PWM technique to eliminate harmonics: A critical evaluation", IEEE Transactions on Industry Applications, Vol. 26, No. 2, March/April 1990, pp. 302-315.
- [4] N.R. Zargari, Y. Xiao and Bin Wu, "Near unity input displacement factor for current source PWM drives", IEEE Industry Applications Magazine, July/Aug. 1999 pp. 19-25.
- [5] S.R. Bowes and S. Grewal, "Novel harmonic elimination PWM control strategies for three phase PWM inverters using space vectors techniques", IEEE Proceedings Electric Power Applications, Vol. 146, Sept. 1999, pp. 495-514.
- [6] J.R. Espinoza and G. Joss, "A current-source inverter-fed induction motor drive system with reduced losses", IEEE Transactions on Industrial Applications, Vol.34, No. 4, pp. 796-805.
- [7] N. Sawaki and N.Sato, "Steady-state and stability analysis of induction motor driven by current source inverter", IEEE Transactions on Industry Applications, Vol. IA-13, No. 3, May/June 1977pp. 244-251.
- [8] E.P. Cornell, and T.A. Lipo, "Modeling and design of controlled current induction motor drive system", IEEE Transactions on Industry Applications, Vol. 13, July/Aug. 1977,pp. 321-329.
- [9] A. Joshi and S.B. Dewan, "Modified steady-state analysis of the current-source inverter and squirrel cage motor drive", IEEE Transactions on Industry Applications, Vol. IA-17, No. 1, Jan/Feb 1981, pp. 50-57.
- [10] P. Agarwal and V.K. Verma, "Performance evaluation of current source inverter- fed induction motor drive", Journals of Institution of Engineers, Vol.72, February 1992, pp. 209-217.
- [11] S. Kwak and H.A. Toliyat, "A hybrid solution for load commutated inverter fed induction motor drive", IEEE Transactions on Power Electronics, Vol.41, No.1, Jan/Feb 2005, pp.83-90.
- [12] Abdul Rahiman Beig and V.T. Ranganathan, "A novel current source inverter fed induction motor drive", IEEE Transactions on Power Electronics, Vol.21, No.4, July 2006, pp-1073-1082.

BIOGRAPHIES



Pramod Agarwal (M'99) received the B.E., M.E., and Ph.D degrees in Electrical Engineering from the University of Roorkee, India, in 1983, 1985 and 1995, respectively.

He joined the erstwhile University of Roorkee, India in 1985 as Lecturer. He was a Postdoctoral Fellow with the Ecole de technologie superior, University of Quebec, Montreal, Canada. He is currently a Professor with the Department of Electrical Engineering, Indian Institute of Technology, Roorkee, India. He has developed a number of educational units for laboratory

experimentation. His fields of specialization are electrical machines, power electronics, microprocessor and microcomputer controlled ac/dc drives, active power filters, multi-level inverters and high power factor converters.



Ashok Kumar Pandey born in 1964, did B.E. (Electrical) from M. M. M. Engineering College, Gorakhpur, India in 1987, M.Tech. (Power Electronics, Electrical Machines and Drives) from Indian Institute of Technology, Delhi in 1995 and Ph.D. from Indian Institute of Technology, Roorkee in 2003.

He joined the Electrical Engineering Department, M. M. M. Engineering College, Gorakhpur, India in 1987 and is presently working as an Assistant Professor. His area of interest includes Power Electronics, Electrical Machines and Drive



V.K. Verma did B.E. (Electrical Engineering) from Government Engineering College, Jabalpur in 1962 and M.E. and Ph.D. from University of Roorkee, Roorkee, India in 1965 and 1976 respectively. He joined Electrical Engineering Department at University of Roorkee, India in 1969 as Reader and became Professor in 1978.

He retired in the year 2000 from University of Roorkee and is currently a Professor with the Department of Electrical Engineering, College of Engineering, Roorkee, India. His

field of research work is Power Apparatus and Electric Drives and microprocessor applications

Reliability Estimation for Power Factor Correction Circuits

Kumar A. Praveen¹ Amer Gulam² Rao.S Srinivasa³

Abstract-Reliability plays an important role in power electronic systems such as spacecrafts, aircrafts and telecommunications. Therefore it is necessary to calculate the failure rate, repair cost etc before designing a power supply for such applications. In this paper single switch boost Power Factor Correction (PFC) converter and interleaved boost PFC converter is simulated in Discontinuous Conduction Mode (DCM), Critical Conduction Mode (CRM) and Continuous Conduction Mode (CCM) under different output power ratings and results are tabulated. The reliability of semiconductor devices and all other components of the converter are calculated based on MIL-HDBK-217 standard. From the simulation results it is found that both single switch boost PFC converter and interleaved boost PFC converter performance when operating in CCM is better with reference to reliability.

Keywords - Reliability, Power factor correction, Boost Converter, Simulation of converters.

I. INTRODUCTION

Reliability is the probability of operating a product for a given period of time without failure under specified conditions and within specified performance limits. It plays an important role in power electronic systems by which the number of system failures, repair costs, guarantee etc are estimated. Every day the dependency upon the continuous availability of electronic equipment grows [1]. Examples include telephone systems, computers supporting stock markets, and industrial control equipment, petrochemicals etc. This means the power supplies supporting the equipments/loads must perform without interruption and without any fault. The design emphasis in power-electronic systems is primarily on (apart from production cost) efficiency, power density and quality; the assumption being, if these criteria are met then, once a power-electronic product or system is in service, it will last for a long time (i.e. it have a high mean time to failure or MTTF). This is not a rational expectation and as such, many of the power-supply and power-system industries are faced with the daunting reality of random product and system failures in the field at a steady rate, which is costing the industries a lot. Many power-supply/power-system industries have expressed the need for investigating failure modes of their products/systems to significantly increase the MTTF and the mean time between failures (MTBFs). However, this is not an easy task which requires an extensive multidisciplinary effort.

The paper first received 5-Jun-2009 and in revised form 16-Sept- 2009.
Digital Ref: A17050229

¹ Department of Electrical Engineering, National Institute of Technology

² Department of Electrical Engineering, National Institute of Technology Warangal, Andhra Pradesh, India E-mail: amer.nitw@gmail.com

³ Department of Electrical Engineering, National Institute of Technology Warangal, Andhra Pradesh, E-mail: srinivasarao_nitw@yahoo.co.in

A. Reliability Function

The reliability of a component can be described as an exponential function [1]. The probability of finding a component operating after a time period is defined as:

$$R(t) = e^{-\lambda t} \quad (1)$$

Where λ is the constant failure rate during the useful life period. The mathematic mean value of $R(t)$ occurs at t equal to $1/\lambda$. It is the mean time elapsed until a failure which occurs, or the "Mean Time To Failure", MTTF. Reliability curve is shown in Fig. 1.

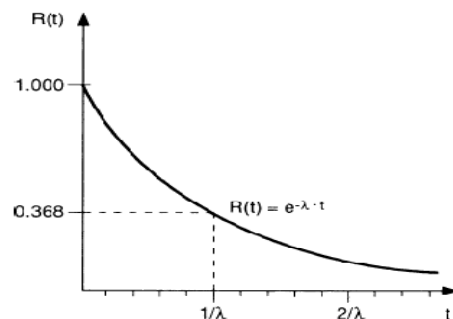


Fig.1 Reliability curve [1]

MTBF (Mean Time between Failures): As repair time (MTTR) normally can be neglected compared to MTTF for electronics, MTBF can be found as :

$$\begin{aligned} \text{MTBF} &= \text{MTTF} + \text{MTTR} \\ &\approx \text{MTTF} = 1/\lambda \end{aligned}$$

MTBF or the failure rate can be calculated using different kinds of input data.

B. Time Dependence of Failure Rate

The time dependence of the failure rate for a given population of items of the same type often exhibits at least one of the following three periods which produce a bathtub curve as in Fig. 2.

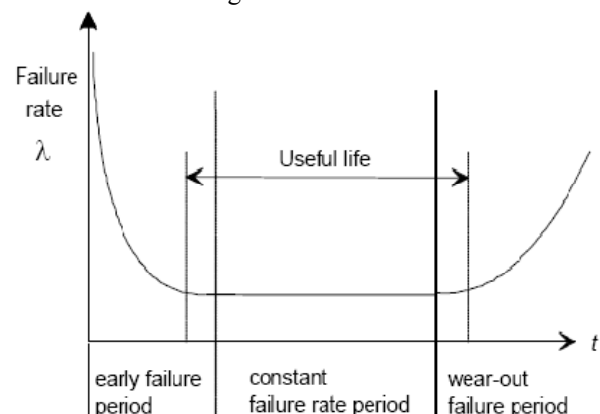


Fig. 2 Time dependence of the failure rate

When interpreting reliability figures it is important to determine the physical reality of failure modes and distributions. These three periods can be explained as in the following. However, the time dependence curve for any single item type could be significantly different.

1. *Early failure period*: At the start of the operating period, sometimes a higher failure rate is observed which decreases with time. Early failures occur due to manufacturing processes and material weaknesses that do not result in failures in tests.
2. *Constant failure rate period*: After the early failure period, the failures occur with varying failure causes that result in an effective constant failure rate during the useful life.
3. *Wear-out failure period*: The final period that shows an increasing rate of failures due to the dominating effects of wear-out, ageing or fatigue.

C. Calculation of MTBF for Equipment

When calculating the MTBF for equipment [1], its total failure rate λ_e must be found. Normally the assumption is that all components are needed for operation. Consider an equipment or apparatus containing n components. The probability to find n components in operation after the time t is:

$$R = R_1 \cdot R_2 \cdot \dots \cdot R_n = e^{-\lambda_1 t} \cdot e^{-\lambda_2 t} \cdot \dots \cdot e^{-\lambda_n t} = e^{-(\lambda_1 + \lambda_2 + \dots + \lambda_n)t} = e^{-\lambda_e t} \quad (2)$$

and

$$\lambda = \lambda_1 + \lambda_2 + \lambda_3 + \dots + \lambda_n \quad (3)$$

The total failure rate for the equipment at specified conditions is accordingly achieved as:

$$\lambda_e = \lambda_{b1} \cdot c_1 + \lambda_{b2} \cdot c_2 + \dots + \lambda_{bn} \cdot c_n \quad (4)$$

By simply inverting this value, the MTBF figure for the equipment is found:

$$MTBF = \frac{1}{\lambda_e} \quad (5)$$

D. Reliability Prediction [2]

Reliability predictions are conducted during the concept and definition phase, the design and development phase and the operation and maintenance phase, at various system levels and degrees of detail, in order to evaluate, determine and improve the dependability measures of an item. Successful reliability prediction generally requires developing a reliability model of the system considering its structure. The level of detail of the model will depend on the level of design detail available at the time. Several prediction methods are available depending on the problem. During the conceptual and early design phase a failure rate prediction is a method that is applicable mostly, to estimate equipment and system failure rate. Following models for predicting the failure rate of items are given:

- failure rate prediction at reference conditions (parts count method)
- failure rate prediction at operating conditions (parts stress method)

Failure rate predictions are useful for several important activities in the design phase of electronic equipment in

addition to many other important procedures to ensure reliability. Examples of these activities are:

- to assess whether reliability goals can be reached,
- to identify potential design weaknesses,
- to compare alternative designs,
- to evaluate designs and to analyze life-cycle costs,
- to provide data for system reliability and availability analysis,
- to plan logistic support strategies,
- to establish objectives for reliability tests.

E. Parts Count Method

In this paper, parts count method is used. The failure rate for equipment under reference conditions is calculated as follows:

$$\lambda_{s,t} = \sum_{i=1}^n (\lambda_{ref})_i \quad (6)$$

where

λ_{ref} is the failure rate under reference conditions
 n is the number of components

The reference conditions adopted are typical for the majority of applications of components in equipment. Reference conditions include statements about operating phase, failure criterion, operation mode (e.g. continuous, intermittent), climatic, mechanical stresses and electrical stresses. It is assumed that the failure rate used under reference conditions is specific to the component, i.e. it includes the effects of complexity, technology of the casing, different manufacturers and the manufacturing process.

F. Parts Stress Method

Components in equipment may not always operate under the reference conditions. In such cases, the real operational conditions will result in failure rates different from those given for reference conditions. Therefore, models for stress factors, by which failure rates under reference conditions can be converted to values applying for operating conditions (actual ambient temperature and actual electrical stress on the components), and vice versa, may be required. The failure rate for equipment under operating conditions is calculated as follows:

$$\lambda = \sum_{i=1}^n (\lambda_{ref} \times \pi_U \times \pi_I \times \pi_T)_i \quad (7)$$

where

λ_{ref} is the failure rate under reference conditions;
 π_U is the voltage dependence factor;
 π_I is the current dependence factor;
 π_T is the temperature dependence factor;
 n is the number of components

II. SINGLE SWITCH BOOST PFC RECTIFIER

The operation of boost PFC converter can be studied under three modes of operations viz. continuous conduction mode, discontinuous conduction mode and critical conduction mode. The continuous conduction mode is studied and simulated for three current control modes-

peak current mode control, average current mode control and hysteresis current mode control. Fig. 3 shows the schematic diagram of boost PFC converter.

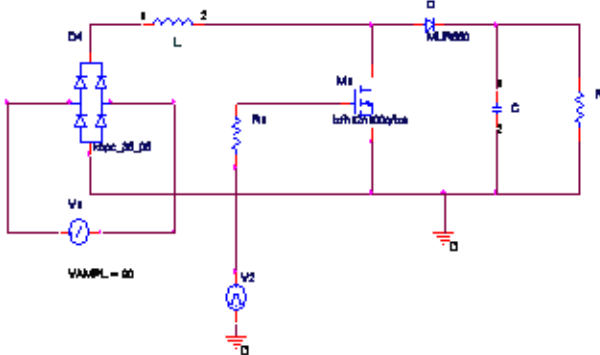


Fig. 3 Boost PFC rectifier

A. Continuous Conduction Mode of Operation

The operation of boost PFC converter for Continuous conduction mode is studied and simulated under voltage control mode and current control mode. The current control mode is simulated under three modes namely peak current mode control, average current mode control and hysteresis current control mode. By calculating the reliability under these three current control modes we can understand which method is best from the reliability point of view and also we can verify whether any of the three current control modes is inferior in reliability to DCM and CRM modes.

(a) Peak Current Mode Control:

The current control signal i^* which is a scaled input voltage determines the peak of the inductor current i_L , the sinusoidal current reference. This reference is usually obtained by multiplying a scaled replica of the rectified line voltage v_g times the output of the voltage error amplifier, which sets the current reference amplitude. The active switch in the boost converter is turned on at the beginning of each switching cycle. The switch is turned on at constant frequency by a clock signal. As soon as the inductor current i_L reaches i^* , the switch is turned off and this process repeats [3]. In this way, the reference signal is naturally synchronized and always proportional to the line voltage, which is the condition to obtain unity power factor.

(b) Average Current Mode Control:

The inductor current is sensed and filtered by a current error amplifier whose output drives a PWM modulator. In this way the inner current loop tends to minimize the error between the average input current i_g and its reference. The latter is obtained in the same way as in the peak current control. Its advantage over the peak current mode control is that the stability ramp, which is mandatory for the peak current mode control, is eliminated. The inductor current waveform shown in fig 4.

(c) Hysteresis Current Mode Control:

The upper inductor current reference is a half sinusoidal denoted $I_p \sin \omega t$, with peak amplitude of I_p . The lower current reference is a half sinusoid, denoted $I_c \sin \omega t$, with peak amplitude of I_c . The average inductor current, which has only the 120 Hz component of inductor current, is a half sinusoid, denoted $I_m \sin \omega t$. The inductor current ripple is $\delta \sin \omega t$, where δ is the peak current ripple. Since the

inductor current switches at a much higher rate than the line voltage, the line voltage is assumed constant in each inductor current switching cycle [4] for the above current control mode techniques.

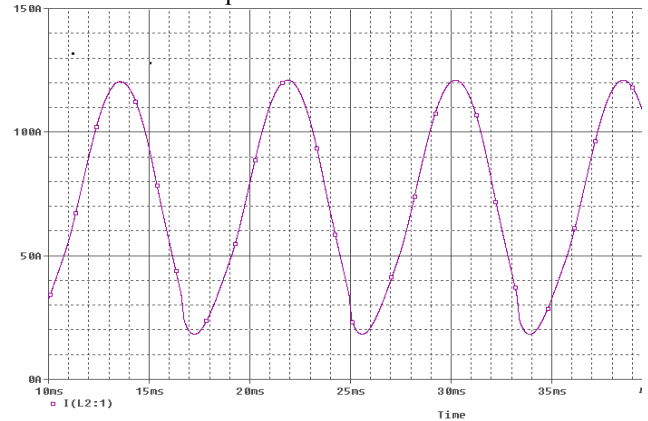


Fig. 4 Inductor current waveform for CCM- Average CMC

B. Discontinuous Mode of Operation

For low power application, to reduce the added component count and cost of the PFC stage in the two-stage approach, low cost alternatives have been rigorously pursued by attempting to integrate the active PFC input stage with the isolated DC/DC converter. The input PFC function is automatically achieved based on the principle of circuit operation. Generally, the input power factor of discontinuous PFC converter is not unity, but its input current harmonics are small enough to meet the specifications, such as the IEC 61000-3-2 class D [5]. The discontinuous conduction mode of boost PFC is simulated and the inductor current waveforms are shown in Fig.5 and Fig. 6.

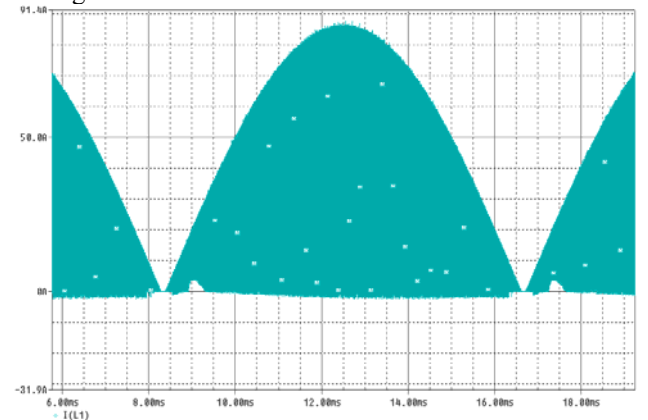


Fig. 5 Inductor current waveform for DCM

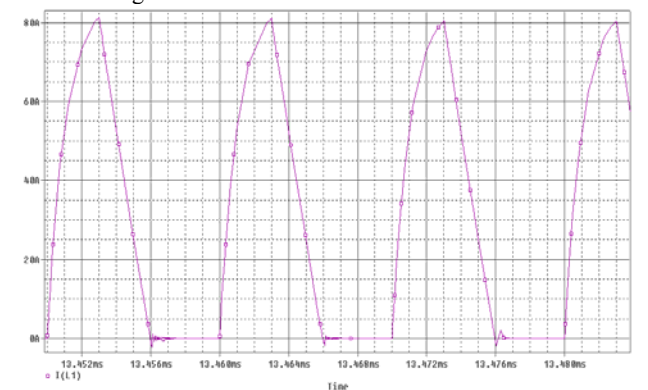


Fig.6 Inductor current for DCM (enlarged)

C. Critical Boost PFC Rectifier

The operation at the boundary of CCM and DCM was considered "constant on-time" for the boost switch. However, due to finite switching frequency and capacitor filter effect, the switch turn-on time varies throughout the entire cycle. This variation of the switch "on-time" affects the average switching frequency and the circuit component selection criterion. The control switch turns on when the inductor drops to zero and turns off when the inductor current reaches the peak inductor current envelope. The actual inductor current presents a saw tooth-type wave shape [6]. The simulated waveforms under critical conduction mode are shown in Fig. 7 and Fig. 8.

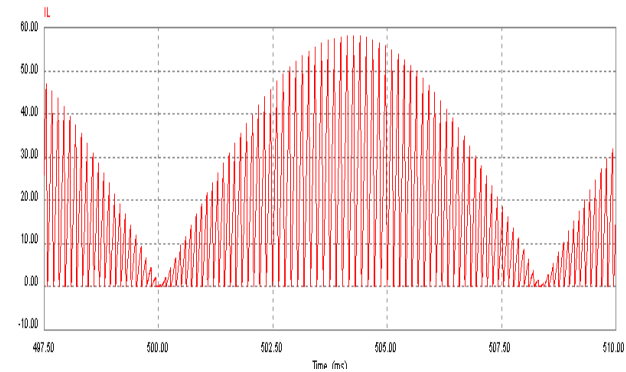


Fig.7 Inductor current waveform for CRM

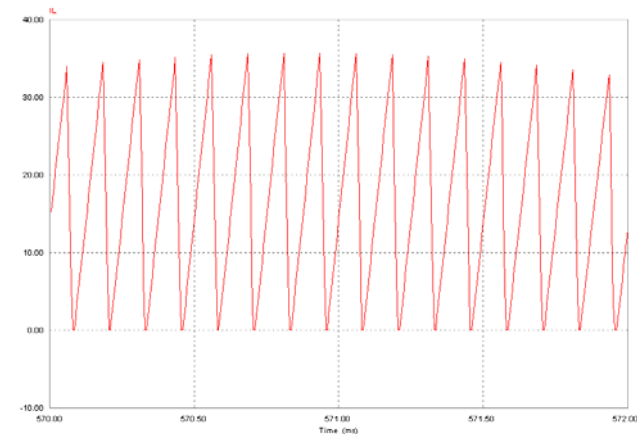


Fig.8 Inductor current waveform for CRM (enlarged)

III. INTERLEAVED BOOST PFC

Interleaved converters offer several advantages over single-power stage converters; a lower current ripple on the input and output capacitors, faster transient response to load changes and improved power handling capabilities at greater than 90% power efficiency. Another important advantage of interleaving is that it effectively increases the switching frequency without increasing the switching losses. The obvious benefit is an increase in the power density without the penalty of reduced power-conversion efficiency. There is still a penalty, however. Interleaving requires increased circuit complexity (greater number of power-handling components and more auxiliary circuitry), leading to higher parts and assembly cost and reduced reliability. Fig.9 shows the schematic diagram of interleaved Boost PFC [7-8].

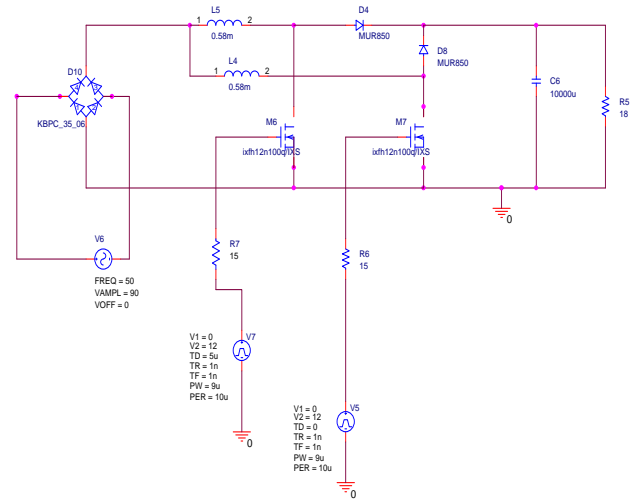


Fig. 9 Interleaved Boost Converter Topology

A. Continuous Conduction Mode

Even though the inductor currents in I_{L1} and I_{L2} are discontinuous the input current which is the sum of two inductor currents is continuous [9]. So that interleaving virtually eliminates discontinuity in the input current which is a major advantage. The inductor current waveform for continuous conduction mode of interleaved converter is shown in Fig. 10

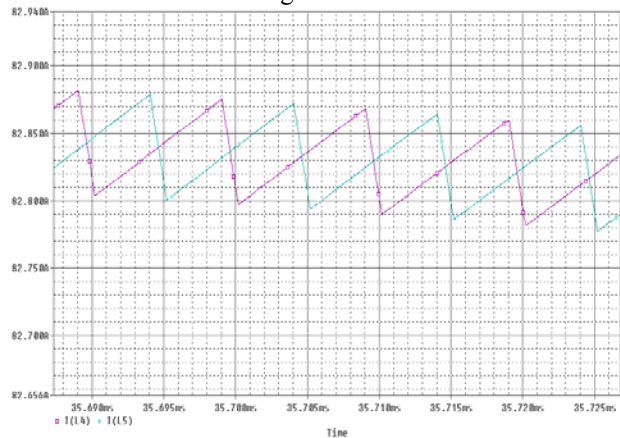


Fig. 10 Inductor current waveforms for Interleaved CCM (enlarged)

B. Discontinuous Mode of operation

To operate interleaving configuration in discontinuous mode of operation the phase shift of 180° is properly incorporated between the two inductor currents by using the delay. Fig. 11 shows the boost inductor current waveforms in discontinuous mode of operation.

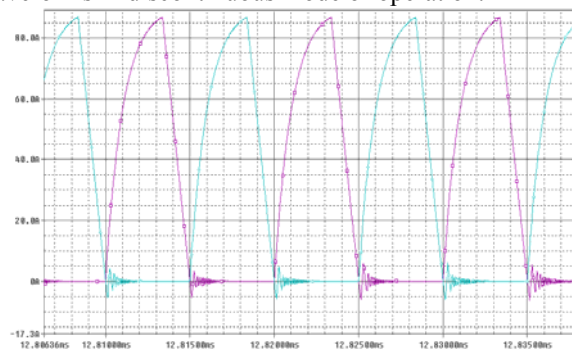


Fig. 11 Inductor currents waveforms (enlarged) for interleaved DCM boost

C. Critical Conduction Mode

The interleaved switching converter composed of parallel connection of switching converters of the same switching frequency, but each switching phase is sequentially shifted over equal fractions of the switching period [10]. The simulated CRM inductor current waveforms have been shown in Fig.12.

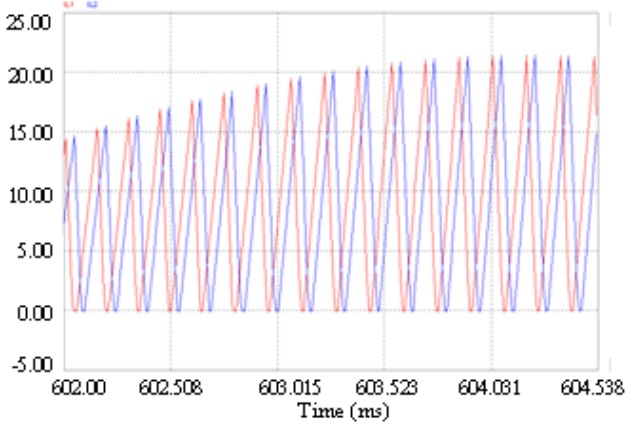


Fig. 12 Inductor currents for Interleaved CRM (enlarged)

IV. RELIABILITY CALCULATIONS [11]

In this section, reliability of the boost converter in 1200 W output power and Peak Current Mode control is calculated and presented in details. For different output powers and operating modes, results of reliability calculations are shown in Table-IV to Table-VI. The parts count method is used to calculate reliability. In this approach, first the failure rate of each component in the converter configuration is obtained individually and then the value of the converter’s MTBF is calculated from equations (4) and (5) that “N” is the number of consisting parts. The reliability of semiconductor devices and all other components of the converter are calculated based on MIL-HDBK-217 standard [12]. MIL-HDBK-217 provides failure rate data and stress models for parts count and parts stress predictions. It provides models for many component and assembly types and fourteen environments ranging from ground benign to canon launch. It is well known for international military and commercial design procedures has been widely accepted. It provides predictions for ambient of 0°C to 125°C. For these calculations the following assumptions are made:

1. The ambient temperature is 27 °C
2. The control structures of these converters are not the same whose reliability can be neglected for comparing the reliability of main components.
3. To calculate the reliability, first the dynamic and static losses of MOSFET and diode should be calculated for different output powers working in three operating modes namely CCM, DCM and CRM.

$$P_{dynamic} = V_{avg} \times I_{avg} \times t_{ol} \times f_s \tag{8}$$

$$P_{static} = V_{on} \times I_{avg} \times t_{on} \times f_s \tag{9}$$

$$P_{loss} = P_{static} + P_{switching} \tag{10}$$

It should be noted that if the converter is operating in DCM mode, ensure that before further turn-on of the switch, the inductor current reaches to zero. So that there will not be turn-on loss. But in CCM operating mode, since in turn-on instant for the switch, the current should

be transferred from diode to the switch, the dynamic loss includes both turn-on/turn-off losses. Sample simulated diagrams for MOSFET and diode switching wave forms have been shown in Fig. 12 – 16.

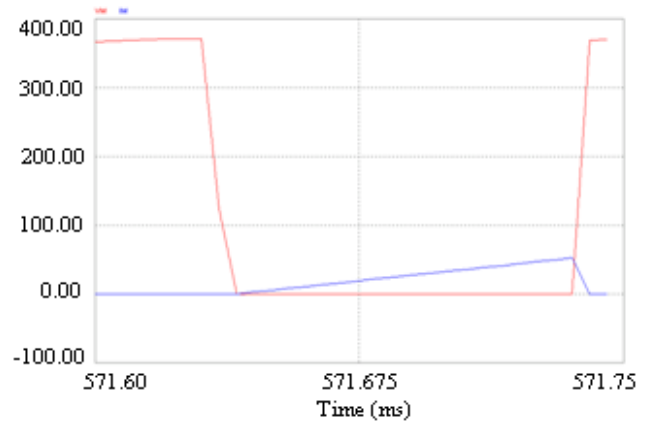


Fig. 13 MOSFET switching waveform for 1200W- CRM.

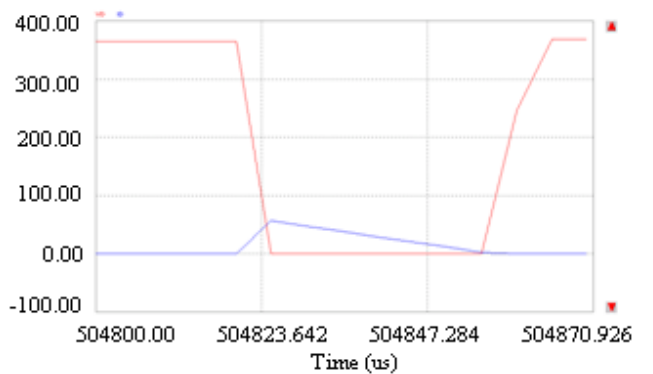


Fig. 14 Diode switching waveform for 1200W- CRM.

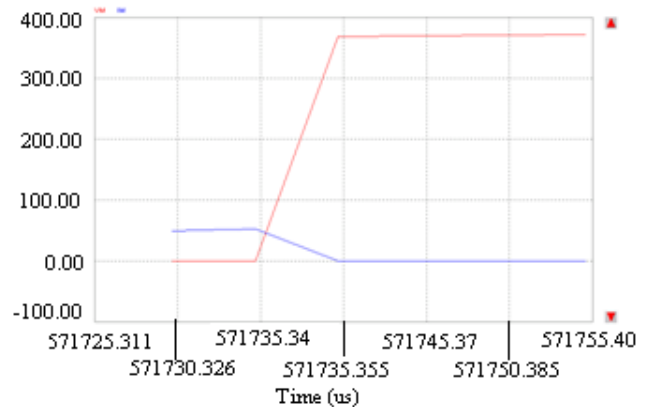


Fig. 15 Turn-off overlap of MOSFET waveform for 1200W- CRM

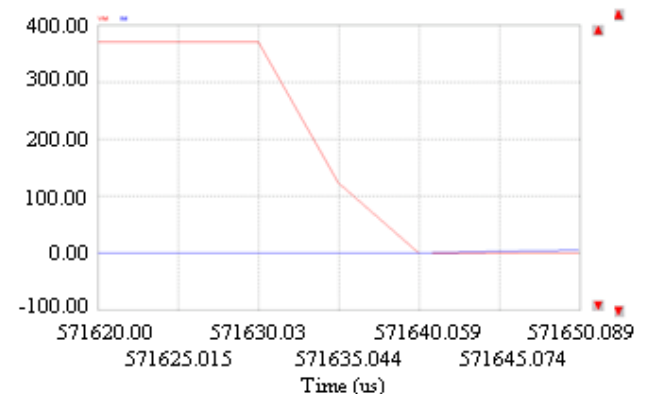


Fig. 16 Turn-on overlap of MOSFET waveform for 1200W- CRM

V. RESULTS AND CONCLUSIONS

A. Discussion of Result

The power loss is calculated for each component in the converters under specified operating modes and tabulated in Tables I, II and III. Then, the reliability is calculated and compared for CCM (namely Peak-CMC, Average-CMC and Hysteresis-CMC), DCM and CRM for the converters and tabulated in tables IV, V and VI.

B. Conclusions

From Table IV, V, VI the following points are observed.

- The Boost Converter has highest reliability in CCM operating mode than in DCM and CRM.
- Switches have highest failure rate in DCM and CRM modes than CCM mode. Since in DCM and CRM modes the peak and rms values of current are higher that results in higher current stress on switches in this mode. Therefore failure rate is higher in CRM and then DCM compared to CCM.
- The results concluded for single switch boost PFC are true for interleaving configuration also. But the reliability of interleaved topology is much lesser compared to the single switch boost PFC because of the presence of two inductors, two diodes and two MOSFETs.

Table-1: Calculated power loss for each component of the boost PFC rectifier

Output Power	800W			1000W			1200W		
	Peak	Average	Hysteresis	Peak	Average	Hysteresis	Peak	Average	Hysteresis
P _{dynamic} (MOSFET)	27.032292	49.614022	93.5101	28.7910	42.62004	73.416	33.787	40.68318	50.4336
P _{static} (MOSFET)	27.34746	43.9747	100.0123	27.81144	39.2316	78.46335	35.376875	43.3254	52.53623
P _{dynamic} (DIODE)	0.94956	1.2294	1.819272	1.270665	2.4239	3.889664	1.9836	1.9986	5.472
P _{static} (DIODE)	0.017835	0.0266568	0.051156	0.029445	0.030247	0.2752386	0.006961	0.00232	0.01152
Input Bridge	3.70128	3.7224	3.79104	3.84384	3.85176	3.86496	3.8808	3.91776	3.96

Table-II Calculated power loss for boost PFC under DCM and CRM

Output Power	800W		1000W		1200W	
	DCM	CRM	DCM	CRM	DCM	CRM
P _{dynamic} (MOSFET)	258.44364	251.4707	229.7106	235.36	135.6885	152.9867
P _{static} (MOSFET)	0.1027628	22.2179	0.094374	26.668	0.02777	23.8866
P _{dynamic} (DIODE)	41.90355	128.1775	30.9852	141.3348	19.1568	166.6692
P _{static} (DIODE)	0.005655	0.16228	0.038627	0.108703	0.0054375	0.30942
Input Bridge	4.32432	5.16912	4.752	5.3724	5.7024	6.115824

Table-III Calculated power losses for MOSFET, output diode and the input bridge for interleaved boost converter

Output Power	800W			1000W			1200W		
	CCM	DCM	CRM	CCM	DCM	CRM	CCM	DCM	CRM
$P_{dynamic}$ (MOSFET) Watts	71.4604	235.4625	238.05197	106.657	23.5172	318.1074	119.238	425.044125	451.6391
P_{static} (MOSFET) Watts	40.85928	0.1029	0.03659	19.36	5.4931	0.169814	17.768	0.25276	0.326604
$P_{dynamic}$ (Output Diode) Watts	2.2758	60.732	76.650435	11.4468	12.2972	52.02252	2.5245	52.24275	56.25371
P_{static} (Output Diode) Watts	0.036125	0.005156	0.0019575	0.162	0.0971	0.018125	0.03912	0.0098	0.04902
P_{loss} (Input Bridge) Watts	2.5476	4.32432	4.7256	2.75616	4.9896	5.2008	2.86704	5.89248	6.0984

Table-IV Reliability calculations for CCM operating mode for single switch boost PFC

Output Power	800W			1000W			1200W		
	Peak	Average	Hysterisis	Peak	Average	Hysterisis	Peak	Average	Hysterisis
λ_p (MOSFET)	15.38	29.64	88.85	16.04	24.81	60.52	20.12	25.66	33.85
λ_p (Output Diode)	0.363	0.412	0.453	0.065	0.073	0.087	0.041	0.05	0.06
λ_p (Input Bridge)	0.241	0.250	0.2656	0.143	0.155	0.164	0.104	0.110	0.113
λ_p (Input Inductor)	0.251	0.251	0.233	0.251	0.251	0.233	0.251	0.251	0.233
λ_p (Output Capacitor)	0.060	0.06	0.06	0.07	0.07	0.07	0.084	0.084	0.084
λ_p (Output Resistor)	0.03	0.03	0.03	0.03	0.03	0.03	0.03	0.03	0.03
Total λ_p	16.32	30.64	89.89	16.60	25.39	61.10	20.63	26.18	34.37
MTBF (hours)	61267	32631	11124	60234	39389	16365	4846	38194	29093

Table-V Reliability calculations for DCM and CRM operating modes of single switch boost PFC

Output Power	800W		1000W		1200W	
	DCM	CRM	DCM	CRM	DCM	CRM
λ_p (MOSFET)	141.25	154.56	117.04	144.28	50.86	76.96
λ_p (Output Diode)	3.90	20.12	0.66	9.72	0.075	4.10
λ_p (Input Bridge)	0.18	0.21	0.19	0.20	0.16	0.17
λ_p (Input Inductor)	0.18	0.18	0.18	0.18	0.18	0.18
λ_p (Output Capacitor)	0.06	0.06	0.07	0.07	0.084	0.084
λ_p (Output Resistor)	0.03	0.03	0.03	0.03	0.03	0.03
Total λ_p	145.60	175.17	118.16	154.48	51.391	81.54
MTBF (hours)	6868	5708	8463	6473	19458	12264

Table-VI Reliability calculations for CCM, DCM and CRM operating modes of interleaving boost PFC

Output Power	800W			1000W			1200W		
	CCM	DCM	CRM	CCM	DCM	CRM	CCM	DCM	CRM
λ_p (MOSFET)	76.686	256.9	261.11	90.92	390.41	391.16	103.20	601.56	655.33
λ_p (Output Diode)	0.200	2.030	3.145	0.58106	2.776	3.1293	0.60	5.014	5.86
λ_p (Input Bridge)	0.103	0.124	0.139	0.14213	0.169	0.181	0.173	0.209	0.222
λ_p (Input Inductor)	0.509	0.363	0.362	0.5099	0.362	0.362	0.5099	0.362	0.362
λ_p (Output Capacitor)	0.060	0.060	0.060	0.0713	0.071	0.071	0.084	0.084	0.084
λ_p (Output Resistor)	0.0297	0.0297	0.0297	0.0297	0.0297	0.0297	0.0297	0.0297	0.0297
Total λ_p	77.59	259.46	264.85	92.25	93.82	394.94	104.60	607.26	661.19
MTBF (hours)	12888	3854	3775	10839	10658	2532	9560	1646	1512

ACKNOWLEDGMENT

We thank the Department of Electrical Engineering, National Institute of Technology, Warangal for providing excellent environment to do this work.

APPENDIX

In this section, the sample calculation for failure rate for each component is presented:

a) Calculation of Failure rate λ_p for MOSFET (IXFH12N100Q/IXS) :

$$V_n=1000V, \theta_{jc}=0.42^\circ C/W, \theta_{ca}=1^\circ C/W$$

$$T_c = T_a + \theta_{ca} \times P_{loss} = 27+1 \times 69.163875=96.163875$$

$$T_j = T_c + \theta_{jc} \times P_{loss} = 96.163875+0.42 \times 69.163875 = 125.2127$$

$$\pi_T = \exp\left(-1925 \times \left(\frac{1}{T_j+273} - \frac{1}{298}\right)\right) = 5.08162$$

$$\lambda_b=0.012, \pi_E=6, \pi_A=10, \pi_Q=5.5$$

$$\lambda_p = \lambda_b \times \pi_Q \times \pi_E \times \pi_A \times \pi_T = 0.012 \times 5.5 \times 6 \times 10 \times 5.08162 = 20.1232$$

b) Calculation of failure rate (λ_p) for Output diode:

$$V_n=1000V, \theta_{jc}=2^\circ C/W, \theta_{ca}=1, P_{loss}=1.99056W$$

$$T_c = T_a + \theta_{ca} \times P_{loss} = 27+1 \times 1.99056 = 28.99056$$

$$T_j = T_c + \theta_{jc} \times P_{loss} = 27+ 1 \times 1.99056 = 32.97168$$

$$\pi_T = \exp\left(-1925 \times \left(\frac{1}{T_j+273} - \frac{1}{298}\right)\right) = 1.183291$$

$$\lambda_b=0.069, \pi_E=6, \pi_Q=5.5, \pi_C=1$$

$$V_S = \frac{90}{500} = 0.18 \Rightarrow \pi_S = V_S^{2.43} = 0.01549$$

$$\lambda_p = \lambda_b \times \pi_Q \times \pi_S \times \pi_E \times \pi_T \times \pi_C = 0.069 \times 5.5 \times 0.015 \times 6 \times 1.183291 \times 1 = 0.041735$$

c) Calculation of failure rate(λ_p) for Input Bridge:

$$V_n=1000V, \theta_{jc}=1.6^\circ C/W, P_{loss}=3.8808 W$$

$$T_c = T_a + \theta_{ca} \times P_{loss} = 27+ 1 \times 3.8808 = 30.8808$$

$$T_j = T_c + \theta_{jc} \times P_{loss} = 30.8808 + 1.6 \times 3.8808 = 37.09008$$

$$\pi_T = \exp\left(-1925 \times \left(\frac{1}{T_j+273} - \frac{1}{298}\right)\right) = 1.286413$$

$$\lambda_b=0.069, \pi_E=6, \pi_Q=5.5, \pi_C=1$$

$$V_S = \frac{304}{1200} = 0.2533 \Rightarrow \pi_S = V_S^{2.43} = 0.03554$$

$$\lambda_p = \lambda_b \times \pi_Q \times \pi_E \times \pi_C \times \pi_S \times \pi_T = 0.069 \times 5.5 \times 6 \times 1 \times 0.03554 \times 1.286413 = 0.104102$$

d) Calculation of failure rate(λ_p) for Inductor:

$$T_{HS} = T_A + 1.1 \times \Delta T = 27 + 1.1 \times 11 = 39.1$$

$$\lambda_b = 0.0016 \times \left(\frac{T_{HS} + 273}{329}\right)^{15.6} = 0.70282m$$

$$\pi_E=6, \pi_Q=20;$$

$$\lambda_p = \lambda_b \times \pi_Q \times \pi_E = 0.070282 \times 10^{-3} \times 6 \times 20 = 0.08433$$

e) Calculation of failure rate for Capacitor:

$$\Pi_{CV} = 0.34 \times C^{0.18} = 0.34 \times (917\mu)^{0.18} = 0.09653$$

$$\pi_E=2, \pi_Q=10;$$

$$\lambda_p = \lambda_b \times \pi_Q \times \pi_E \times \pi_{CV} = 0.13 \times 10 \times 2 \times 0.09653 = 0.250978$$

f) Calculation of failure rate for Resistor:

$$\pi_R=1, \pi_E=2, \pi_Q=10, \lambda_b = 0.000066;$$

$$\lambda_p = \lambda_b \times \pi_Q \times \pi_E \times \pi_R = 0.00066 \times 10 \times 2 \times 1 = 0.0297$$

Therefore the total system failure rate will be:

$$\lambda_{system} = \sum_{n=1}^N \lambda_{part} = 20.634 \text{ (failures/ } 10^6 \text{ hours)}$$

$$\Rightarrow MTBF = \frac{1}{\lambda} = 48463.70$$

REFERENCES

- [1] Reliability aspects on power supplies, design note 02 EN/LZT 14600 RIA (C Ericsson Microelectronics AB, April, 2001).
- [2] European power supply manufacturing association, "Guidelines for understanding Reliability Prediction", June, 2005
- [3] C. Zhou, M. Jovanovic, "Design trade-offs in continuous current-mode controlled boost power-factor correction circuits", HFPC Conf. proc. May 1992, pp. 209-219.
- [4] C. Zhou, R. B. Ridley and F. C. Lee, "Design and analysis of a hysteretic boost power factor correction circuit", PESC Conf. Proc.1990, pp. 800-807.
- [5] Jindong Zhang, "Advanced integrated single stage power factor correction techniques" Ph.D thesis, Virginia tech., 15 March 2001.
- [6] Dao-Shen Chen, Jih-Sheng Lai, "A Study of power correction boost converter operating at CCM-DCM mode", Proceedings of IEEE Southeastcon'93, 4-7 Apr 1993.
- [7] Chin Chang; Knights, M.A. "Interleaving technique in distributed power conversion systems", IEEE Transactions on Circuits and Systems: Fundamental Theory and Applications, Vol. 42, Issue 5, May 1995, pp.245 – 251.
- [8] Takuya Ishii and Yoshio Mizutani, "Power Factor Correction using Interleaving Technique for Critical Mode Switching Converters", PESC'98, Vol.1, May 1998, pp. 905-910.
- [9] B.A. Miwa and M.F. Schlecht, "High efficiency power factor correction using interleaving techniques", Applied Power Electronics Conference and Exposition (APEC '92), 23-27 Feb. 1992, pp.557 - 568.

- [10] Abdi, M.B.Menhaj, L.Yazdanparast, J.Milimonfared, "The effect of the transformer winding on the reliability of switching power supplies", 12th International PEMC Aug 2006- Sept 2006, pp.663 – 667.
- [11] B.Abdi, A.H.Ranjbar, J.Milimonfared, .B.Gharehpetian, "Reliability comparison of boost PFC converter in DCM and CCM operating modes", International Symposium on Power Electronics, Electrical Drives, Automation and Motion Conference (SPEEDAM), 11-13 June 2008, pp: 939-943.
- [12] MIL-HDBK-217, "Reliability prediction of electronic equipment", 1991.

BIOGRAPHIES



A. Praveenkumar received his B. Tech degree in electrical engineering from Jawaharlal Nehru Technological University, Anantapur, India in 2006. and M. Tech degree from National Institute of Technology, Warangal India in 2009. His research interests include DC-DC converter for power factor correction, Distributed power system.



Gulam Amer has obtained the B.E. in instrumentation engineering from Osmania University, Hyderabad, India in 2002 and M.Tech in Power Electronics from Vishweshwaraya technological university, Belgaum, India. He is presently doing research at National Institute of Technology Warangal, India.. His research interests include DC-DC Converter, SMPS, Power factor correction circuits, distributed power system and telecom power supply. He is the life member of ISTE and BMESI. He is also student member of IEEE.



S. Srinivasa Rao received his B.Tech degree in electrical engineering from Regional Engineering College, Warangal, India, in 1992 and M. Tech degree from Regional Engineering College, Calicut, India, in 1994. He obtained his Ph. d degree from National Institute of Technology Warangal in 2007. Since 1996 he is working as a faculty member in National Institute of Technology Warangal, India. He published many papers in international journals and conferences. His research interests include power electronic drives, DSP controlled drives and non-conventional power generation. He is a Life Member in Systems Society of India (SSI) and Society for Technical Education (ISTE) and Member in Institution of Engineers (India).

Control Technologies in Distributed Generation System Based on Renewable Energy

Jie Wu¹ Sizhe Chen¹ Jun Zeng¹ Lamei Gao¹

Abstract – Great efforts have been done to distributed renewable energy (RE) power system in latest years. This paper summarizes the research achievements of New Energy Research Center (a research center in Electric Power College, South China University of Technology) in distributed RE power system. The paper is mainly divided into three parts, including wind energy generation, photovoltaic generation and energy management system. Firstly, the wind energy generation control technologies is presented in variable speed constant frequency, maximum wind power capture, power decoupled control, pitch control, low voltage ride through, and grid synchronization. Secondly, the photovoltaic generation control technologies is introduced including photovoltaic maximum power point tracing, configuration and optimization of photovoltaic array and grid-connected converter. Lastly, the energy management system is proposed as the super manage layer to hybrid REs, which including wind speed forecast, integrative evaluate to power quality, power quality analytical instrument and the construction of energy management system based on multi-agent technology.

Keywords – Distributed generation, Wind energy generation, Photovoltaic generation, Energy management system

This paper introduces the research results of NERC, which focuses on the complex dynamic control technologies in distributed RE power system. Some simple or mature control technologies are out of the scope of this article, such as battery charging, braking and yawing.

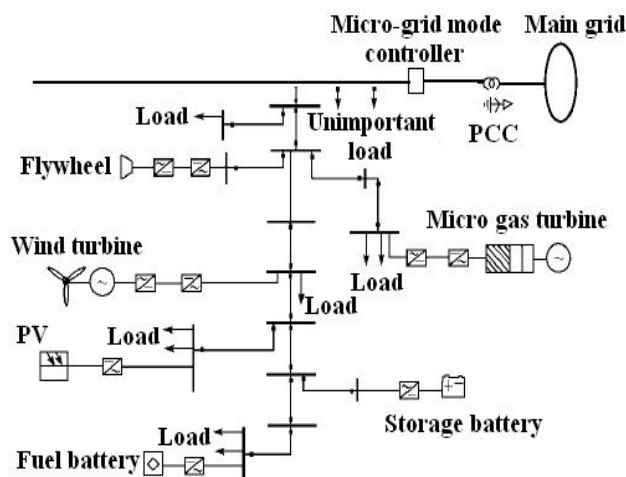


Fig. 1 Structure of distributed generation system

I. INTRODUCTION

With the gradual depletion of fossil energy resources and the increasingly serious issue of environmental pollution, great concern is paid to the development of renewable energy (RE), such as wind and solar energy. The development of distributed RE power system play more and more important role in traditional power system as a useful complement to the grid. It is a good way to reduce energy consumption, improve flexibility and reliability of power system.

The distributed power system generally refers to relatively small-scale power generation system (typically 50 MW or less). It is mainly made up of RE, including bio-energy power generation, solar power, wind energy and small-scale gas turbine power generation and energy storage devices. It is always located at the user-site nearby, which can be connected to power grid or isolated operated as shown in Fig.1.

In the latest years, great efforts have been done in distributed RE power system at the New Energy Research Center of South China University of Technology. Nowadays, Guangdong Key Laboratory of Clean Energy Technology is built based on these research achievements.

II. CONTROL TECHNOLOGIES IN WIND ENERGY GENERATION

A. Variable speed constant frequency

In order to improve the efficiency and power quality of wind energy conversion system (WECS), achieve variable speed constant frequency (VSCF) generation, and get rid of the slip ring maintenance in conventional doubly-fed induction generation (DFIG), a brushless doubly-fed machine (BDFM) is designed and manufactured [2]. The structure of BDFM is shown in Fig.2. There are two windings in the stator: power winding and control winding. The pole pair number of power winding p_p is four, and the pole pair number of control winding p_c is one. The relations among power winding frequency f_p , control winding frequency f_c and rotary frequency f_r is given as

$$f_r = \frac{f_p \pm f_c}{p_p + p_c} \quad (1)$$

Under different rotary speed, the power winding frequency can be controlled to follow the grid frequency by adjusting the frequency of control winding exciting converter, and hence VSCF will be achieved. Fig.3 shows the voltage of the BDFM power winding under different rotary speed and load conditions. When the rotary speed changed, the power winding frequency can be keep at 50 Hz by adjusting the exciting converter frequency.

This paper has been published in PESA09 Conference and has been selected to be published in this APEJ issue.

¹College of Electric Power, South China University of Technology, Guangzhou, China, 510640E-mail:epjiewu@scut.edu.cn

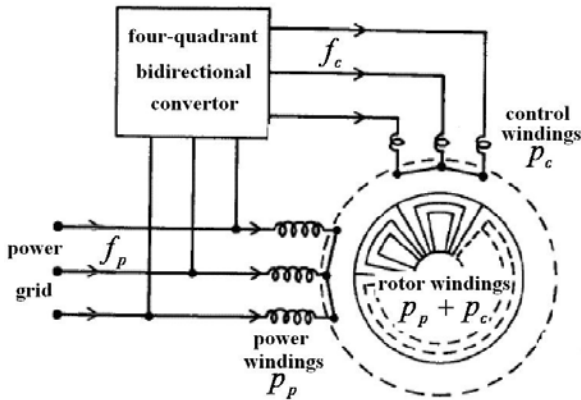
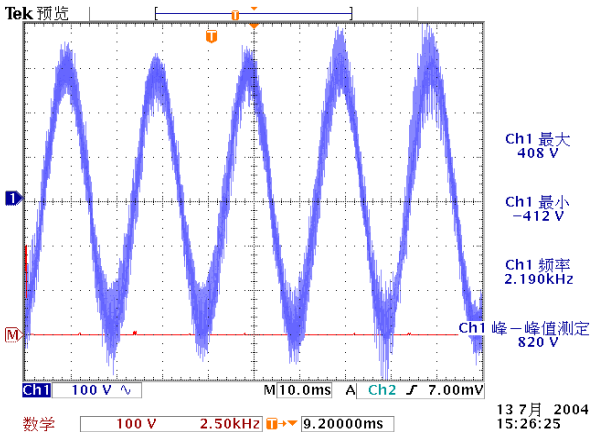
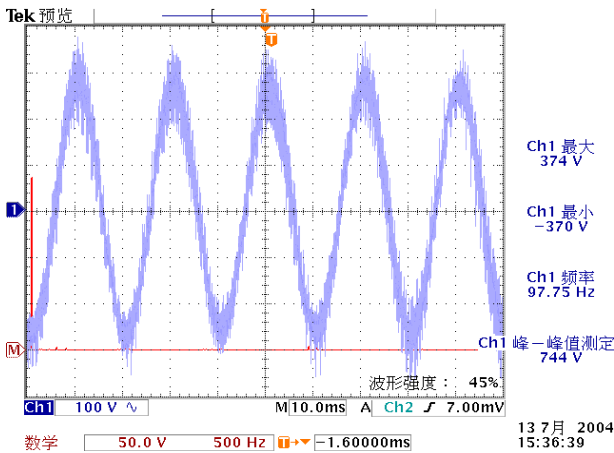


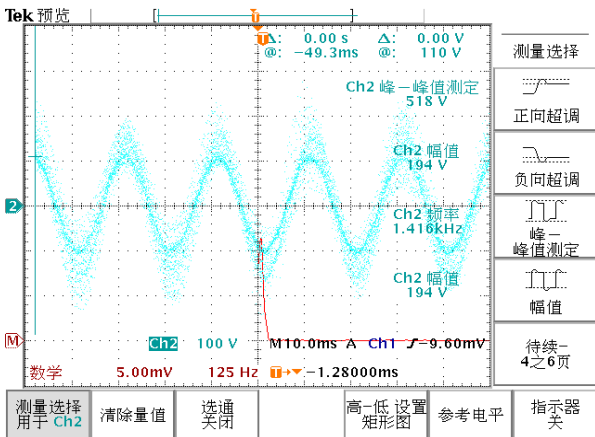
Fig.2 Structure of BDFM



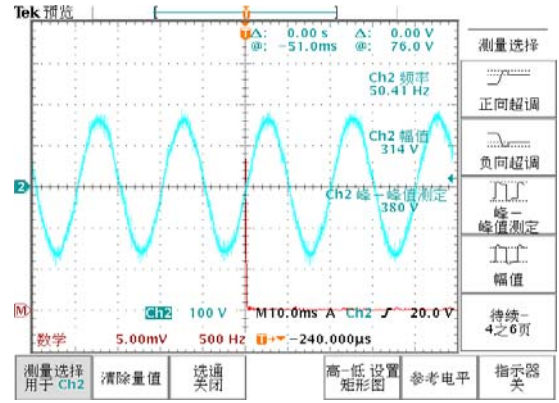
(a). $n_r=540$ rpm, $f_c=5.0$ Hz, no load



(b). $n_r=540$ rpm, $f_c=5.0$ Hz, with resistance load



(c). $n_r=504$ rpm, $f_c=8.0$ Hz, no load



(d). $n_r=504$ rpm, $f_c=8.0$ Hz, with resistance load

Fig. 3 Voltage of BDFM power windings under different rotary speed and load condition

B. Maximum wind power capture

Fig.4 shows the relations among wind power, wind speed and rotary speed. Under different wind speed, the blade tip speed ratio λ of maximum power point is a constant. The principle of maximum power point tracking (MPPT) control is to adjust the rotary speed of wind turbine according to wind speed, and keep the wind turbine working at optimal blade tip speed ratio λ_{opt} . The dashed line in Fig.4 is the maximum power curve under different wind speed, and it's given as

$$P_{mopt} = \frac{1}{2} C_{pmax} \rho \pi R^2 \left(\frac{\omega_r R}{\lambda_{opt}} \right)^3 \quad (2)$$

where, C_{pmax} is the maximum wind power coefficient, ρ is the air density, R is the radius of wind turbine, ω_r is the rotary speed of wind turbine.

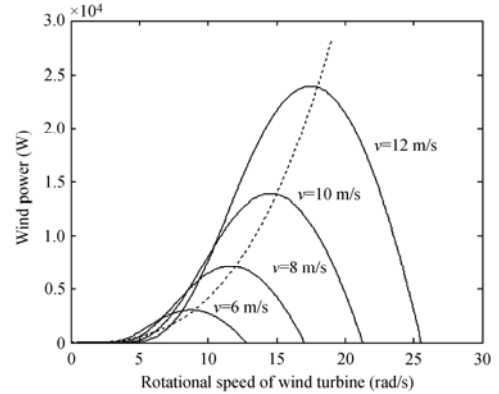


Fig.4 Relations between wind power captured and rotary speed under different wind speed

C. Power decoupled control

The BDFM is a time varying, nonlinear and strong coupled system, whose model is very complex (Fig.5) [3]. The power decoupled control is a difficulty in wind turbine control systems. The voltage-forced mode of the BDFM in the rotor speed d-q axis coordinate frame is given as [4]:

$$\begin{bmatrix} u_{qp} \\ u_{dp} \\ u_{qc} \\ u_{dc} \\ 0 \\ 0 \end{bmatrix} = \begin{bmatrix} r_p + L_{sp}p & 3\omega_r L_{sp} & 0 & 0 & M_p p & 3\omega_r M_p \\ -3\omega_r L_{sp} & r_p + L_{sp}p & 0 & 0 & -3\omega_r M_p & M_p p \\ 0 & 0 & r_c + L_{sc}p & \omega_r L_{sc} & -M_c p & \omega_r M_c \\ 0 & 0 & -\omega_r L_{sc} & r_c + L_{sc}p & \omega_r M_c & M_c p \\ M_p p & 0 & -M_p p & 0 & r_r + L_r p & 0 \\ 0 & M_p p & 0 & M_c p & 0 & r_r + L_r p \end{bmatrix} \begin{bmatrix} i_{qp} \\ i_{dp} \\ i_{qc} \\ i_{dc} \\ i_{qr} \\ i_{dr} \end{bmatrix} \quad (3)$$

where, $r_p, L_{sp}, r_c, L_{sc}, r_r, L_r$ are the resistances and self-inductions of power winding, control winding, and rotor windings, respectively, and M_p, M_c are the inductions among power windings, control windings and rotor windings.

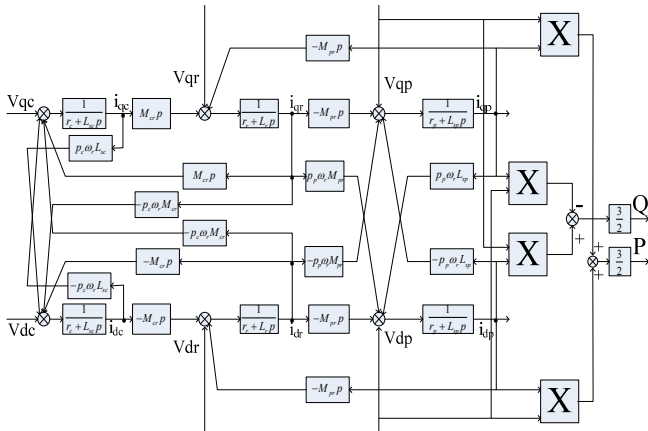


Fig. 5 Model of BDFM

Basing on (3), reference [5] and [6] developed the state space model as

$$\begin{bmatrix} \dot{x}_1 \\ \dot{x}_2 \\ \dot{x}_3 \\ \dot{x}_4 \end{bmatrix} = \begin{bmatrix} 0 & 1 & 0 & 0 \\ a_{21} & a_{22} & \omega_r a_{23} & -\omega_r \\ 0 & 0 & 0 & 1 \\ -\omega_r a_{23} & \omega_r & a_{21} & a_{22} \end{bmatrix} \begin{bmatrix} x_1 \\ x_2 \\ x_3 \\ x_4 \end{bmatrix} \quad (4)$$

$$+ \frac{1}{k} \begin{bmatrix} 0 & 0 \\ 1 & 0 \\ 0 & 0 \\ 0 & -1 \end{bmatrix} \begin{bmatrix} u_{dc} \\ u_{qc} \end{bmatrix} + \begin{bmatrix} 0 & 0 \\ 1 & 0 \\ 0 & 0 \\ 0 & 1 \end{bmatrix} \begin{bmatrix} f_{dc} \\ f_{qc} \end{bmatrix}$$

where, $x_1 = \int i_{dr} dt, x_2 = i_{dr}, x_3 = \int i_{qr} dt, x_4 = i_{qr},$

$$a_{21} = \frac{r_c}{M_c k} r_r, \quad a_{22} = (L_r - \frac{M_p^2}{L_{sp}}) \frac{r_c}{M_c k} + \frac{L_{sc}}{M_c k} r_r,$$

$$a_{23} = \frac{L_{sc}}{M_c k} r_r, \quad k = (L_r - \frac{M_p^2}{L_{sp}}) \frac{L_{sc}}{-M_c} + M_c,$$

$$f_{dc} = \sqrt{\frac{3}{2}} \frac{M_p V}{L_{sp} M_c k \omega_{1p}} [(4\omega_r - \omega_{1p}) L_{sc} \sin \theta_{pe} + r_c \cos \theta_{pe}],$$

$$f_{qc} = \sqrt{\frac{3}{2}} \frac{M_p V}{L_{sp} M_c k \omega_{1p}} [(\omega_{1p} - 4\omega_r) L_{sc} \cos \theta_{pe} + r_c \sin \theta_{pe}]$$

The active power and reactive power of power winding in the power winding synchronous rotary coordinate frame is given as

$$P_p = \frac{3}{2} (u_{qp}^{pe} i_{qp}^{pe} + u_{dp}^{pe} i_{dp}^{pe}) = -\frac{3}{2} V \frac{M_p x_4^{pe}}{L_{sp}} \quad (5)$$

$$Q_p = \frac{3}{2} (u_{qp}^{pe} i_{dp}^{pe} - u_{dp}^{pe} i_{qp}^{pe}) = \frac{3}{2 L_{sp}} V \left[\sqrt{\frac{3}{2}} \frac{V}{\omega_p} - M_p x_2^{pe} \right] \quad (6)$$

The active power reference is set according to the MPPT curve given by (2), and the reactive power reference is set according to the requirement of power grid. Reference [6] applies auto disturbance rejection control (ACRC) [7] into the power decoupled control of BDFM. Fig.6 shows the diagram of control system, in which the convertor

uses AC-AC matrix convertor [8]. Simulation results are shown in Fig.7 and Fig.8. In Fig.7, the reference of reactive power is constant and the wind speed changes. The rotary speed of wind turbine changes according to the wind speed, and the power coefficient keeps at the maximum value, which means MPPT is achieved. In Fig.8, the wind speed is constant and the reference of reactive power is step changed. The reactive power tracks the reference quickly when the rotary speed and active power are almost unchanged, and the power coefficient is still kept at the maximum value. The ADRC effectively achieved the MPPT and power decoupled control of BDFM. Fig.7 (d) and Fig.8 (d) shows the output voltage of matrix convertor which is applied at control winding.

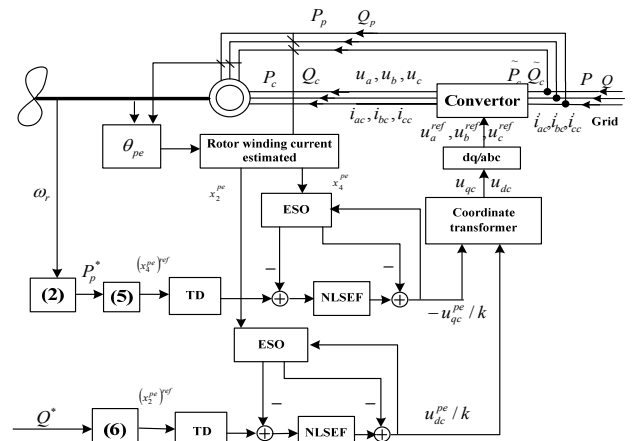
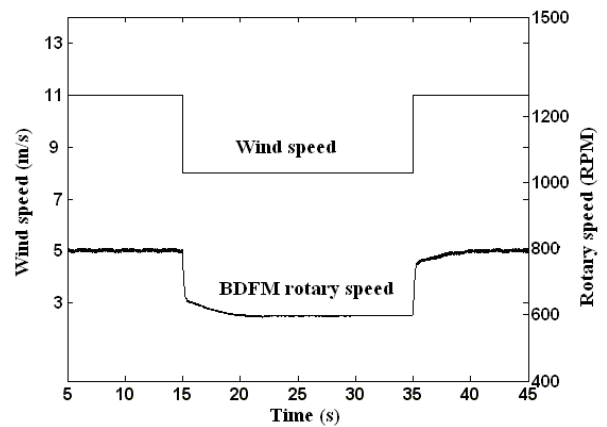
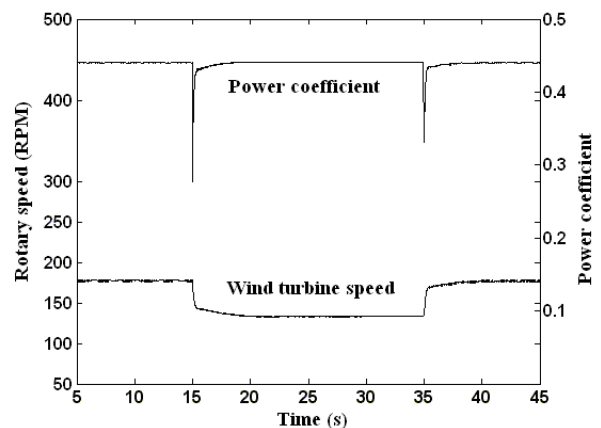


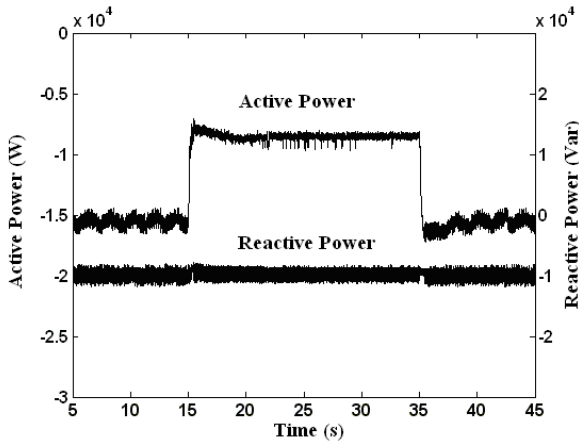
Fig.6 Power decoupled control diagram of the WECS with the BDFM



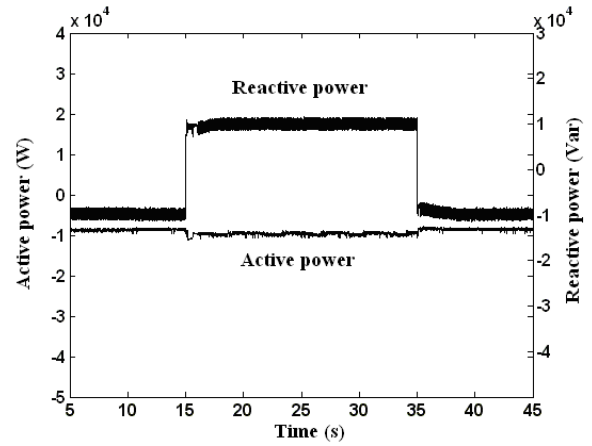
(a) Wind speed and BDFM rotary speed



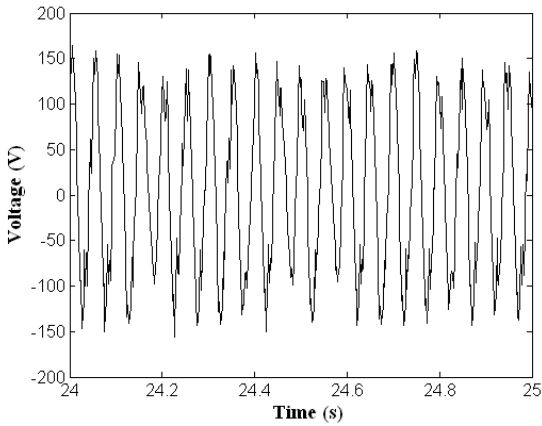
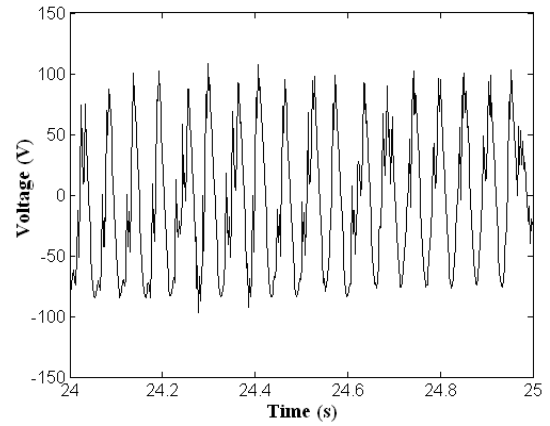
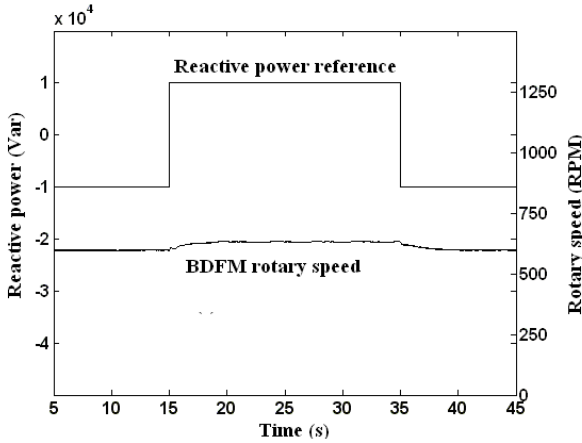
(b) Wind turbine rotary speed and power coefficient



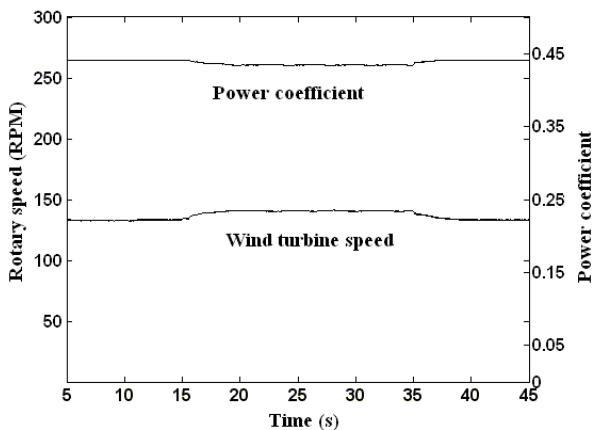
(c) Power output of the power windings



(c) Power output of the power windings


 (d) Voltage output of the matrix converter
 Fig.7 Response to step changed of wind speed

 (d) Voltage output of the matrix converter
 Fig.8 Response to step changed of reactive reference value


(a) Reactive power reference and BDFM rotary speed



(b) Wind turbine rotary speed and power coefficient

D. Pitch control

Torque control and pitch control can both limit the power capture of wind turbine when wind speed is above rated value. However, if only torque control is used, the generator has to offer large electromagnetic torque to reduce the rotary speed of wind turbine [9]. Large energy stored as rotor kinetic energy will transfer into power grid and lead to power fluctuation. Reference [10] present a pitch control method based on H-infinity control. The pitch angle of wind turbine is adjusted to keep the rotary speed and torque at rated value. The mechanical system nonlinear model of variable speed pitch control wind turbine is given as

$$\begin{cases} \dot{\omega}_r = -\frac{B_{ls} + K_r}{J_r} \omega_r + \frac{B_{ls}}{J_r n_g} \omega_g - \frac{K_{ls}}{J_r} \theta + \frac{1}{J_r} T_a \\ \dot{\omega}_g = \frac{B_{ls}}{J_g n_g} \omega_r + \left(\frac{K_g}{J_g} - \frac{B_{ls}}{J_g n_g^2} \right) \omega_g + \frac{K_{ls}}{J_g n_g} \theta - \frac{1}{J_g} T_{em} \\ \dot{\beta} = -\frac{1}{T_\beta} \beta + \frac{1}{T_\beta} \beta_r \\ \dot{\theta} = \omega_r - \frac{\omega_g}{n_g} \end{cases} \quad (7)$$

When wind speed is 13m/s, the linearized model of system near equilibrium point is given as

$$\begin{bmatrix} \dot{\omega}_r \\ \dot{\omega}_g \\ \dot{\beta} \\ \dot{\theta} \end{bmatrix} = \begin{bmatrix} -137.43 & 22.3214 & -70.0741 & -1000 \\ 22.3214 & -4.97 & 0 & 223.2143 \\ 0 & 0 & -5 & 0 \\ 1 & -0.2232 & 0 & 0 \end{bmatrix} \begin{bmatrix} \omega_r \\ \omega_g \\ \beta \\ \theta \end{bmatrix} \quad (8)$$

$$+ \begin{bmatrix} 0 \\ 0 \\ 5 \\ 0 \end{bmatrix} u + \begin{bmatrix} 214.115 \\ 0 \\ 0 \\ 0 \end{bmatrix} v$$

The transfer function matrix of system is given as

$$\omega_g = P_2 u + P_1 w \quad (9)$$

where, $P_1 = \frac{4780s^2 + 71690s + 238970}{s^4 + 147.4s^3 + 1946.6s^2 + 8025.4s + 9261.8}$,

$$P_2 = \frac{-7821s - 78208}{s^4 + 147.4s^3 + 1946.6s^2 + 8025.4s + 9261.8}$$

The control problem can be described as a standard H-infinity control problem shown in Fig.9. The transfer function between input and output is given as

$$\begin{bmatrix} z_1 \\ z_2 \\ -\omega_g \end{bmatrix} = \begin{bmatrix} -W_e P_1 & -W_e P_1 \\ 0 & W_u \\ -P_1 & -P_2 \end{bmatrix} \begin{bmatrix} v \\ \beta_r \end{bmatrix} \quad (10)$$

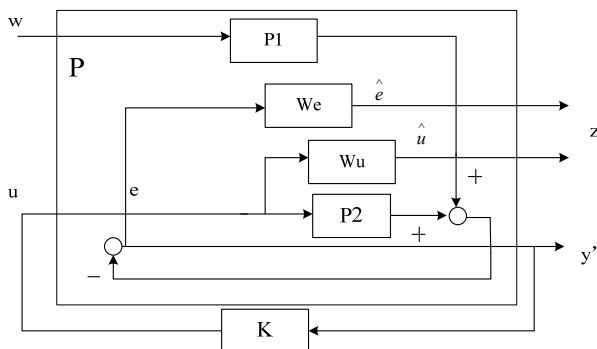
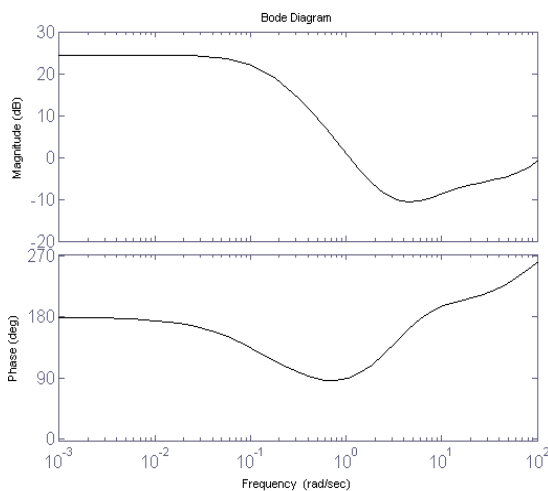


Fig.9 Standard H-infinity design diagram for power regulation

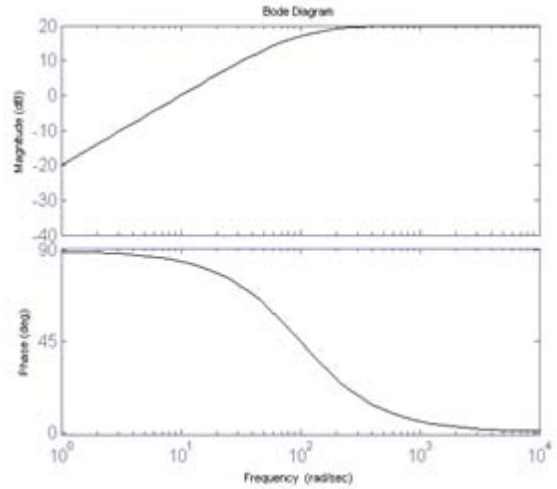
The weighting function W_e is chosen to keep the rotary speed of generator at rated value during steady state, and the weighting function W_u is used to limit the response speed of pitch angle to avoid saturation.



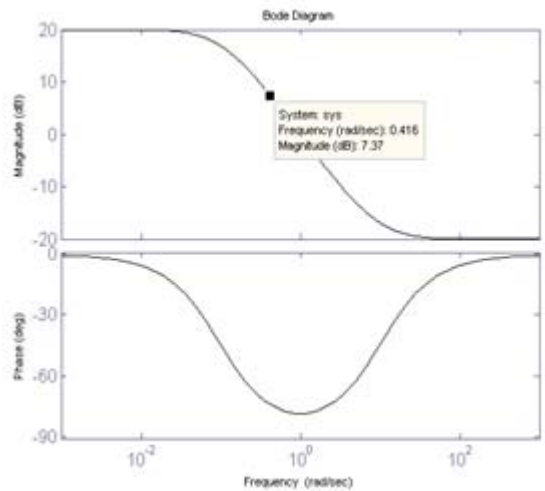
(a) Bode diagram of controller K_I

The weighting functions are chosen as (11), whose bode diagrams are shown in Fig.10.

$$W_u(s) = \frac{10s}{s+100}, \quad W_e(s) = \frac{0.1(s+10)}{s+0.1} \quad (11)$$



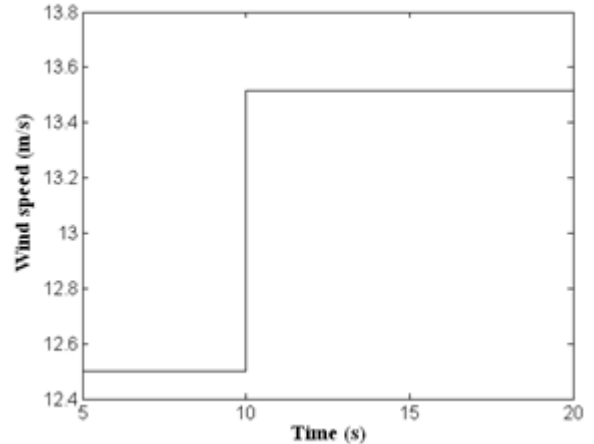
(b) Bode diagram of W_u



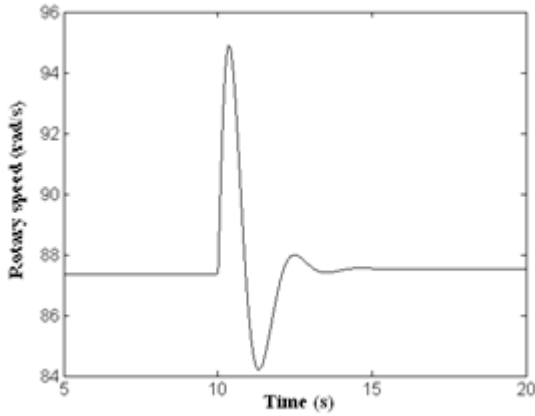
(c) Bode diagram of W_e

Fig.10 Bode diagrams of the functions

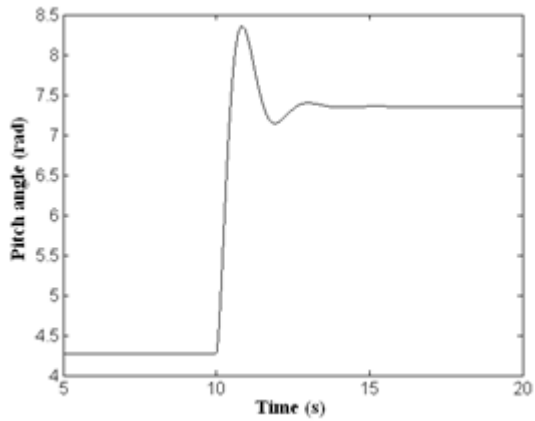
Simulation results in Fig.11 show that the pitch angle increases with wind speed, which keeps the rotary speed and capture power at rated value and hence achieves power limited control. Fig.12 shows the response of wind turbine with 5% error of rotary inertia, which verifies the robustness of controller.



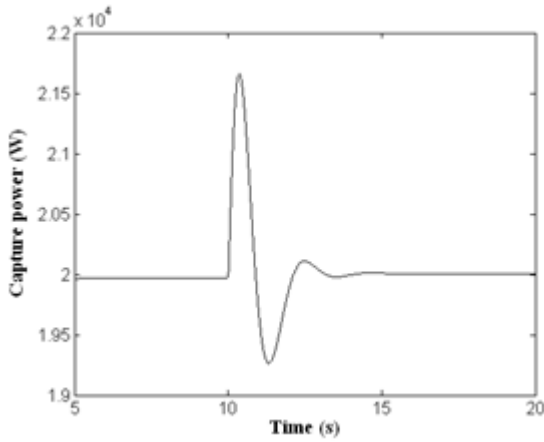
(a) Wind speed



(b) Rotary speed of generator



(c) Pitch angle



(d) Capture power

Fig.11 Dynamic response of wind turbine above rated wind speed

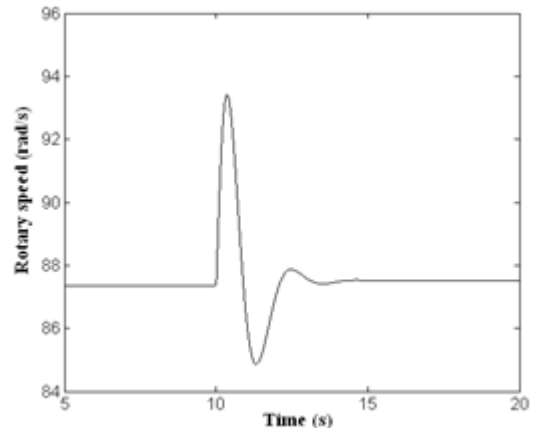


Fig.12 Rotary speed of generator with 5% error of rotary inertia

E. Low voltage ride through

The relations among rotor winding current and voltage of DFIG are given as

$$\begin{cases} \frac{di_{rd}}{dt} = \frac{u_{rd}}{\sigma L_r} - \frac{R_r i_{rd}}{\sigma L_r} + \frac{\omega_s \varphi_{rq}}{\sigma L_r} - \frac{L_m}{\sigma L_r L_s} \frac{d\varphi_{sd}}{dt} \\ \frac{di_{rq}}{dt} = \frac{u_{rq}}{\sigma L_r} - \frac{R_r i_{rq}}{\sigma L_r} - \frac{\omega_s \varphi_{rd}}{\sigma L_r} - \frac{L_m}{\sigma L_r L_s} \frac{d\varphi_{sq}}{dt} \end{cases} \quad (12)$$

Traditional control method based on ideal grid voltage always neglect the stator flux transient term in (12). When the grid voltage dips, the transient component in stator flux will induce large current in rotor winding, which may damage the exciting converter [11]. Reference [12] introduces ADRC to combine with vector control (Fig.13). The influences of disturbances, including stator transient flux and generator parameter errors, are estimated and compensated by the extended state observer (ESO).

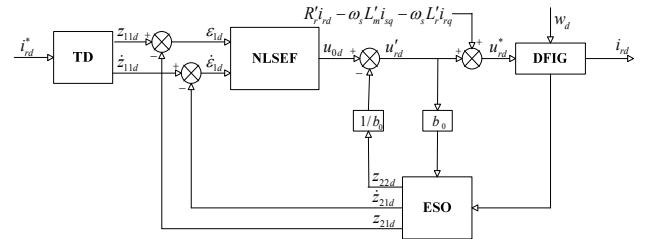
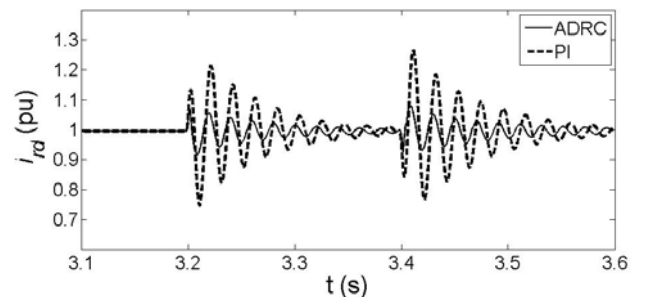
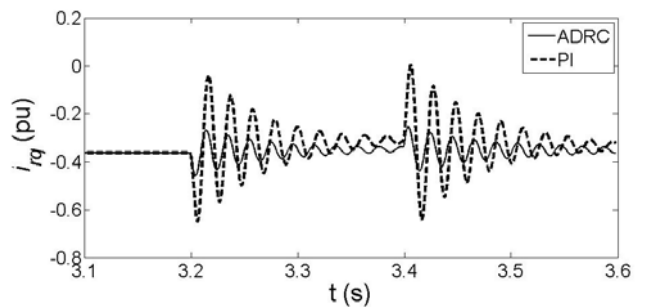


Fig. 13 ADRC of d-axis rotor current

The simulation results of traditional control and ADRC during grid voltage dip are compared in Fig.14. Because the ADRC scheme includes disturbances compensation, the voltage applied into rotor winding increases, which decreases the peak current of rotor winding. The ADRC scheme effectively avoids over current in rotor winding, and hence, protects the exciting converter during grid voltage dip. Additional simulation results in [12] show excellent robustness of ADRC against generator parameter errors.



(a) d-axis rotor current



(b) q-axis rotor current

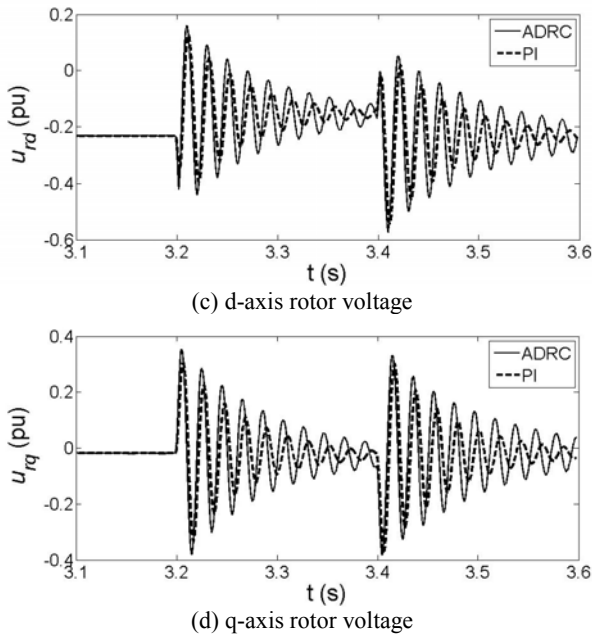


Fig. 14 Comparison of PI and ADRC control under grid voltage dip fault

F. Grid synchronization control

The control objective of grid synchronization is to control the stator direct and quadrature voltage to track the grid direct and quadrature voltage in the grid voltage reference frame, respectively, such that the stator voltage and grid voltage will have equal magnitude, frequency, and phase [13].

Cascaded control approaches are shown in Fig.15. The inner loop controls rotor current, and the outer loop minimizes the voltage differences between generator stator and power grid. The grid and stator line voltages of the DFIG are shown in Fig.16 (a) at rotor speed of 1400 rpm, and the corresponding direct and quadrature voltages are shown in Fig.16 (b). The stator voltage tracks the grid voltage rapidly and has its amplitude, frequency, and phase equalized to those of the grid voltage in several periods. The results are very similar at super-synchronous speed.

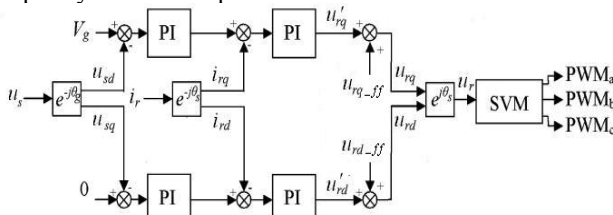
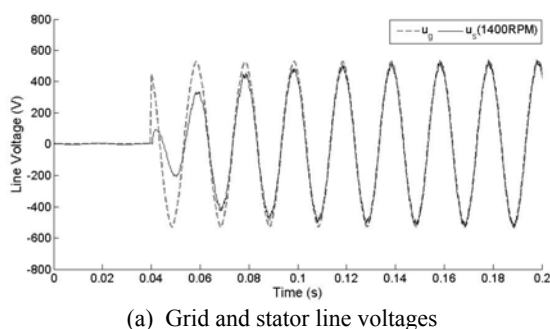
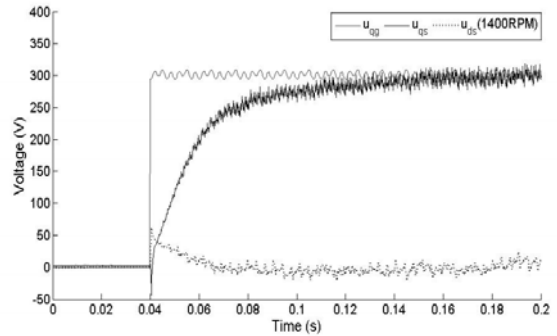


Fig.15 Control scheme of grid synchronization



(a) Grid and stator line voltages



(b) Grid, stator direct and quadrature voltages
Fig. 16 Experiment results of grid synchronization

III. CONTROL TECHNOLOGIES IN PHOTOVOLTAIC GENERATION

A. Photovoltaic maximum power point tracking

Fig.17 shows a buck-boost DC/DC converter for MPPT control of photovoltaic (PV) array [14].

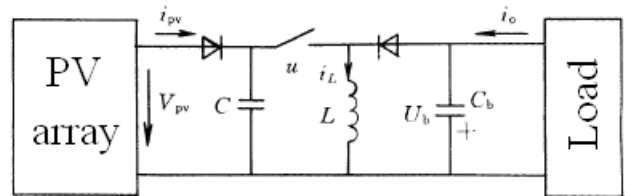


Fig.17 Photovoltaic generation system

Define u as the switching function of the switching component, $u=1$ means the switching is closed and $u=0$ means the switching is open circuit. The model of system is given as

$$\begin{cases} \dot{U}_{pv} = \frac{1}{C} i_{pv} - \frac{u}{C} i_L \\ \dot{i}_L = -\frac{1}{L} U_b + \frac{u}{L} (U_{pv} + U_b) \\ \dot{U}_b = \frac{(i_L - i_o)}{C_b} - \frac{u}{C_b} i_L \end{cases} \quad (13)$$

where, U_{pv} and i_{pv} is the terminal voltage and output current of PV array, respectively.

A MPPT control scheme of PV array based on sliding mode control is designed in [15]. The sliding surface is chosen as

$$S = \frac{\partial p_{pv}}{\partial U_{pv}} = \left(\frac{\partial i_{pv}}{\partial U_{pv}} U_{pv} + i_{pv} \right) \quad (14)$$

The switching control signal is chosen as

$$u = \begin{cases} 0 & S \geq 0 \\ 1 & S < 0 \end{cases} \quad (15)$$

Reference [15] proves that the system with controller satisfies the Lyapunov stability condition. Hence, the system can reach and finally settle in the sliding surface. The simulation result during light intensity step change is shown in Fig.18. p_{pv1} and U_{pv1} are the output power and terminal voltage of PV array with sliding mode control. p_{pv2} and U_{pv2} are the output power and terminal voltage of PV array with traditional comparative control scheme. The sliding mode control improves the response speed of MPPT.

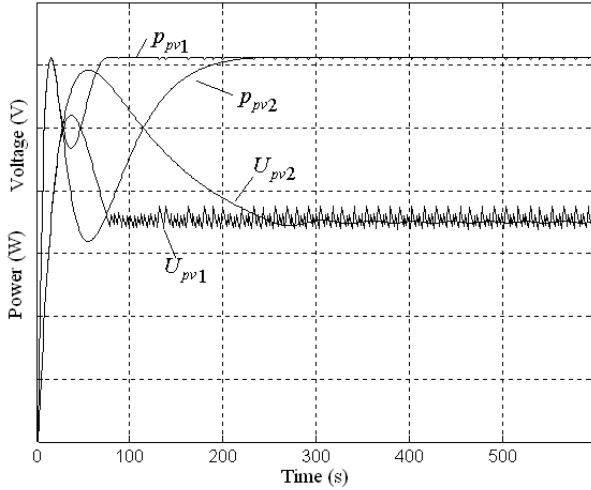


Fig. 18 The terminal voltage and output power response of PV array with light intensity step changed

B. Photovoltaic array configuration optimization control

Reference [16] presents a configuration optimization control scheme for PV array. The principle is to change the PV batteries arrangement when the temperature and light intensity of the PV batteries have large different, and make sure that all the PV batteries works near the maximum power point (MPP), which will optimize the total output power of the whole PV array.

The basic principle is as follows

(1) The optimization terminal voltages of every PV pile at the maximum power point are calculated according to the measured temperature and light intensity. If the terminal voltage difference between two PV piles, such as U_1 and U_3 , is larger than $1.5 U_m$, reconfiguration is necessary.

(2) If $(U_3 - U_1) \in ((n-0.5)U_{3m}, (n+0.5)U_{3m}]$, the reconfiguration method is as follow

If n is even, the configuration of array is changed as

$$\begin{bmatrix} U_1 \\ U_2 \\ U_3 \end{bmatrix} = \begin{bmatrix} NU_{1m} + (n/2 - 1)U + U_{3m} \\ NU_{2m} \\ (N+1-n)U_{3m} \end{bmatrix} \quad (16)$$

If n is odd, the configuration of array is changed as

$$\begin{bmatrix} U_1 \\ U_2 \\ U_3 \end{bmatrix} = \begin{bmatrix} NU_{1m} + (n-1) U / 2 \\ NU_{2m} \\ (N+1-n)U_{3m} \end{bmatrix} \quad (17)$$

where, $n \in [2, N]$, and U is the parallel connection of two U_{3m} PV batteries.

(3) If $(U_1 - U_3) \in ((n-0.5)U_{1m}, (n+0.5)U_{1m}]$, the reconfiguration method is as follow

If n is even, the configuration of array is changed as

$$\begin{bmatrix} U_1 \\ U_2 \\ U_3 \end{bmatrix} = \begin{bmatrix} (N+1-n)U_{1m} \\ NU_{2m} \\ NU_{3m} + (n/2 - 1)U + U_{1m} \end{bmatrix} \quad (18)$$

If n is odd, the configuration of array is changed as

$$\begin{bmatrix} U_1 \\ U_2 \\ U_3 \end{bmatrix} = \begin{bmatrix} (N+1-n)U_{1m} \\ NU_{2m} \\ NU_{3m} + (n-1)U / 2 \end{bmatrix} \quad (19)$$

where, $n \in [2, N]$ and U is the parallel connection of two U_{1m} PV batteries.

Simulation of a given illustration is carried out. Three PV piles mounted at different aspect of a building, such as east, south and west, have different temperature and light intensity at a moment. The temperature and light intensity is listed as 298K, 0.8kW/m²; 301K, 0.95kW/m²; 306K, 1.1kW/m². If the arrangement of the PV array is 33×3, then the power-voltage curves of three PV pile shown in Fig.19 are T_1 , T_2 , and T_3 . T is the total power-voltage curve of the whole PV array. If traditional fixed array scheme is used, only the third PV pile works at MPP, and the other two PV pile both deviate from the MPP. The total output power of the PV array is 7501W.

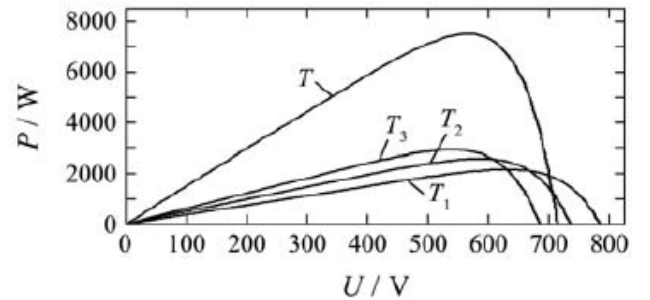


Fig.19 Power-voltage curves of PV pile with different conditions

As shown in Fig.19, the terminal voltage of three PV pile at the maximum power point are 613.8V, 573.2V and 557.6V. The terminal voltage difference between east pile and west pile satisfies $(U_1 - U_3) \in (2.5U_{1m}, 3.5U_{1m}]$, and hence the PV array should be rearranged according to (19). The result of configuration optimization is shown in Fig.20. In the new PV array after configuration optimization, only two batteries in the first pile don't work at the MPP and deviate from the MPP little. The total output power of the PV array is 7928W, which increase 5.69% before configuration optimization.

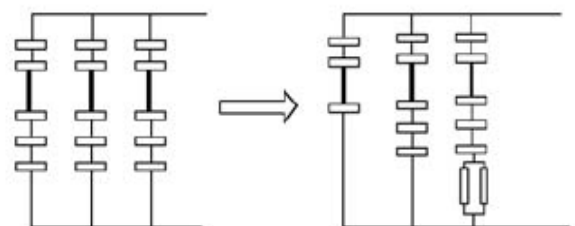


Fig.20 Configuration optimization of PV array

C. Grid-connected control for photovoltaic array

A PV grid-connected converter is shown in Fig.21 [17]. The system model neglecting high frequency switching dynamic is given as

$$\begin{cases} \frac{du_c}{dt} = -\frac{1}{R_L C} u_c - \frac{i_s}{C} u_a + \frac{1}{C} i_e \\ \frac{di_s}{dt} = -\frac{R}{L} i_s + \frac{1}{L} u_s - \frac{1}{L} u_a \end{cases} \quad (20)$$

According to the nonlinear character of the grid-connected converter, an ADRC scheme is designed in [17], whose structure is shown in Fig.22.

Cascaded control approaches are used. The inner loop is current proportion control loop, which control the output current of the converter to follow reference value. The grid voltage is considered as external disturbance, whose influence to the system is suppressed by the auxiliary feedback branch. The outer loop is voltage control loop, in which the DC side voltage is control by the ADRC. The output current of the PV array is considered as external disturbance, which is observed and compensated by the extension state observer (ESO).

The simulation results with traditional PI control scheme and proposed ADRC scheme are shown in Fig.23 and Fig.24, respectively. The overshoot of capacitor voltage and the inrush of current are suppressed by the ADRC scheme. Fig.25 shows that if the output power of PV is more than load, the phases of voltage and current of the converter are the same and energy transfers from the system to grid. Contrarily, the phases are inverted and energy transfers from grid to the system. The converter has excellent performance under both modes.

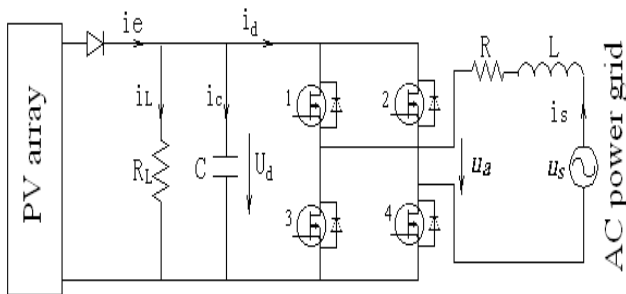


Fig.21 PV grid-connected converter

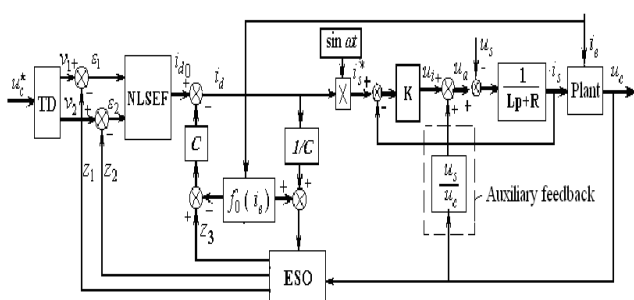


Fig.22 Control scheme of PV grid-connected converter

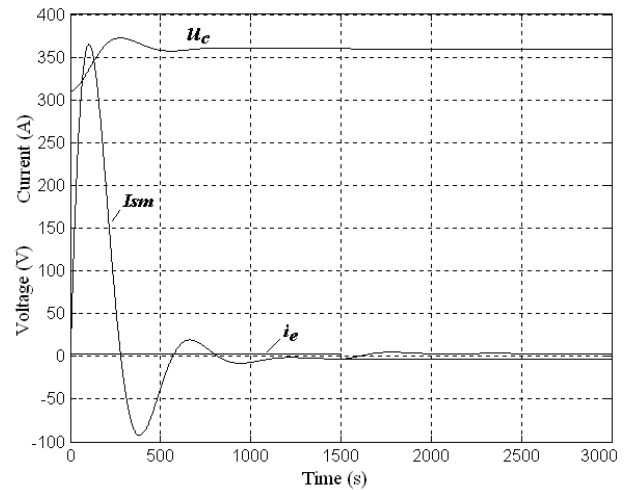


Fig.23 System response with PI control scheme

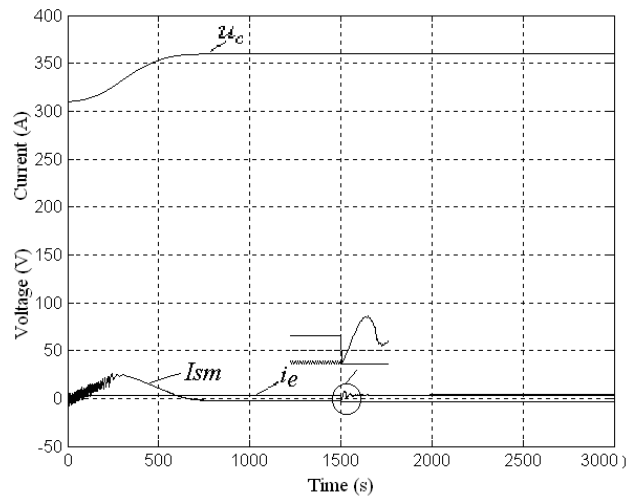
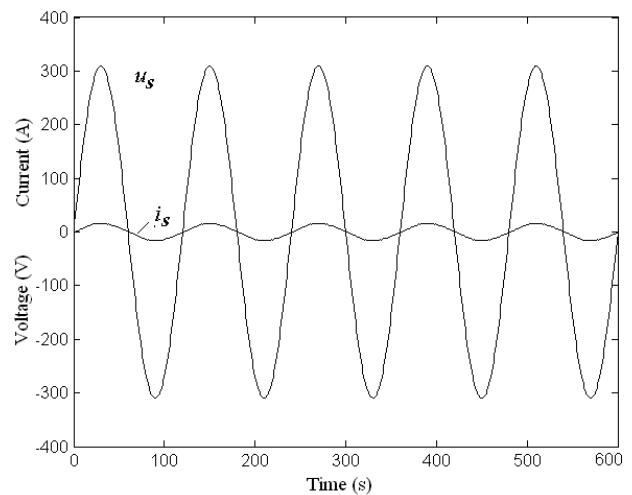
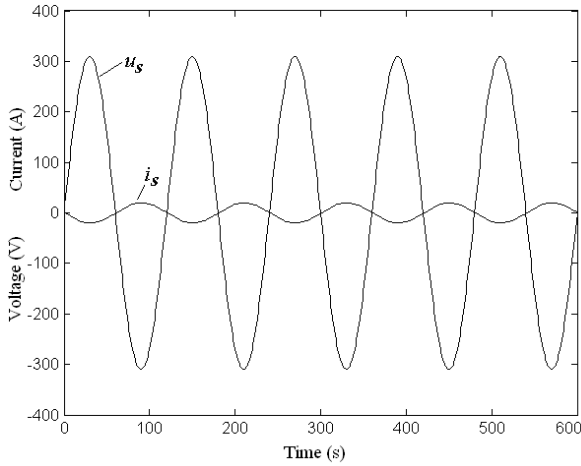


Fig.24 System response with ADRC scheme



(a) PV output power is more than load



(b) PV output power is less than load

Fig.25 Output voltage and current of PV grid-connected convertor

The hardware experimental results are shown in Fig.26 and Fig.27. In Fig.26, the first waveform is with ADRC scheme and the second waveform is with PI control scheme. The experimental results are very similar with simulation results, which also verify the better performance of ADRC. Fig. 27 shows the voltage of grid and output current of convertor, whose phase are almost the same.

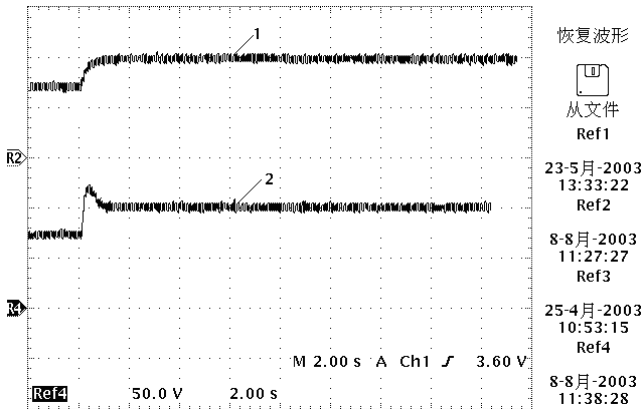


Fig.26 Experimental response of ADRC and PI

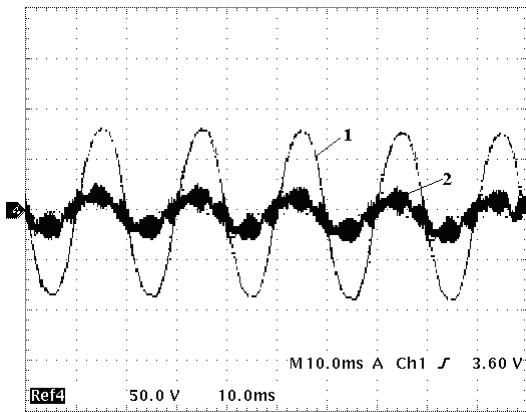


Fig.27 Grid voltage and convertor output current

IV. ENERGY MANAGEMENT SYSTEM

1. Wind Speed and power prediction

With a view to the randomness of wind, the forecast of

wind resource plays more and more important role in the scheduling system in wind power farm. Combination the forecast of wind speed and output power is a good way to improve the performance in scheduling of wind power farm. A new approach to forecast wind speed and output power were accomplished based on Box-Jenkins random time series theory [18].

Different experiments results are discussed based on different wind speed as follows.

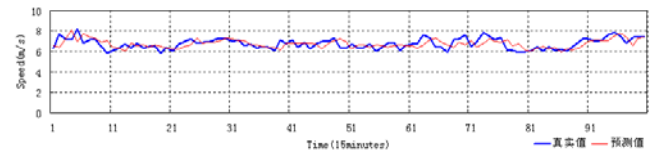
Firstly, when the wind speed is changed gently, the prediction result and absolutely error are shown in the Fig.28 (a) and (b) respectively. Where, the blue line is the initial data from Shanwei Wind Power Farm, and the red one is the result of forecast. Absolute error (AE), relative error (RE) and mean absolute error (MAE) are calculated according to equation 21.

$$\begin{aligned}
 AE &= y - \hat{y} \\
 RE &= \frac{y - \hat{y}}{y} \times 100\% \\
 MAE &= \frac{1}{N} \sum_{i=1}^N \frac{|y_i - \hat{y}_i|}{y_i}
 \end{aligned}
 \tag{21}$$

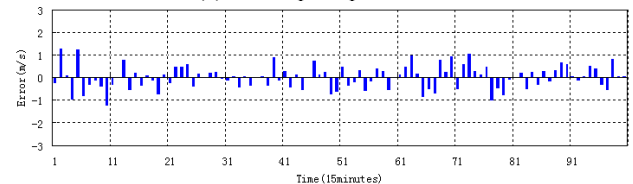
Where, y is truth value, $\hat{}$ means the value of forecast. From the Fig.28, the prediction results are good, and the MAE just hits 6.046%.

Secondly, when the wind speed is changed in a large scale, the prediction results are shown in Fig.29, and the MAE is 9.21%. The results show good performance of this algorithm, which can be used in wind power farm in future.

The output power of wind turbine is also accomplished by the same algorithm. The experiment results are shown in Fig.30. The MAE hits 16.62%.

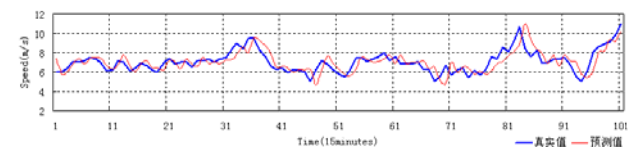


(a) Wind speed prediction

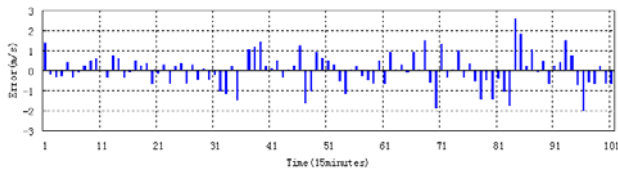


(b) Absolute error

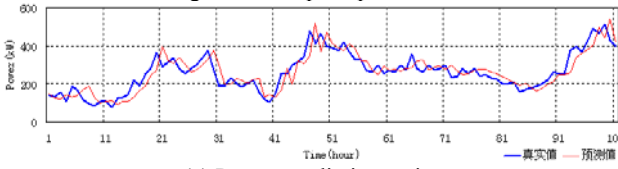
Fig.28 Wind speed prediction in real time



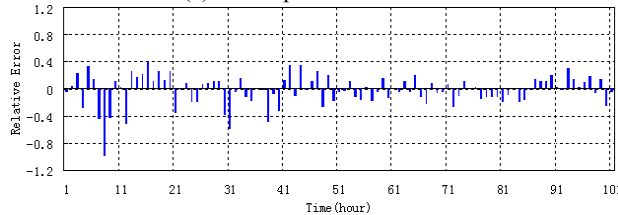
(a) Wind speed prediction



(b) Absolute error
Fig.29 Wind speed prediction



(a) Power prediction series



(b) Relative error in power prediction
Fig.30 Power prediction

2. Power Quality

Due to the intermittence and uncontrollable of RE, doubts to the power quality and stability of RE power system are the main hindrance to develop RE power system. As a result, evaluation and monitoring of power quality plays most important role in RE power system.

2.1. Power quality evaluation

According to IEEE-Std100-1992, we introduced six indexes of power quality in RE power, including Voltage Sags, Frequency Deviation, Voltage Fluctuation, Flicker, Waveform Distortion, and Three-phase Unbalanced [19]. Especially, power fluctuation is proposed with a view to the characteristics of RE, which be defined as follows.

$$\Delta P_n = \frac{P_{nt} - P_{(n-1)t}}{t} \times 100\% \quad (22)$$

$$D_P = \frac{P_{max} - P_{min}}{P_N} \times 100\% \quad (23)$$

Where, P is the output power, n is sampling number, t is sampling time. ΔP_n and D_P are the variable rate and amplitude rate of output power respectively. P_N is the root mean squares of all sampling data during sampling period, P_{max} and P_{min} are the maximum and minimum value.

Analytic hierarchy process (AHP) is adopted to obtain weight for each index as defined above. Then, to evaluate power quality of RE, a synthetic evaluation approach is proposed as follows, which combines probability and statistics with fuzzy mathematics.

Step 1, define evaluation period, $T=t$;

Step 2, each index is divided into m qualification ranks with step length as $\Delta q=x/m$. Where, $m \geq 10$, x is the limit value of each index according to national standard.

Step 3, summing the time when data locates in the same rank.

$$\tau(k) = \sum_{i=1}^n t_i \quad (24)$$

Where, t_i is the i time period when the absolute value of index locate in the rank k , n is the total number of times when the absolute value of index locate in the rank k .

Step 4, calculate the probability distribution of index at rank K , and then forming a $1 \times m$ matrix.

$$P_k = \tau(k) / T \quad (25)$$

$$R' = [p_1, p_2, p_3, \dots, p_m] \quad (26)$$

Step 5, integrate all the indexes' matrix into a $8 \times m$ matrix

$$R = [R_{VS} \ R_{TPU} \ R_{VF} \ R_{WD} \ R_{FD} \ R_F \ R_{\Delta P} \ R_{DP}] \quad (27)$$

where, $R_Z, R_T, R_V, R_X, R_P, R_S, R_B, R_G$ are matrix of voltage sags, three-phase unbalanced, voltage fluctuation, harmonic distortion, frequency deviation, flicker, power fluctuation ΔP and D_P respectively.

Step 6, Adopt analytic hierarchy process (AHP) to obtain weight for each indexes, and let assessment value as $V=W \times R$, where,

$$W = [W_{VS} \ W_{TPU} \ W_{VF} \ W_{WD} \ W_{FD} \ W_F \ W_{\Delta P} \ W_{DP}]$$

the suffixes are defined as step 5.

Step 7, Apply Additive Weight Method in V , get the assessment value.

$$V' = \sum_{k=1}^m kV_k / \sum_{k=1}^m V_k \quad (28)$$

Where, V' is the final assessment result.

2.2. A portable power quality analyzer

We developed a new portable power quality analyzer based on dual CPU (DSP+ARM). Data process and communication are divided into two parts with different CPU. DSP is designed to charge data process and sent information to ARM via SCI communication port. ARM is designed to compute, display and storage the data from DSP. Further more, ARM also supplies another communication port which can joint into monitor net based on optical Ethernet network as shown in Fig.31 [20].

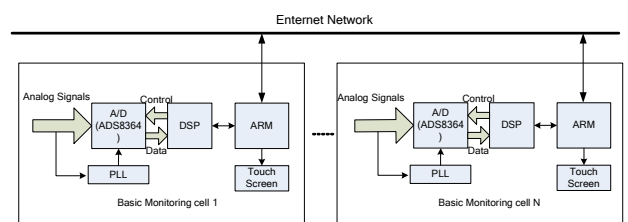
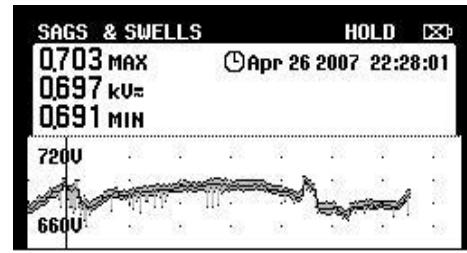


Fig.31 The power quality monitoring network based on optical fiber ethernet.

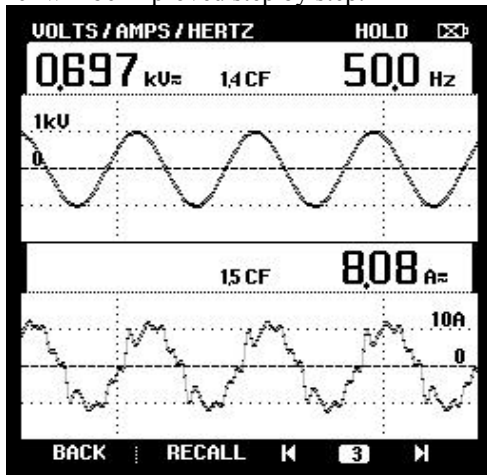
The simultaneous Data Acquisition System (DAS) is based on synchronized Phase Lock Loop (PLL), which can track the frequency of the input signal. And Fast Fourier Transform Spectrum Analysis (FFTSA) is introduced into the system to improve the accuracy and reliability greatly. The chip ADS8364, a multi-channel simultaneous chip, measures three-phase voltage and current simultaneously. So, it analyzes the power quality with high accuracy. This is a great development of the general equipment which just evaluates the single phase power quality.

A series of experiments have been done with this power quality analyzer in Shanwei Red Bay, Guangdong province. From the results of practically application, the power quality analyzer not only obtained parameters from power quality from several wind turbines, also synchronously completed the initial analysis, assessment and certification of data. A typical experiment results as shown in Fig.32, including voltage and current waveforms, voltage harmonic data, current harmonic data, and voltage etc. Now, further testing is under way, we believe the performance of the Power Quality Analyzer will be improved step by step.

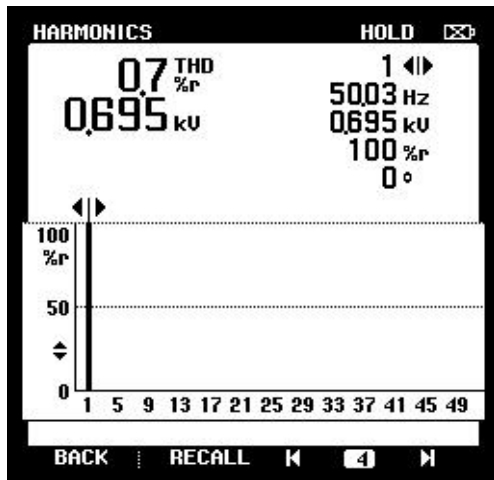


(d) Voltage fluctuation of UBC

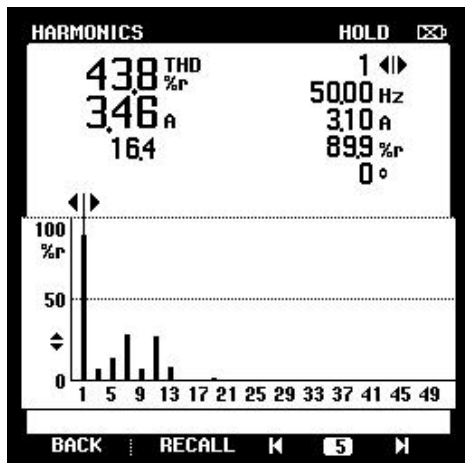
Fig.32 Experiment results of the portable power quality analyzer



(a) The wind turbine voltage and current of phase A



(b) The wind turbine voltage harmonics of phase A



(c) The wind turbine current harmonics of phase A

3. Energy Management System based on Multi-Agent Technology

A novel energy management system is developed based on hybrid multi-agent (MAS) technology. The multi-agent technology is the evolution of the classical distributed technology with specific characteristics, which provided new abilities in controlling complex system. According to the characteristics of renewable energy power system, an intelligent hybrid control system is proposed to embed in the intelligent agent. “Hybrid” stands for that the system plays continuous control algorithm in a certain mode, and plays discrete control strategy in mode transitions when external environment changed. Agents with layered architectures are designed to present RE source utility as shown in Fig.33 [21]. There are five layers, including monitoring layer, union mission planning layer, negotiating and cooperating layer, motion control layer, continue controlling layer, as well as executing and performance evaluating module.

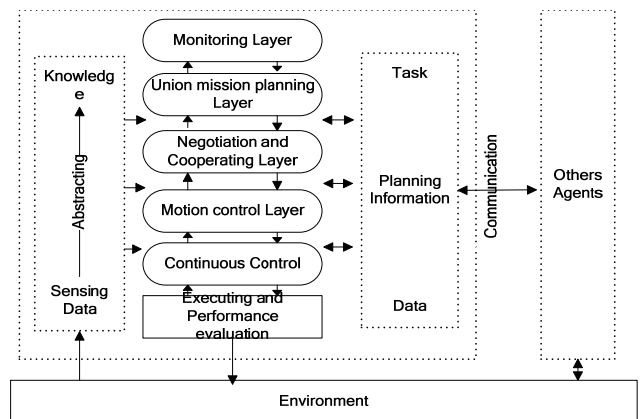


Fig.33 The framework of Agent

The agent can be defined as follows [22]

$$\text{Agent} = \{ \text{ID}, \text{G}, \text{S}, \text{IP}, \text{CC}, \text{I}, \text{E}, \text{ST}, \text{A}, \text{R}, \text{K} \} \quad (29)$$

Where, these elements are defined as follows: Agent-ID, Goal, Sensor, Information Processing, Communicating and Cooperating, Integrated Processing, Effect, State, Ability, Rule database, Domain Knowledge. Especially, states define a discrete operation mode {S1, S2, S3, S4} to present the characterization of the node at macrostructure. S4 stands for operation. S3 stands for the hot stand-by. S2 stands for the cold stand-by. S1 stands for the maintenance outage. Fig.34 shows the relationship of the different mode.

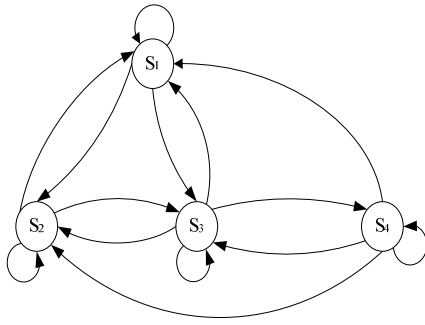


Fig.34 The transition of different mode

According to the demands and requirements of RE power system, the station of optimization and decision-making is shown as follows [23]

$$\min \frac{\sum_i C_{W_i} P_{W_i}(t) + \sum_j C_{PV_j} P_{PV_j}(t)}{\sum_i P_{W_i}(t) + \sum_j P_{PV_j}(t)} \quad (t = 1, 2, \dots, T) \quad (30)$$

$$\text{s.t. } \sum_i P_{W_i}(t) + \sum_j P_{PV_j}(t) - P_L(t) \pm P_{BAT}(t) = 0,$$

$$Q_f = \sum_{i=1}^8 W_i E q_i \geq C, \quad P_{BAT-MIN} \leq P_{BAT} \leq P_{BAT-MAX}$$

Where, C_{W_i} , C_{PV_j} , P_{W_i} , P_{PV_j} are the per-cost and output power of wind turbines and PV arrays respectively, Q_f is the synthetic power quality index.

Based on the objectives mentioned above, the continuous control is implemented by reinforcement learning algorithm. And two cooperation methods are proposed. One is master-slave model based on improved contract-net protocol, the other is totally distributed model based on Petri net and cooperative task planning algorithm.

Energy management in RE power system is distributed and complex. The MAS not only provide perfect framework closing to the real system, but also integrate other AI techniques. The energy management system based on MAS meet the requirement about distribution, heterogeneity, openness, hybrid, cooperation and autonomous.

Nowadays, Micro-grid is a new concept in RE research filed. It is a generation system composed of low-voltage distribution networks, small modular generation devices and loads connected to them. It can also be regarded as a small scale grid based on distributed generation devices, to manage the supply and demand of local energy. Currently, it has become one of the hottest research issues in renewable energy field. The energy management system based on Multi-Agent will become one of main development directions of micro-grid.

V. CONCLUSION

The Environment protection is the most important problems in the countries' sustainable development.

Energy should be more "environment friendly" and achieve "zero emission" by applying RE as power sources. Researches on energy management play a significant role in the process. This article mainly introduces the research efforts on control technologies in distributed generation system based on renewable energy by the New Energy Research Center of South China University of Technology, which includes wind energy generation, photovoltaic generation, and energy management system. For the intact purpose, some achievements by other researchers are referred.

ACKNOWLEDGMENT

The work described in this article was fully supported by the National Natural Science Foundation of China under Grant. 60534040.

REFERENCES

- [1] J. Wu, S.Z. Chen, and J.H. Yang, "Control on green energy source and ecologic environment", Asian Power Electronic Journal, Vol. 1, No. 1, 2007, pp. 36-41.
- [2] J.H. Yang, "Research on Wind Energy Conversion System and Control with Brushless Doubly-Fed Generator", Ph.D. thesis, South China University of Technology, China, 2006.
- [3] J. Wu, S.Z. Chen, and D. Liu, "Control and Power Electronics Technology in Renewable Energy", SCIENCE IN CHINA SERIES E-TECHNOLOGICAL SCIENCES, Vol. 51, No. 6, 2008, pp. 702-712.
- [4] R.Q. Li, "Dynamic modeling, simulation and stability analysis of brushless doubly fed machines", Ph.D. thesis, Oregon State University, American, 1991.
- [5] X.Y. Zhang, J. Wu, and J.H. Yang, "Decoupled power control with sliding mode for brushless doubly-fed machine", Acta Energiæ Solaris Sinica, Vol. 28, No. 1, 2007, pp. 68-73.
- [6] X.Y. Zhang, "Modeling and control of wind energy conversion system with brushless doubly-fed machine", Ph.D. thesis, South China University of Technology, China, 2007.
- [7] J.Q. Han, "From PID technique to active disturbance rejection control technique", Control Engineering, Vol. 3, No. 3, 2002, pp. 13-18.
- [8] J. Wu, Z.H. Shi, J.H. Yang, and Y.R. Chen, "Simulation of Matrix Converter Based on Direct Torque Control", Journal of South China University of Technology (Natural Science Edition), Vol. 34, No. 4, 2006, pp. 47-55.
- [9] S.Z. Chen, J. Wu, G.X. Yao, and J.M. Yang, "Power Limitation Control of Wind Turbine System Based on Differential Geometry Theory" Control Theory & Applications, Vol. 25, No. 2, 2008, pp. 336-340.
- [10] X.Y. Zhang, J. Wu, J.M. Yang, and J. Shu, "H-infinity robust control of constant power output for the wind energy conversion system above rated wind", Control Theory & Applications, Vol. 25, No. 2, 2008, pp..
- [11] J.B. Hu, D. Sun, and Y.K. He, "Modeling and control of DFIG wind energy generation system under grid voltage dip", Automation of Electric Power Systems, Vol. 30, No. 8, 2005, pp. 21-26.
- [12] S.Z. Chen, J. Wu, and M. Liu, "Low voltage ride through control of DFIG wind energy generation system", Acta Energiæ Solaris Sinica, (Accepted for publication).
- [13] K.C. Wong, S.L. Ho, and K.W.E. Cheng, "Direct voltage control for grid synchronization of doubly-fed induction

- generators”, *Electric Power Components and Systems*, Vol. 36, No. 9, 2008, pp. 960-976.
- [14] M. Zhang, “Research of wind and solar PV hybrid generating control system”, Ph.D. thesis, South China University of Technology, China, 2004.
- [15] M. Zhang, and J. Wu, “Application of Slide Technology in PV MPPT System”, *Transactions of China electro technical society*, Vol. 20, No. 3, 2005, pp. 90-93.
- [16] C.A. Cen, M. Zhang, and L.Q. Wang, “Control of the configuration optimization for photovoltaic array”, *Control Theory & Applications*, Vol. 25, No. 2, 2008, pp. 364-366.
- [17] M. Zhang, and J. Wu, “Control system of renewable energy connected grid based on the auto-disturbances rejection control technology”, *Control Theory & Applications*, Vol. 22, No. 4, 2005, pp.583-587.
- [18] Liu, “Research on Distributed Wind-Photovoltaic Hybrid Power Management System”, Ph.D. thesis, South China University of Technology, China, 2008.
- [19] Y.W. Ma, Y.R. Chen, and J. Zeng, “Analysis and evaluation on the electric power quality of wind farm”, *Control Theory & Applications*, Vol. 25, No. 2, 2008, pp 307-310.
- [20] Y. Zhang, J. Zeng, S.W. Wang, and X.M. Yu, “A Portable Power Quality Monitoring System for Wind Power Generation System”, *Control Theory & Application*, Vol. 25, No. 1, 2008, pp. 163-166.
- [21] Liu, J. Wu Jie, J. Zeng, H.X. Guo, and X.M. Yu, “Planning of Distributed Generating Management Based on Multi-Agent System”, *Control Theory & Application*, Vol. 25, No. 1, 2008, pp. 151-154.
- [22] J. Zeng, J. Wu, J.F. Liu, and L.M. Gao, “An Agent-based Approach to Renewable Energy Management in Eco-building”, *IEEE International Conference on Sustainable Energy Technologies*, 2008, Nov, pp. 46-50.
- [23] X.M. Yu, J. Zeng, H.X. Guo, and D. Liu, “Distributed Wind-PV System based on Multi-Agent and Petri Nets”, *Control Theory & Applications*, Vol. 25, No. 2, 2008, pp. 353-356.

A

Agarwal Pramod	21
Aware Mohan V.	15

C

Chen Sizhe	39
------------	----

G

Gulam Amer	30
Gupta R. A.	8
Gao Lamei	39

I

Iqbal Atif	1
------------	---

K

Khan M. Rizwan	1
Kumar Rajesh	8

M

Mohod Sharad W.	15
-----------------	----

P

Pandey A.K.	21
Praveen Kumar A	30

S

Srinivasa Rao.S	30
Surjuse Rajesh S.	8

V

Verma V.K.	21
Virulkar Vasudeo B.	15

W

Wu Jie	39
--------	----

Z

Zeng Jun	39
----------	----

Submission details

Only online submission will be accepted. Please first register and submit online. The paper is in double column and is similar to most IET or IEEE journal format. This is no page limit. Any number of pages of more than 6 will be subject to additional charge.

The paper guidelines can be downloaded using the link: <http://perc.polyu.edu.hk/apejournal/>

Any queries, please contact Prof. Eric Cheng, Publishing Director of APEJ, Dept. of Electrical Engineering, The Hong Kong Polytechnic University, Hung Hom, Hong Kong.

Email: eeecheng@polyu.edu.hk Fax: +852-2330 1544

Any secretarial support and production related matters, please contact Mr. Ken Ho, Power Electronics Research Centre, The Hong Kong Polytechnic University, Hung Hom, Hong Kong.

Email: eeapej@polyu.edu.hk Tel: +852-3400 3348 Fax: +852-3400 3343

Publication Details

The Journal will be published 3 times a year. The first issue was published in 2007. Response time for paper acceptance is within 3 months.

Financial Charge

All the accepted papers will be printed without charge for 6 or less pages. An additional page charge is HK\$100 per page. A hardcopy of the journal will be posted to the corresponding author free of charge. Additional copies of the journal can be purchased at HK\$200 each. The charge includes postage and packing.

All Chinese Papers will be subjected to a translational fee of HK\$350 per page. It will be charged when the paper is accepted for publication.

Advertising

Advertisement is welcome. Full page advertisement is HK\$1000. For colour advertisement, the amount is doubled. All the advertisement will be both posted online in the journal website and hardcopy of the journal.

For advertising enquiries and details, please contact Ms. Anna Chang, eeapej@polyu.edu.hk .

Tel: +852-3400 3348 Fax: +852-3400 3343

For payment, please send your cheque, payable to 'The Hong Kong Polytechnic University, address to Ms. Canary Tong, Secretary of APEJ, Dept. of Electrical Engineering, The Hong Kong Polytechnic University, Hung Hom, Hong Kong.